METASURFACE BASED UNCOOLED $SI_xGE_yO_{1-x-y}$ MICROBOLOMETER FOR INFRARED DETECTION

A Dissertation

Presented to

The Faculty of the Graduate School

At the University of Missouri-Columbia

In Partial Fulfillment

of the Requirements for the Degree

Doctor of Philosophy

---

by

AMJED ABDULLAH

Dr. Mahmoud Almasri, Dissertation Supervisor

May 2022

The undersigned, appointed by the dean of the Graduate School,
have examined the dissertation entitled

METASURFACE BASED UNCOOLED $SI_xGE_yO_{1-x-y}$ MICROBOLOMETER FOR INFRARED DETECTION

Presented by Amjed Abdullah

A candidate for the degree of

Doctor of Philosophy

And hereby certify that, in their opinion, it is worthy of acceptance.

_____

Associate Professor Mahmoud Almasri

_____

Professor Naz E. Islam

_____

Professor Gohn Gahl

_____

Associate Professor Yan Zheng

_____

Associate Professor Edward Kinzel

ACKNOWLEDGEMENTS

It is a pleasure to express my thanks and gratitude to my Advisor, Dr. Mahmoud Almasri, for giving me the opportunity to work in the Microsystem Research Laboratory. I would like to thank him for his invaluable encouragement, guidance, support, and help throughout my master's and PhD research. I am also thankful to all my committee members, Dr. Islam, Dr. Gahl, Dr. Yan, Dr. Kinzel, and Dr. Almasri for the time and contribution with their valuable input toward the completion of this work.

I extend my thanks to my friend and brother Ibrahem Jasim for being by my side throughout my Ph.D journey. I will always be appreciative for his help and support. Also, my other colleagues in the lab: Akshay Koppula Reddy, Omar Alkorjia, Jiayu Liu, Sura Abd-Alzahra, Weinan Zhang, and Mohammed Almalaysha for their help and support.

I specially want to thank my parents and my siblings for their encouragement, love, and support throughout my life. This project was supported by National Science Foundation, Grant Nos. 1509589 and 1653792.

TABLE OF CONTENTS

LIST OF FIGURES

LIST OF TABLES

NOMENCLATURE

α_H	Hooge's Constant
V_J	Johnson Noise
η	Absorptivity
μ	Carrier Mobility
τ_{th}	Thermal Time Response
D^*	Detectivity
E_a	Activation Energy (eV)
G_{th}	Thermal Conductance
C	Thermal Mass
K_f	Hooge's Coefficient
R_v	Voltage Responsivity
TCR	Temperature Coefficient of Resistance
Au	Gold
Cr	Chromium
EDX	Energy-dispersive X-ray spectroscopy
FPA	Focal Plane Array
FTIR	Fourier Transform Infrared Spectroscopy
IR	Infrared
NETD	Noise Equivalent Temperature Difference
NiCr	Nickel-Chrome
RF	Radio Frequency
RTS	Random Telegraph Switching

Si-Ge-O	Silicon Germanium Oxide
Si_3N_4	Silicon Nitride
SiO_2	Silicon Dioxide
Ti	Titanium
Al	Aluminum
VOx	Vanadium Oxide
XRD	X-Ray Diffraction
YBaCuO	Yttrium Barium Copper Oxide
LWIR	Long Wavelength Infrared

ABSTRACT

In this research, we have investigated metasurface integrated uncooled $Si_xGe_yO_{1-x-y}$ microbolometers. Two device architecture were fabricated and characterized.

The first design presents the implementation of metasurface integrated uncooled infrared (IR) silicon germanium oxide (Si-Ge-O) microbolometers for Long Wavelength Infrared (LWIR) detection. Metasurface materials were proposed in this design to increase the absorption of the microbolometer and to provide wavelength selectively based on the geometry of the metasurface material. The inclusion of the metasurface permits engineering the IR absorptance with respect to wavelength. Absorption by the metasurface eliminates the need for a ¼-wave resonant cavity under the microbolometer. In addition, the metasurface can significantly improve the electrical performance of the temperature-sensing layer. Experimental results show an increase in the Temperature Coefficient of Resistance (TCR) and a decrease in the resistivity of the amorphous Si-Ge-O films. These parameters scale with the periodicity and area fraction of the metasurface. The voltage noise power spectral density was reduced by annealing the devices in vacuum and in forming gases. The results demonstrated that annealing in vacuum lowered the noise much more than that of annealing in forming gases. The lowest measured noise in vacuum annealing for the metasurface integrated microbolometer was 1.2×10^{-16} V^2/Hz at the corner frequency, where Johnson noise meet 1/*f*-noise. This frequency was lowered to 10 Hz (from 87 Hz) after 4 hours annealing. In addition, the corresponding Hooge's parameters γ, β and K_f for the device were 1.02, 2.01, 2.637×10^{-14}, respectively. The measured responsivity and detectivity approached 10^4 V/W and 10^8 cm $Hz^{1/2}$/W to filtered blackbody infrared

radiation. The microbolometer PSD noise was studied in detail and reduced using vacuum annealing and forming gases annealing and the results showed significant reduction of the noise level and the corner frequency compared to the noise without annealing. In addition, the spectral responsivity and detectivity were measured in vacuum as a function of IR wavelength over the range from 4 μm to 14 μm.

In the second microbolometer architecture, A new uncooled microbolometer is presented that utilizes an amorphous silicon germanium oxide ($Si_xGe_yO_{1-x-y}$) infrared (IR) sensitive material, a dual level architecture with dual-air cavity fabricated on top of each other, and a metasurface to control IR absorption/reflection in interaction with standard Fabry-Pérot cavity. The design combines two-microbolometer stack in a single pixel to achieve high IR absorption over two distinct spectral windows across the long wavelength infrared region (LWIR) without using a filter wheel. The bottom microbolometer uses a metasurface to selectively absorbs a portion of the spectrum, and reflects radiation outside this window range, while the top microbolometer uses a conventional Fabry-Pérot resonant cavity to absorb a different portion of the spectrum and transmit any unabsorbed radiation outside this window. This device can be used to measure the absolute temperature of an object by comparing the relative signals in the two spectral bands. The spectral responsivity and detectivity, and thermal response time were > 10^5 V/W, > 10^8 cm $Hz^{1/2}$/W, and 1.13 ms to filtered blackbody infrared radiation between 2–16 μm. The microbolometer voltage noise power spectral density was reduced by annealing the microbolometers in vacuum at 300 ^oC.

CHAPTER 1: INTRODUCTION

This chapter presents an overview of the applications of the uncooled infrared thermal cameras, infrared thermal detectors, infrared material, and metasurface materials and detectors.

1.1 Applications of Uncooled Infrared Thermal Cameras

IR thermal cameras detect variations in heat and create an electronic image/video of everything in view. Cameras that are based on uncooled microbolometers have broad range of military and civilian applications such as automotive and truck safety, medical diagnostics, surgical interventions, surveillance, law enforcement, and security. Most of the cameras that use thermal sensors are developed by multiple companies such as Raytheon [1], L-3 Communications [2], Leonardo DRS [3], British Aerospace BAE Systems [4], Institute National d'Optique INO [5], Semiconductor Devices Ltd SCD [6]. For example, night vision cameras as shown in Figure 1.1 increase a driver's perception and seeing distance in detect objects long before the car headlights

Figure 1.1: Thermal imaging makes night driving clearer and help avoiding accidents.

would illuminate them. In firefighting, it is used to enable the fire fighter to see through smoke as shown in figure 1.2. The same infrared technology is utilized to image blood flow, and map body temperature. In military, the infrared detectors are used, e.g., inside

Figure 1.2: Temperature detection in smoky environment using infrared detectors.

the small drones that can travel distances and record instant videos of the surrounding thread as shown in Figure 1.3. In industrial processing, it is used to monitor hot spots, micro-cracks and observe machines and processes for proper temperature a shown in

Figure 1.3: Thermal detectors were used with small drones to record instant videos.

Figure 1.4. Also, the IR radiation cameras are widely used for surveillance purposes, it has the ability to capture videos in low light and no light areas as shown in Figure 1.5.

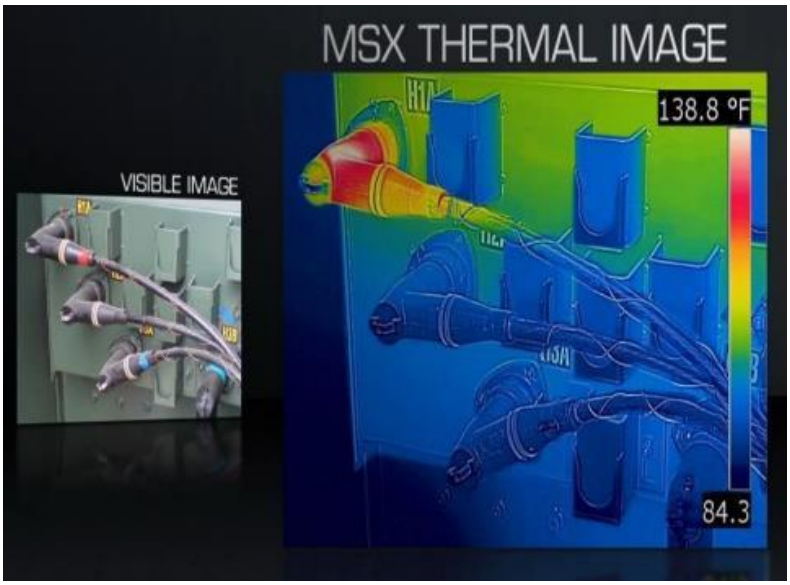

Figure 1.4: Thermal imaging can be used in the industry to identify such as hot spots.

Figure 1.5: IR imaging is used for civilian surveillance and security applications.

Multiband infrared cameras can resolve attributes of the scene beyond the intensity of the incident radiation, i.e., wavelength selectivity. Such camera permits the determination of the temperature of objects to be resolved as well as multicolor without a-priori knowledge of the objects emittance. The multispectral improvements provide

enhanced abilities to defeat camouflage and wavelength selectivity which has potential applications in detecting reflected versus emitted radiation sources as well as identifying manmade sources such as lasers. With the utilization of the multispectral images, it would reveal more information of the scene and enhance the ability of detecting and identifying the targets as shown in Figure 1.6 and Figure 1.7. In addition, multispectral dependent pixels provide a combinations of narrowband wavelength s electivity which opens up a broad application space for multispectral gas detection and

Figure 1.6: More Information are revealed with multispectral images using multispectral detectors.

Figure 1.7: Multispectral thermal detectors are used to defeat camouflage.

better thermal measurement to quickly identify leaks and leaky equipment that may need repair, increasing efficiency and reducing economic losses. Early detection also reduces any potential detrimental effect of gas emissions to the atmosphere as shown in Figure 1.8.

Figure 1.8: Gas leak detection using multispectral thermal imaging.

1.2 Review of Uncooled Infrared Materials

1.2.1 Vanadium Oxide (VOx)

Vanadium Oxide (VO_x) technology is one of the two main mainstream infrared materials used in the production of commercial thermal cameras. The material is deposited from low temperature ion beam sputtering system of mixed oxides (VO_2, V_2O_5, V_2O_3), and goes through rapid thermal annealing to oxidize and achieve the desired resistance. VOx has an acceptable TCR between −2 %/K to −2.4 %/ and 1/*f*-noise of 2.3×10^{-8} V/Hz$^{1/2}$ at 5 Hz with a bias current of 19.3 µA [7]. Current VOx devices utilize a pixel size of 17×17 µm^2 and routinely reported NETD value of < 50 mk [8], [9].

1.2.2 Amorphous Silicon (*a*-Si)

Amorphous silicon, *a*-Si, is the second mainstream infrared material used in the production of IR thermal cameras. It has been widely used as an infrared sensitive

material in uncooled microbolometers [10]–[12]. *a*-Si has achieved wide range of TCR with high values between −2.5 %/ K and −5 %/ K with a corresponding resistivity range from 200 Ω-cm to 1×10^5 Ω-cm [13]. This TCR value was used to build fully operational 17×17 μm^2 long wave infrared focal plane array (FPA) [14]. In addition, the fabricated *a*-Si microbolometers with a size of 17×17 μm^2 by L-3 Communications have achieved NETD less than 35 mK for spectral window between 8-12 μm [2].

It is noted that *a*-Si microbolometers took advantages of the extensive knowledge available in Si manufacturing processes as it can be deposited using traditional Plasma Enhanced Chemical Vapor Deposition (PECVD) on high volume deposition tools. Two RF modes (13.56 MHz and 380 kHz) have obvious influence on the deposition rate of amorphous silicon, high RF mode result in higher deposition rate, but not certain on the residue stress. The power used is proportional to the deposition rate and to the stress induced at high RF mode. Low power is used for low stress film. At high RF mode, the deposition rate decreases with temperature while stress increases. Increasing the flow rate of argon will decrease the stress in both RF modes, while the deposition rate decreases for the low RF mode. The overall production cost of *a*-Si based cameras is low, which has enabled high volume commercial market [15], [16].

1.2.3 Polycrystalline Silicon (Poly-Si)

The single crystal silicon, Poly-Silicon consists of multiple individual grains. These grain boundaries scatter phonons, which yield to decrease the thermal conductivity of the grain. The thermal properties of Poly-silicon cannot be inferred from single crystal silicon data due to the variability of grain sizes. This material is subjected to a series of high temperature annealing cycles around 925 °C to achieve wide range of resistivity.

It is doped with phosphorous, arsenic, or boron. It has a mechanically stable structure and a TCR of 1-2 %/ K [17].

1.2.4 Polycrystalline Silicon Germanium Alloy (Poly-Si-Ge)

Polycrystalline silicon-germanium (poly-Si-Ge) has recently been shown to be a favorable alternative to polycrystalline silicon (poly-Si) for various applications in metal oxide semiconductor (MOS) technologies. Ploy-Se-Ge can be fabricated using conventional microelectronic fabrication techniques below 550 °C, whereas Poly-Si require processing temperatures above 600 °C. Poly-Si-Ge thin films were deposited using silane (SiH_4) and germane (GeH_4) as source gases with a base pressure of 2.5×10^{-2} Pa and at temperature of 550 ˚C by CVD. Then, the poly-Si-Ge films were doped through ion implantation with two different boron doses: 4×10^{13} and 5×10^{15} cm^{-2}. The poly-Si-Ge were annealed at different temperatures ranging from 650 to 1050 ˚C for 1 min in N_2 atmosphere by rapid thermal annealing (RTA). After performing RTA, the films becomes polycrystalline [18]–[21].

1.2.5 Yttrium Barium Copper Oxide (YBaCuO)

YBaCuO has been used as an IR detector material in both superconducting (oxygen-rich) and semiconducting (oxygen-depleted) phases. $YBa_2Cu_3O_{6+x}$ in its crystalline, phase with $x > 0.95$ is a High-Temperature Superconducting (HTS) materia1with the superconducting transition T_c= 90K. It is most studied and characterized material among CuO based HTS materials. The electrical and optical properties of $YBa_2Cu_3O_{6+x}$ vary with the oxygen stoichiometry. At ($0< x < 0.3$), the YBaCuO compound is a Mott-Hubbard insulator with a well-defined charge transfer gap of the order of about 1 .5 eV between the O (2p) band and Cu (3d) band. As x is increased $x < 0.5$, random oxygen

doping introduces disorder to O1 sites of the intercalated layers, resulting in localized states that serve as charge reservoirs for the transfer of carriers to the conduction planes. Thus, YBaCuO showing the electronic characteristics of a Fermi glass. As x is increased above 0.5, YBaCuO undergoes a semiconductor-metal transition to metallic state with an orthorhombic structure that exhibits superconductivity upon cooling [22]–[25].

As an alternative, many other IR materials have been investigated and used in uncooled microbolometers, which includes Si/SiGe quantum well microbolometer [26], Molybdenum Oxide (MoO_x), Nickel Oxide (NiO_x) [27], metals [28], [29], and Silicon Germanium Oxide (Si-Ge-O).

1.2.6 Silicon Germanium Oxide (Si-Ge-O)

We have selected to study amorphous $Si_xGe_yO_{1-x-y}$ IR sensing layer as a new addition to the mainstream materials due to its excellent IR radiation, absorption, and mechanical and electrical properties at room temperature. The sensing layer can achieve low resistivity with a high TCR and low 1/*f*-noise. Keeping the 1/*f*-noise level low improves the performance of the device (responsivity and detectivity). Also, Si and Ge based compounds are standard materials in silicon integrated circuits providing a wide range of fabrication knowledge of the microbolometer array. In addition, $Si_xGe_yO_{1-x-y}$ sensing layer is compatible with CMOS technology due to the low deposition temperature and the use of conventional dry-etch processing. The $Si_xGe_yO_{1-x-y}$ based detectors can be easily integrated with the readout electronics [30]–[33].

Many research groups have investigated Si-Ge-O as an IR sensitive material. Clement *et al* [33] deposited $Ge_{0.85}Si_{0.15}$ in an oxygen/ argon environment. The resulting resistivity and TCR of the sputtered film were 10 KΩ and -5 %/K, respectively. They

have showed the possibility to achieve a sensing material with a high value of the activation energy by increasing the oxygen content in the films. In addition, the resistivity of the films can maintain moderate values by applying a bias voltage to the substrate during deposition. Ahmed *et al* [34] studied the formation of a-$Ge_xSi_{1-x}O_y$ in detail with the objective of optimizing film properties for use in uncooled bolometer applications, requiring high TCR and acceptable resistivity. Implemented Co-sputtering of Ge and Si in oxygen and argon which allow the content of each element to be controlled separately. They proved that for a fixed oxygen concentration, the TCR and resistivity increase as Si concentration increases up to 5-10 atomic % and then start to decrease. Those parameters are proportional to the oxygen concentration in $Si_xGe_yO_{1-x-y}$ films. They noted that the high oxygen concentration in the film (14% and above) might have resulted in high resistivity and TCR. Values of temperature coefficient of resistance as high as -5 %/K were obtained at moderate resistivity values around 3.8×10^4 Ωcm by controlling both silicon and oxygen contents. Similar sputtering method was investigated by Rana *et al* [35]. The silicon and oxygen concentrations were varied in an investigation of dependence of the electrical and optical characteristics of the thin films on the composition parameters. They have found as the Si concentration was increased in the $Si_{1-x}Ge_x$ films; the temperature coefficient of resistance (TCR) was decreased. Also, for $Si_{1-x}Ge_xO_y$ films the addition of oxygen to the $Si_{1-x}Ge_x$, increased the activation energy and TCR. The TCR was measured to vary from − 2.27 %/K to − 8.69 %/K. We have employed $Si_xGe_yO_{1-x-y}$ as the sensitive material in this thesis. The activation energy (EA), resistivity, and TCR of $Si_xGe_yO_{1-x-y}$ mainly depend on the amount of oxygen content in the film, which controlled through the deposition process. A high TCR and low resistivity values can be achieved at some

specific silicon and oxygen percentage. A high TCR above -3 %/k and low resistivity compositions were used on the fabricated microbolometer using the RF magnetron sputtering machine which provides a uniform coating on the substrate. Table 1 shows the common uncooled infrared materials.

Table 1: TCR of common uncooled infrared materials.

IR sensitive material	TCR (%/k)	References
VOx	-(2 - 2.4)	[36], [37]
α: Si	-(2 - 3.9)	[38]–[40]
YBaCuO	-(2.88 - 3.5)	[23], [24]
Si-Ge	-(2 - 3)	[19], [41]
Metal	-0.2	[42]
Ge	-1	[43]

1.3 Uncooled Infrared Detectors

1.3.1 General Infrared Detectors

Infrared detector exhibits a change of some measurable electrical property that accompanies a change in the temperature of the sensitive element due to the absorption of IR radiation. The Infrared detector has the ability to absorb the infrared radiation without the need of any cryo-cooling apparatus for operation. The basic structure consists of a sensitive pixel connected to a heat sink via the support/electrode arms. Every object, whose temperature is more than absolute zero, radiates IR radiation. A black body is an ideal hypothetical object considered to be a perfect absorber and a perfect radiator. It absorbs all incident electromagnetic radiation, regardless of frequency or angle of incidence. At thermal equilibrium, it emits electromagnetic radiation called black-body radiation. The radiation is emitted according to Planck's law, expressed as (1):

$$M_{e,\lambda}(\lambda, T) = \frac{2\pi hc^2}{\lambda^5[e^{\frac{hc}{\lambda k_B T}} - 1]} \quad (1)$$

where, M is known as spectral radiance in W/(cm^2-μm), T is its absolute temperature, c is the speed of light in the medium, λ is its wavelength, kB is the Boltzmann constant and h is the Planck constant.

Infrared (IR) radiation ranges from the red edge of visible spectrum at 0.78 μm to 1 mm that corresponds to a frequency range of approximately 400 THz to 300 GHz. Objects usually emit infrared radiation across the whole IR spectrum. The region of interest in the infrared radiation range has been recognized, the infrared band is generally subdivided into different sub-bands, specifically classified into five sub regions. These are: near IR (NIR) that ranges from 0.7 μm to 1.4 μm, short wavelength IR (SWIR) that ranges from 1.4 μm to 3 μm, mid wavelength IR (MWIR) which ranges from 3 μm to 8 μm, long wavelength IR (LWIR) that ranges from 8 μm to 15 μm and far wavelength IR (FWIR) which extends from 15 μm to 1 mm [44]. The Infrared imaging detectors have a broad spectrum of commercial and military applications including surveillance, threat detection, target recognition, medical diagnostics, firefighting, and security [45]–[47]. Therefore, there have been an interest for researchers to study and optimize different materials and designs to achieve a perfect infrared absorber. For example, L-3 communication have developed 17×17 μm^2 low thermal pixel size based on *a*-Si sensing material with high fill factor, it employs a ¼ wave resonant cavity to enhance the infrared absorptance. It is integrated with amorphous silicon films with TCR of up to 3.9 %/ K [48]. Figure 1.9 shows the SEM micrograph of the fabricated devices. The pixel design exhibits a quarter-wavelength resonant absorptance centered in the LWIR band exhibiting infrared absorptance ~90%

across the LWIR band. Raytheon Vision Systems (RVS) has made a significant improvement in the development of a 640×512 uncooled arrays with a unit cell size of 17×17 μm^2, and performance that is similar to 25 μm arrays. The key factor

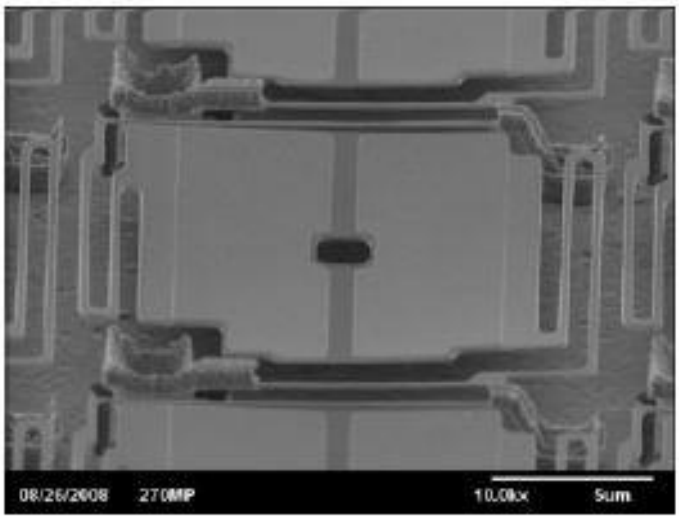

Figure 1.9: Low thermal mass 17μm pixel size with high fill factor designed by L-3 communications.

development of this array is the first step in achieving mega-pixel formats. This FPA is designed to ultimately achieve performance with noise equivalent temperature difference of (NETD) <50 mK at 30 Hz with an 8 msec time constant. VOx was selected as the microbolometer material due to its combination of moderate temperature coefficient of resistance (TCR), low electrical resistivity and low 1/*f*-noise. The detector showed an absorption peak of 80% in the spectral band of 8 to 14 μm and a TCR of 2.4 %/K [37]. Figure 1.10 shows SEM micrographs of the fabricated detectors. DRS developed an umbrella pixel structure. The top "umbrella" layer consists of absorbing dielectric films, which works along with the underlying thermal isolation structure to maximize the radiation absorption. The umbrella covers most of the pixel and it is connected through a post at the center for thermal conduction to the VOx

microbolometer body. VOx sensing thin film is placed at the center of the layer where resistance change occurs upon incoming radiation. The detector showed a good sensitivity and NETD of < 50 mK with a spectral band of 7-14 µm, and 12-16 ms

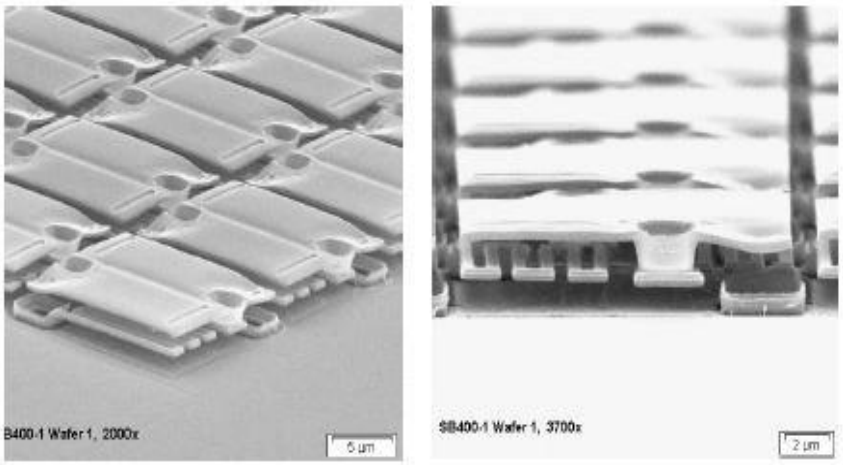

Figure 1.10: SEM micrographs of a 640×512 17µm FPA developed by RVS.

thermal time constant [49]. Figure 1.11 shows the SEM micrograph of the fabricated detector and cross section of the umbrella detector. Infrared Technology Corporation (ITC) developed a high performance 25 µm 640×480 uncooled infrared sensors for high performance applications including military markets. The Uncooled focal Plane array (FPA) responsivity was > 10 V/K with a frame rate of 30 Hz and a noise equivalent

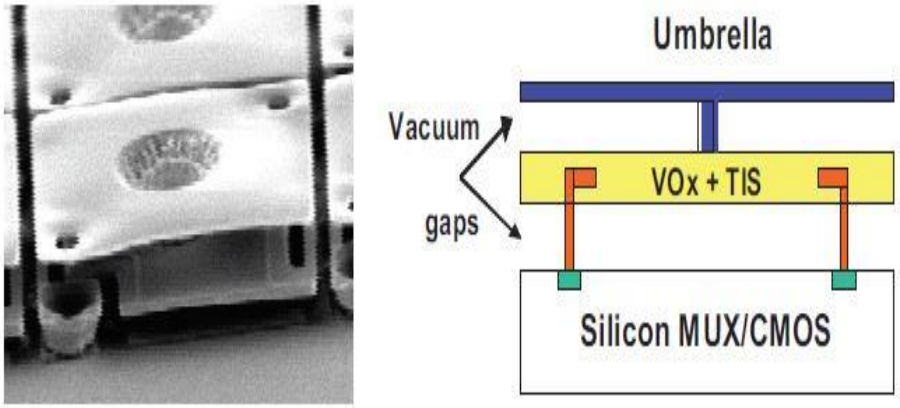

Figure 1.11: SEM micrograph of the fabricated detector and a cross section of the umbrella detector developed by DRS.

temperature difference of < 60 mk [50]. Figure 1.12 shows the SEM micrographs of the fabricated infrared detector.

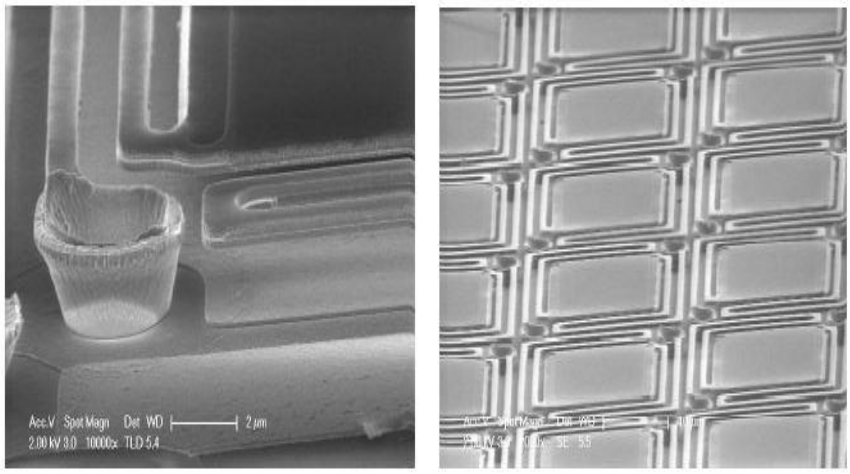

Figure 1.12: Focal plane array with a 25 µm pitch pixel developed by Infrared Technology Corporation (ITC).

Laboratorie Infrarouge (LIR) of the Electronics and Information Technology Laboratory (LETI) has developed a specific microbolometer technology for 25 µm pitch IRFPA achievement shown in Figure 1.13. This structure still relies on a single level microbridge arrangement to ensure noise reduction. presenting a complete characterization of an advanced dedicated 320×240 IRCMOS circuit that takes

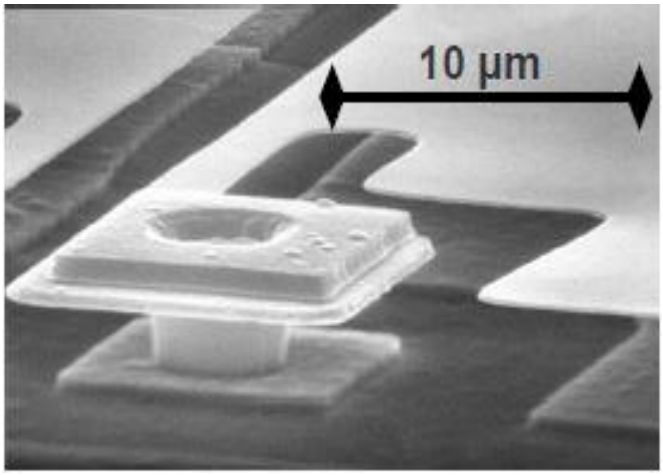

Figure 1.13: FPA of the 25 µm pitch pixel developed by Electronics and Information Technology Laboratory (LETI).

advantage of the new 25 µm pitch microbolometer process. The response and NETD mean values are 8.1 mV/K and 78 mK, respectively. The low drift DC operating point and reduced microbolometer responsivity enabled LETI to investigate the operation with a simplified proximity electronic in the future [51].

1.3.2 Si-Ge-O Based Infrared Detectors

$Si_xG_yO_{1-x-y}$ sensitive materials have been developed and used by many research groups and have a promising result in the infrared detection area. Rana *et al* [52] investigated the material for compositions, electrical and optical performance. The detectors based on this material were fabricated using surface micromachining with a polyimide sacrificial layer shown in Figure 1.14. The thickness of the suspended $Si_{0.15}Ge_{0.85}$ thin film was 200 nm. The TCR values were ranging from -1.13 to -1.25%/K. The thermal conductance of the microbolometers was ~10^{-5} W/K. The I-V characteristics of the detector were measured and showed a linear region between -20 µm to 20 µm without joule heating. The linear I-V characteristics were the result of

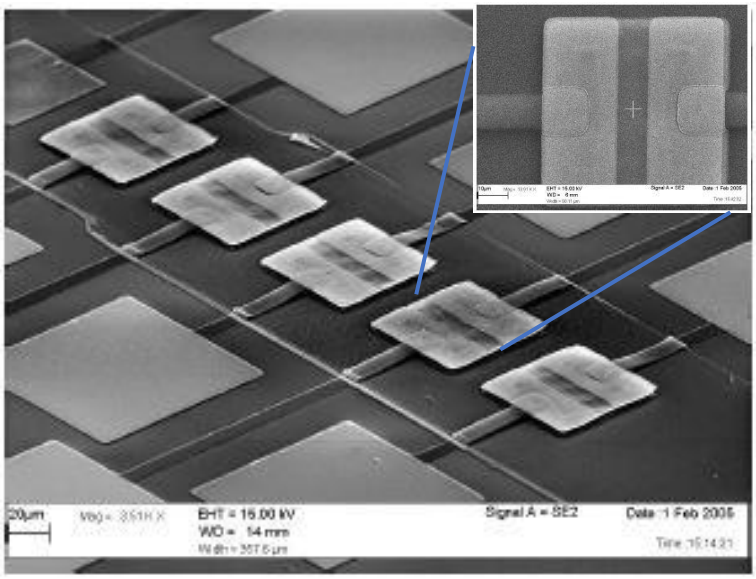

Figure 1.14: SEM micrographs of 60×60 µm^2 detector array with of $Si_xGe_yO_{1-x-y}$ sensing layer.

using highly doped Si in the SiGe sputter target and choosing Au as a contact material. Ahmed *et al* [53] studied and demonstrated the formation of $Si_xGe_yO_{1-x-y}$ as a detector in a combined vertical resistor and absorber structure, shown in Figure 1.15. The presented design and microbolometer fabrication is suitable for integration with CMOS read-out electronics. Measurement of noise characteristics showed 1/*f*-noise and Johnson noise as the dominant sources in the fabricated microbolometers. They stated that 1/*f*-noise is originated from the dangling bonds at the material surface. Non-ohmic contacts can be another source of 1/*f*-noise, which may influence device performance. Another component for excess noise is the random telegraph switching (RTS) noise, which is believed to be a bulk effect noise and is not related to surface or contact

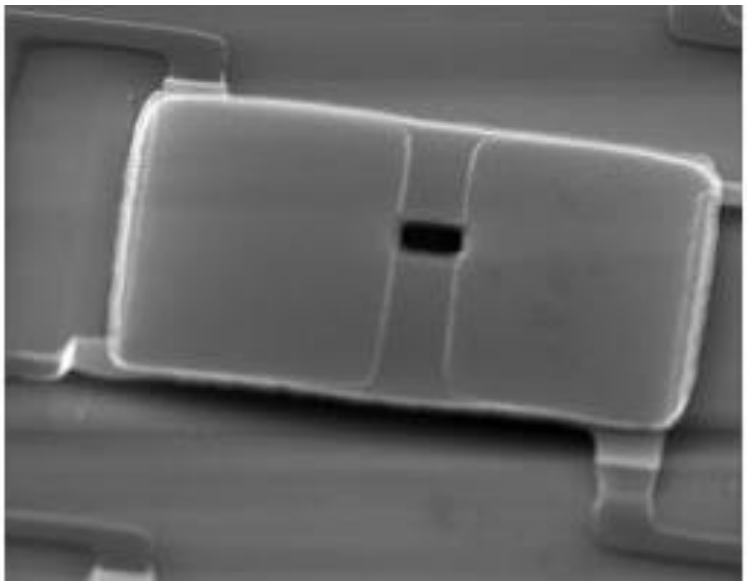

Figure 1.15: Released microbolometer structure SEM micrographs for the sandwiched design.

interface effects. The responsivity values were as high as 1.67×10^5 V/W, and a normalized detectivity as high as 6.7×10^8 cm $Hz^{1/2}$/W at 10 Hz chopping frequency. The thermal response time of the device was 13 ms. The reported thermal conductance of the fabricated devices was 0.36×10^{-7} W/K. Clement *et al* [32] presented the

fabrication of bulk micromachined microbolometers made amorphous germanium silicon oxygen $Ge_xSi_{1-x}O_y$ and developed by reactive sputtering of a $Ge_{0.85}Si_{0.15}$ target with a pixel size of 100×100 μm^2 as shown in Figure 1.16 with the integrated gab structure. The authors reported thermally isolated devices with thermal conductance G_{th} of 3×10^{-6} W/K at atmospheric pressure. The employment of amorphous $Ge_xSi_{1-x}O_y$ sensing layer with high values of the thermal coefficient resistance TCR of -4.2 %/K provided a device structure responsivity of 380 V/W at a bias current of 100 nA. The detectors have response time of 1.8 ms.

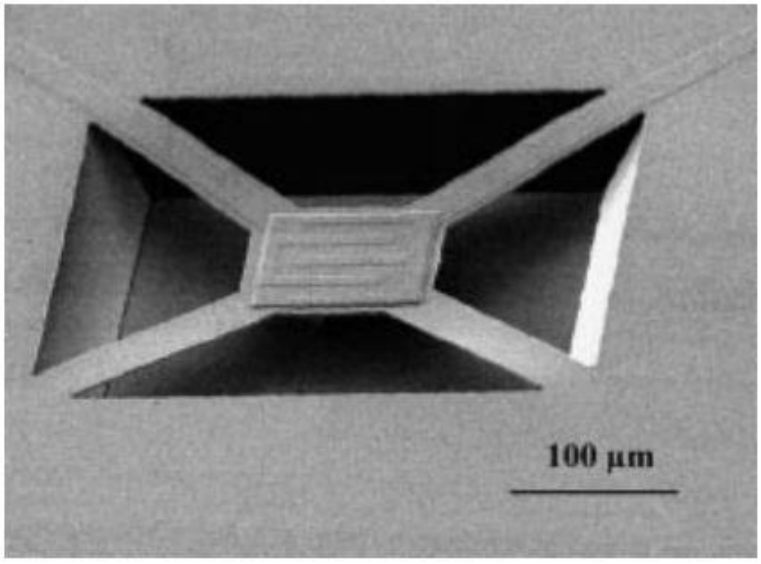

Figure 1.16: SEM picture of the fabricated bolometer showing the interdigitated gap sandwich structure.

1.3.3 Multiband Tunable Detectors

Spectral tuning can be achieved using Fabry-Perot cavity where focal plane array's (FPA's) pixels have to be fabricated with multiple cavity heights. This poses significant manufacturing challenges. Several groups have experimented with dynamically tuning the microbolometer's cavity. Song *et al* [54] employed the electrostatic actuation and reported the design and characterization of adaptive microbolometers with a thermally

tuned responsivity. The maximum actuation voltage was set to 17 V, and the thermal conductance, responsivities and detectivities of a typical device can be switched more than an order of magnitude between 1.65×10^{-5} W/K and 2.99×10^{-4} W/K , between 1.5 V/ W and 0.2 V/ W and between 1.8×10^{6} cm $Hz^{1/2}$ /W and 1.5×10^{5} cm $Hz^{1/2}$/ W , respectively. This extends the dynamic range of the device more than an order of magnitude. The device pixel size is 100×100 μm^2 as shown in Figure 1.17. The high sensitivity state corresponded to normal microbolometer operation. In the low sensitivity state, a portion of the support beam is actuated to be partially in contact with the substrate and that increased the thermal conductivity and reduced the detectivity.

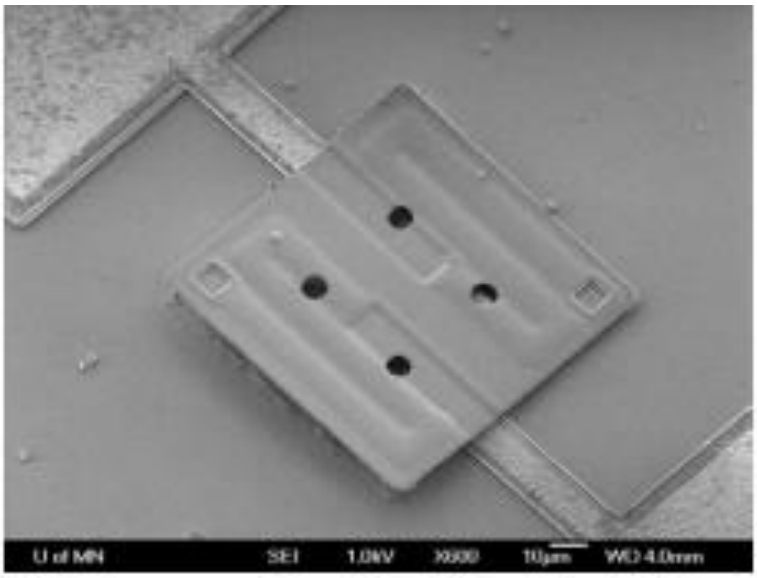

Figure 1.17: SEM micrograph of the tunable responsivity by electrostatic actuation.

They reported that the thermal conductance of a typical device could be changed by 1.25 orders of magnitude, the responsivity by one order of magnitude and the detectivity by 1.2 orders of magnitude with the minimum NEP of 5.6×10^{-8} W $Hz^{-1/2}$ in the high sensitivity state. Gia *et al* [55] employed Liquid Crystals (LCs) method to provide selective reflection and multispectral thermal imaging utilizing the Blue Phases (BP) transitions, which is the transition between the cholesteric and isotropic phases of liquid

crystals. Liquid crystals are organic substances which behave, from a mechanical point of view, as liquids while they simultaneously exhibit optical properties similar to crystalline materials. The authors fabricated and designed a thermal imaging apparatus which combined the attributes of weak first-order phase transitions between BPI and BPII to the colors of BPI and BPII caused by the selective reflections, by investigating the temperature dependent phase transition between BPI and BPII for tuning of selective wavelengths. Figure 1.18 shows the reflection spectra of the BPI and BPII phases and the phase transition. Vladimir *et al* [56] investigated a movable micromirror with the microbolometer structure to achieve multispectral. A micromirror switching between two spatial positions under the detector, provides a response to two wavelength windows by tuning the optical resonant cavity. The resonance between the incoming

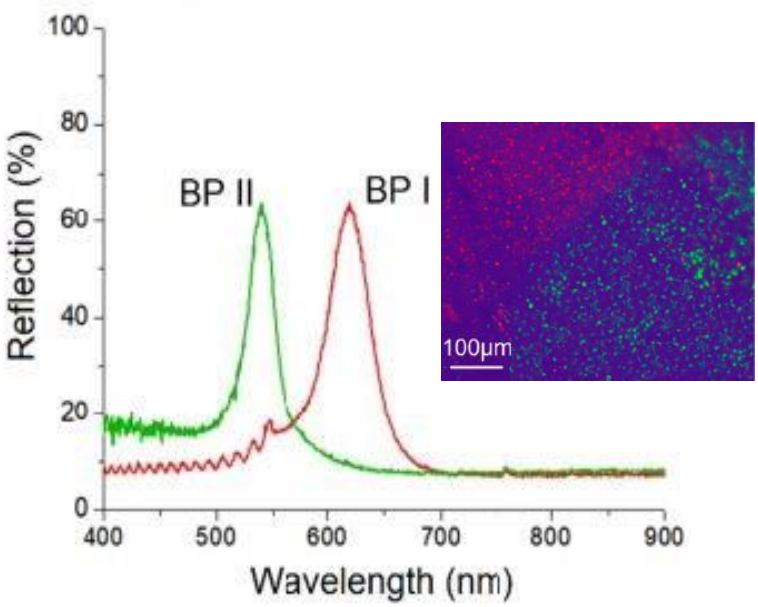

Figure 1.18: Reflection spectra of the BPI and BPII phases and the phase transition.

and reflected waves in the micromachined cavity under the pixel is wavelength dependent, so the detector can be tuned to a particular spectral band when the cavity depth is varied. The image can then be integrated at the readout level to achieve a multicolor IR picture. Figure 1.19 shows the optical tuning of the resonant cavity in the

8-14 μm IR region where the dotted curve shows the conventional tuning for the whole 8–14 μm window. The solid curves show the proposed tuning, providing a selection of the 8–10.5 or 10.5–14 μm regions. Almasri *et al* [57] presented a modeling and design

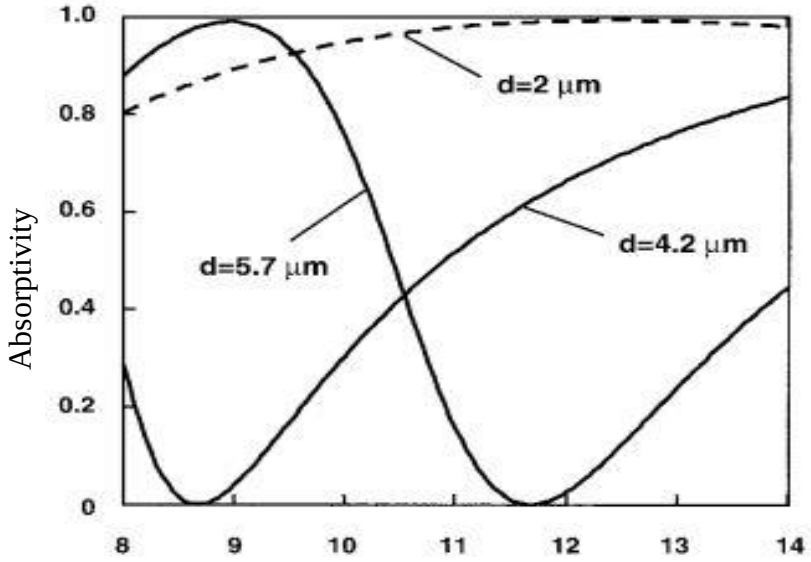

Figure 1.19: Optical tuning of the resonant cavity in the 8–14 μm IR region.

of two color microbolometers for uncooled infrared (IR) detection. Developing a high resolution IR detector array that can measure the actual temperature and color of an object based on two spectral wavelength regions using a tunable micromachined Al mirror. The mirror is switched between two positions by the application of an electrostatic voltage. The switching of the mirror between the two positions enables the creation of two wavelength response windows, 3–5 μm and 8–12 μm. Also, enable the determination of the actual temperature of the scene obtained by the IR camera by comparing the two response wavelength windows. The microbolometer is designed with a low thermal mass of 1.65×10^{-9} J/K and a low thermal conductance of 2.94×10^{-7} W/K to maximize the responsivity Rv to a value as high as 5.91×10^{4} W/K and detectivity D to a value as high as 2.34×10^{9} cm $Hz^{1/2}$/W at 30 Hz. The corresponding thermal time constant is equal to 5.62 ms. Figure 1.20 shows the calculated absorption

spectra versus wavelength. All the previously mentioned approaches to provide multispectral and wavelength tunability require actuation and refractive infix transition. However, these requirements significantly complicate the fabrication, and reduce the resolution of the FPA.

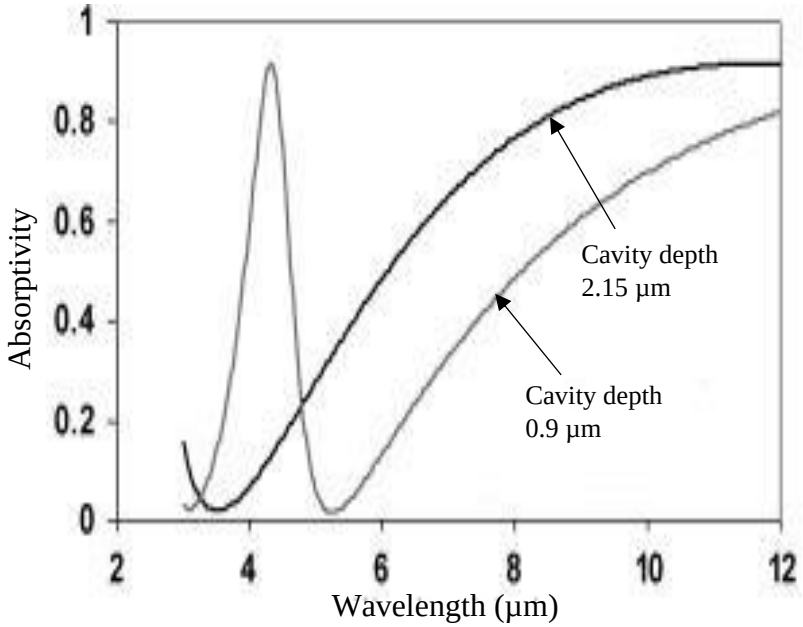

Figure 1.20: Calculated absorption spectra versus wavelength for 0.9 and 2.15 μm cavity depths.

1.4 Metasurface Based IR Materials

Metasurface can be used to control the way a structure interacts with radiation. It was initially developed at microwave wavelengths and it can be scaled down to IR frequencies using microfabrication to optimize the reduced feature sizes [58]. A large selection of metasurface materials have been investigated for applications such as filters, selective absorbers, waveplates, selective thermal emitters, and angular sensitive absorbers. The approach of metasurfaces have been widely used in the infrared detection with different materials and structures. A highly tunable dual-band metamaterial was achieved using asymmetric cross-shaped nanoparticle antenna

separated by a thin MgF_2 layer on a thick gold film [59]. Figure 1.21 Shows the SEM of the fabricated metasurface and the dual band reflected results.

A wide band perfect absorber at midwave infrared using multiplexed metal structure was experimentally demonstrated [60]. Two different metasurface structures were fabricated with multiplexed light absorbers and nonmultiplexed light absorbers in the

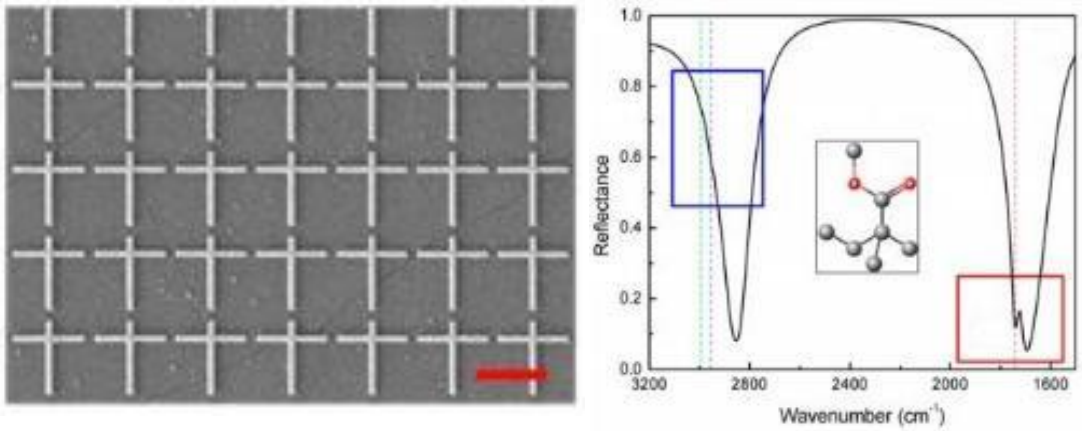

Figure 1.21: Asymmetric cross shaped metasurfaces SEM micrographs with dual band absorption.

midwave IR region. Each nonmultiplexed metasurface with different size resulted in a different band absorption, and the multiplexed structure combined the two bands in one single wider band. Figure 1.22 shows the SEM micrographs of the fabricated metasurfaces and the reflectivity, the dotted blue curve is the power reflection from the perfect absorber structure with one 815 nm gold square in the unit cell. The black dashed curve is the power reflection from the perfect absorber with one 865 nm metal square in the unit cell. The solid red curve is the power reflection from the multiplexed structure perfect absorber with two gold metal squares in the unit cell. A graphene material was investigated theoretically and numerically at the mid infrared regions for a tunable broadband metamaterial absorber graphene based [61]. A broadband

bandwidth of 11.7 THz and an absorption over 90 % was obtained for the proposed metamaterial. The absorber consists of a metal cross metamaterial which is embedded into a graphene plane at the top layer, a dielectric spacer, and a bottom gold film. The absorption is happening due to the coupling effect between the metal and the graphene.

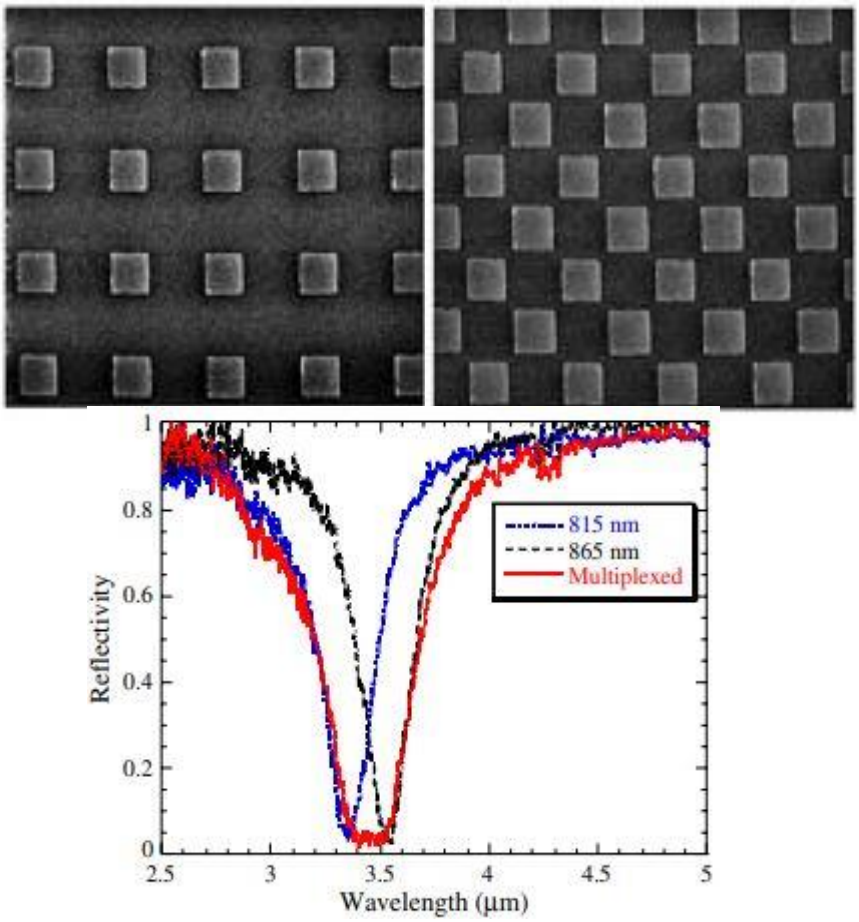

Figure 1.22: Nonmultiplexed and multiplexed SEM micrographs and the resulted IR band reflectivity in the midwave IR region.

The origin of this effect is demonstrated using the two-mode waveguide coupling theory. The Fermi energy of the graphene can be dynamically tuned by changing the external voltage to achieve the tunability of the metamaterial. Figure 1.23 shows the prospective view unit cell of the graphene based metamaterial and different comparison absorbers at normal incidence. Two dimensional plasmonic crystals (2D PLCs)

metasurface material has been studied and investigated [62]. It demonstrated that the absorbed wavelength can be mainly controlled by the period of surface structure. Various types of absorbers for the surface of the two-dimensional plasmonic absorbers

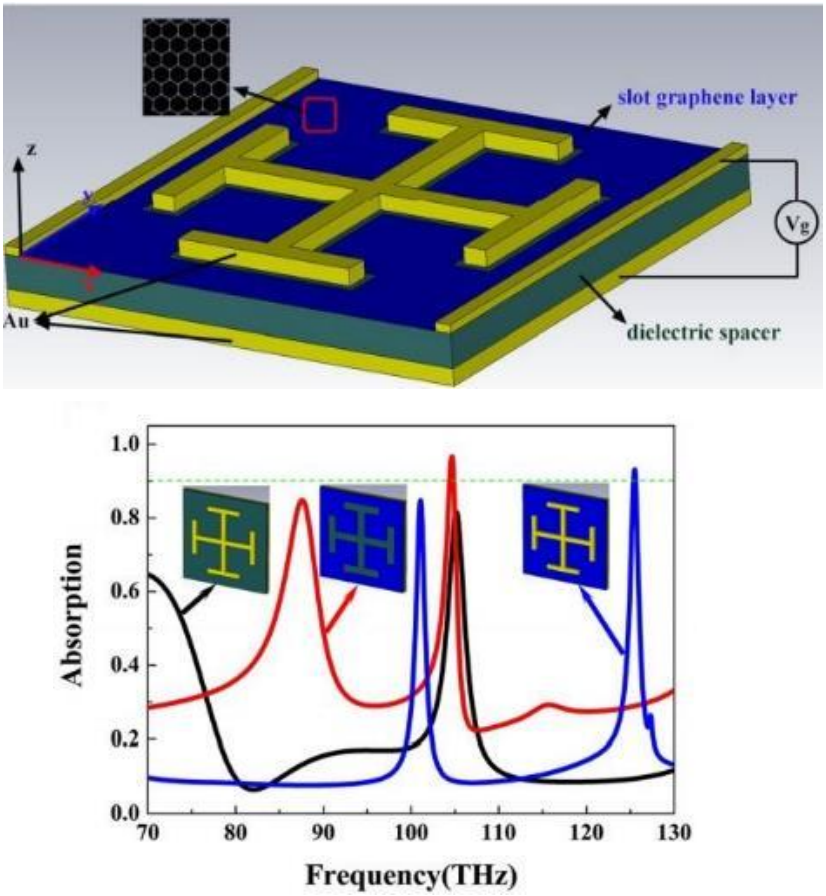

Figure 1.23: (a) Prospective view unit cell of the graphene based metamaterial and (b) Three comparison absorbers at normal incidence.

(2D-Pas) can be chosen, such as Ag, Al, Au, Mo, and W plasmonic metals. Different strong absorption peaks were observed due to the surface plasmon like mode where responsivity is selectively enhanced, and the detection wavelength can be controlled by the period of the 2D-PLC IR absorber. When the period is enlarged from sensors A to D as shown in Figure 1. 24, the responsivity peak shifts to the longer wavelength. The maximum responsivity for 160 mV/W around 5 μm is achieved by sensor C (Figure

1.24). Metal Insulator Metal (MIM) metasurface material was employed to realize spectral tuning [63]. Through-holes were integrated in the MIM structure while

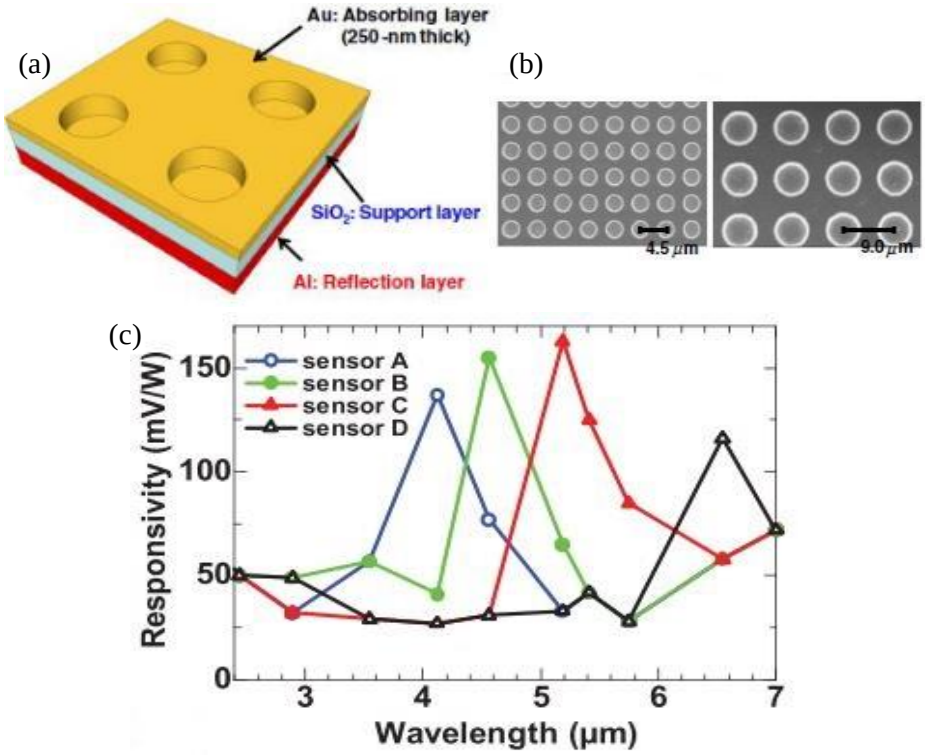

Figure 1.24: (a) Schematic diagram of the 2-d PLA (b) SEM micrographs of the fabricated 2-D PLA and (c) measured spectral responsivities of sensors A to D.

maintaining wavelength selectivity due to the antenna effect. The absorption wavelength can be controlled by the micropatch size and by lesser extent by the periodicity of the metamaterials. Figure 1.25 shows schematic of the through-hole MIM plasmonic metamaterial absorber and the measured reflectance with various micropatch sizes. It can be seen that the reflectance dip corresponds directly to the absorption, since the reflector of the MIM was thick and prevented the transmission, so the absorptance was calculated as 1-reflectance. Another approach to improve the performance of the metamaterial absorbers was using all metal based mushroom plasmonic metamaterial absorbers (MPMAs) [63]. The components forming the MPAM are based on thin films

films of metals such as Au. A promising wavelength-selective absorption was observed over a wide range of MWIR and LWIR wavelengths by the plasmonic resonance of the

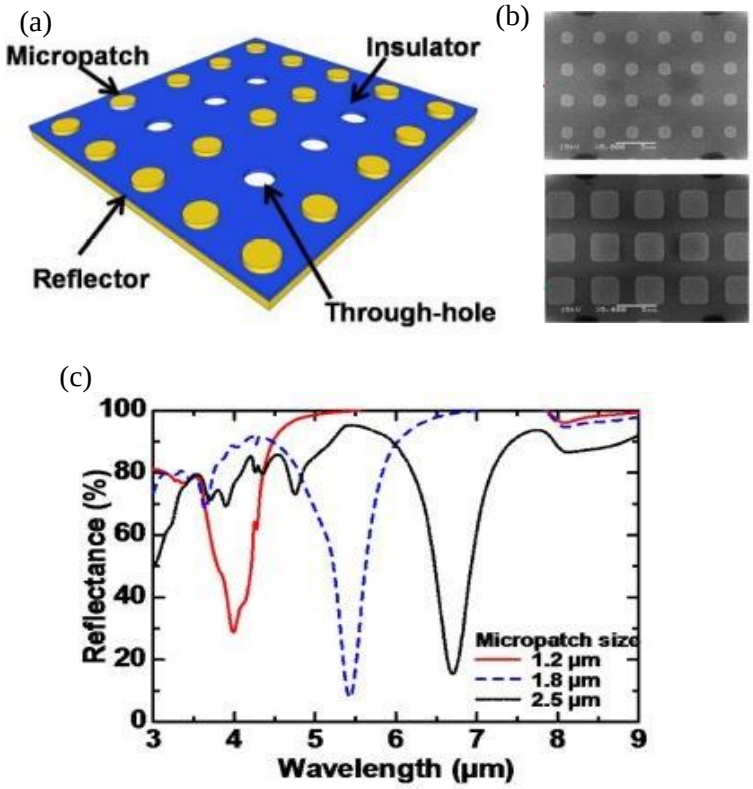

Figure 1.25: (a) Schematic of the Through-hole MIM metamaterial (b) SEM micrographs of the fabricated TH-MIM and (c) Measured reflectance with various micropatch sizes.

micropatch and the narrow-gap resonance. The Si post was fabricated by XeF_2 etching of the Si insulator layer in MIM structures, the width of the post can be varied to tune the single or dual band detections. As shown in Figure 1.26 the results showed that the wavelength selective absorption can be controlled by changing the width and height of the mushroom like metasurface, with strong absorption at 6.4 μm and 9.7 μm with high absorptance over 95%. The MR-PMAs are favorable candidate for high-performance wavelength- or polarization-selective absorbers due to the wide operating ranges in the MWIR and LWIR.

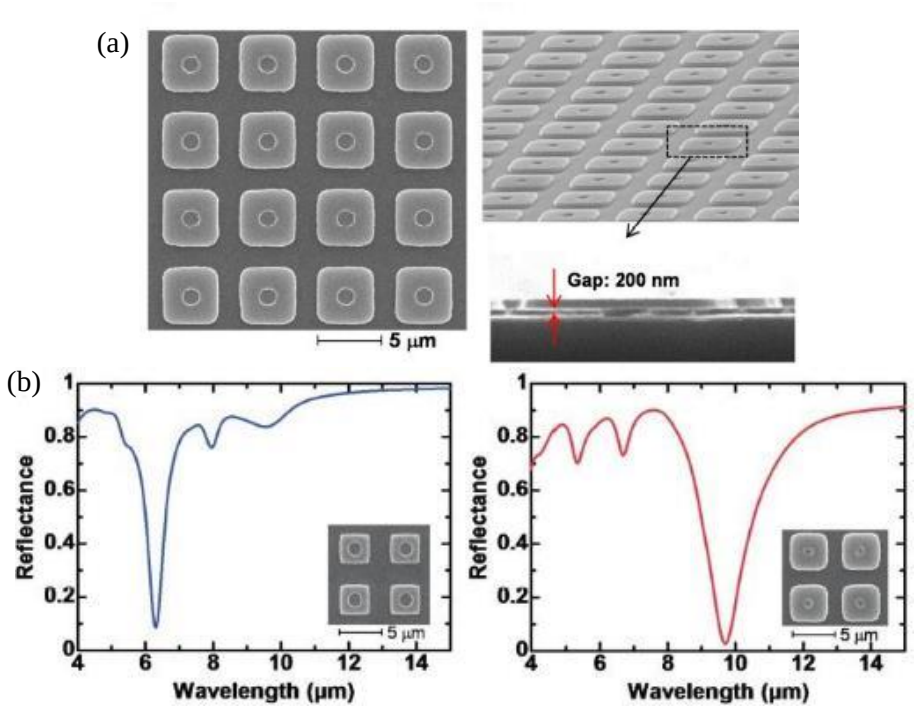

Figure 1.26: (a) SEM micrographs of MR-PMAs with a tubular post and (b) Experimental reflectance spectra with different height and width of the MPMA.

1.5 Metasurface Based Uncooled Infrared Detectors

Metasurfaces, are periodic arrays of sub-wavelength antenna elements. It can be employed to increase the absorptance of the microbolometer. At infrared frequencies, they can be arranged to be a perfect absorber over a narrow-band by matching a structure with a ground plane to free-space [64]. Recently, several groups have begun exploring the potential for applying metasurface concepts to engineer the electromagnetic absorptance by combining the metasurface with microbolometer to achieve spectral selectivity [65]–[74], through the use of metasurfaces. A wavelength-selective metasurface absorber suitable for use in multispectral microbolometer focal plane arrays in the long-wavelength infrared (LWIR) region is theoretically and experimentally investigated as shown in Figure 1.27. The fabricated metasurface absorbers experimentally showed efficient narrowband wavelength-selective

absorption in the LWIR, and three-color spectral responses using different dimensions of the metasurface [75]. A dual band absorption characteristic of a complementary

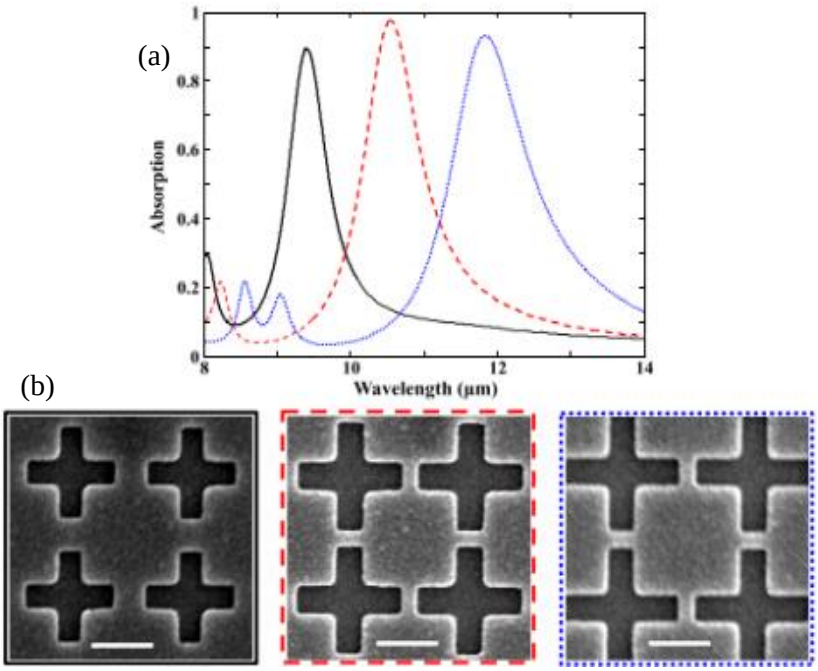

Figure 1.27: (a) Measured spectral response of the three different wavelength-selective metasurface absorbers (b) SEM images of the fabricated metasurface absorbers for different metasurface dimensions [70].

metamaterial was studied in [76]. The diameter of the metamaterial absorbers was varied to obtain different absorption peaks in the measured absorption spectra in the near infrared (1.3-2.5 μm) region as shown in Figure 1.28. Broadband metamaterial absorbers was designed and fabricated to be working in the mid-infrared regime by employing the multilayered metal-dielectric-metal resonant stacks [77]. The absorption bandwidth was effectively broadened through the hybridization of magnetic resonances in all resonant stacks and through using different dielectric stacks on the metamaterial with different resonances as shown in Figure 1.29. The application of metamaterials on bi-material cantilever-based IR FPA was investigated [78] to enhance its IR absorption

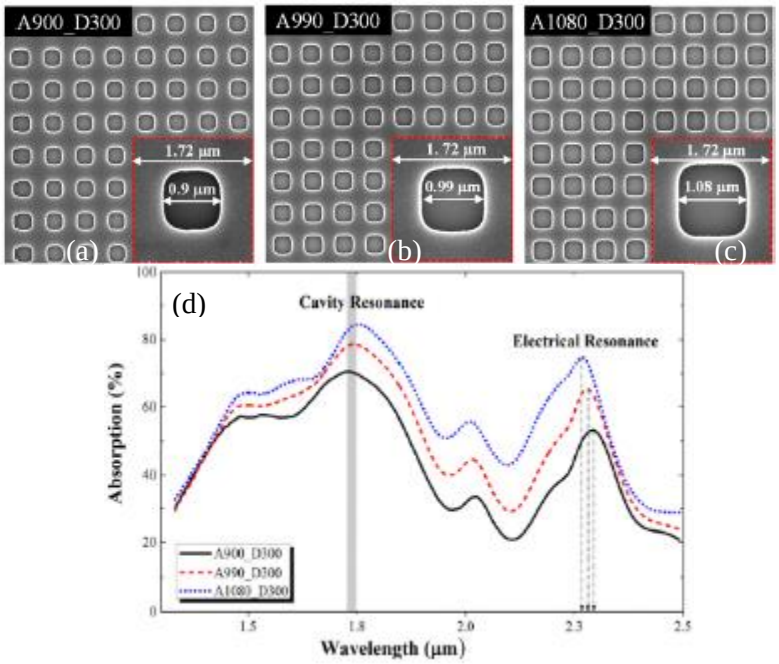

Figure 1.28: SEM micrographs of the three fabricated devices with fixed spacer thickness, d=300 nm and varying metasurface dimensions (a) 900 nm, (b) 990 nm, and (c) 1080 nm, (d) measured absorption spectra of the three fabricated devices.

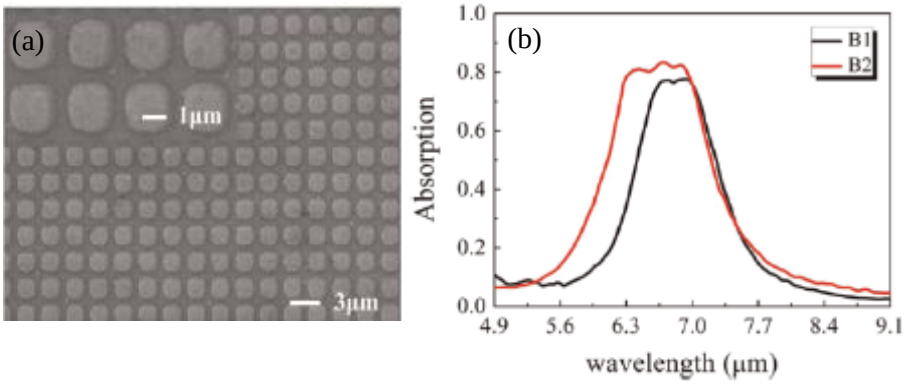

Figure 1.29: (a) SEM micrograph of the fabricated sample. (b) Measured absorption spectra for a structure composed of two resonant stacks.

and consequently the detector responsivity. Four absorptions peaks were observed, where two were located in the long-wavelength IR band with the absorption of 90.1% at 7.6 μm and 79.5% at 13.8 μm, respectively, as shown in Figure 1.30. Also, the metasurfaces were used in plasmonic and it showed the ability to control and

manipulate light at unprecedented levels, leading to exciting optical functionalities and applications. The combination of nano plasmonic and piezoelectric resonances allowed

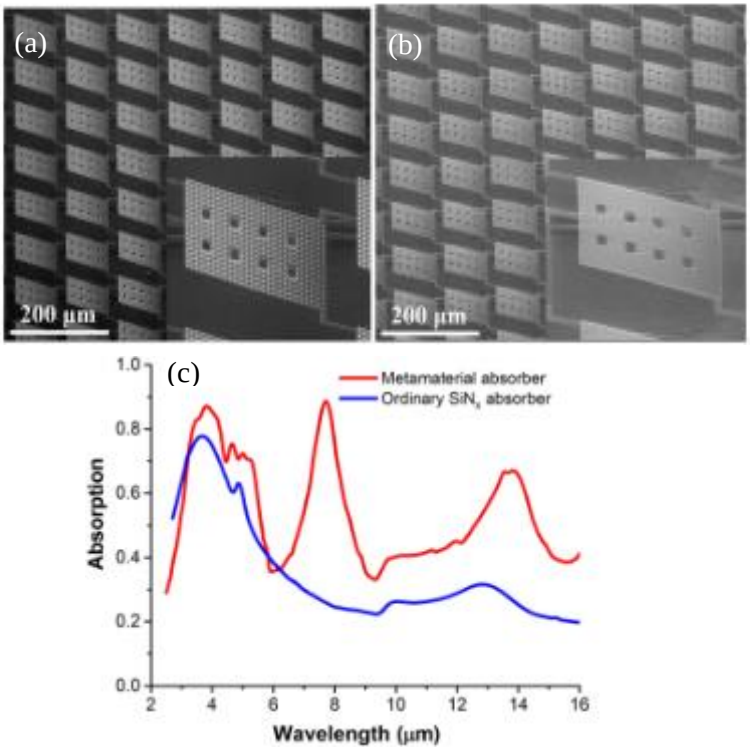

Figure 1.30: SEM images of the fabricated Focal Plane Array (FPA) with (a) and without (b) metasurface absorbers. (c) Measured absorption spectra.

the proposed device to selectively detect long-wavelength infrared radiation with unprecedented electromechanical performance and thermal capabilities [79]. These attributes lead to the demonstration of a fast, high-resolution, uncooled infrared detector with 80% absorption for an optimized spectral bandwidth centered around 8.8 µm as shown in Figure 1.31. In addition, metasurface absorber microbolometer were constructed via the integration of a resonant metamaterial absorber microbolometer sensor [80]. The single absorber has a narrow absorption peak at 2.56 THz and an absorption magnitude of 55%. The three-layer of the electric ring resonators (ERR) structure has a broad absorption peak of magnitude 80% at 2.56 THz while at 2.52 THz the absorption magnitude was 78% as shown in Figure 1.32. Many of the proposed

devices require patterning features below 400 nm. These metasurface disks can be arranged to be an excellent absorber (near unity absorptance over a narrow-band) by matching a structure with a ground-plane to free-space [81]–[86].

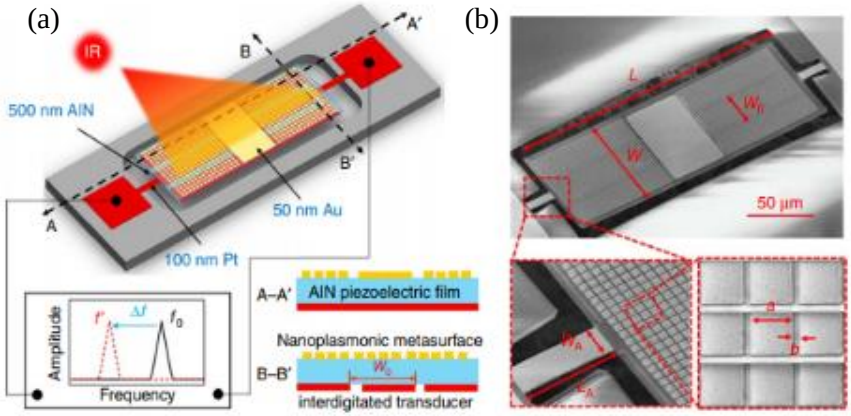

Figure 1.31: (a) 3D view of the device showing the interdigitated electrode (b) SEM images of the resonator .

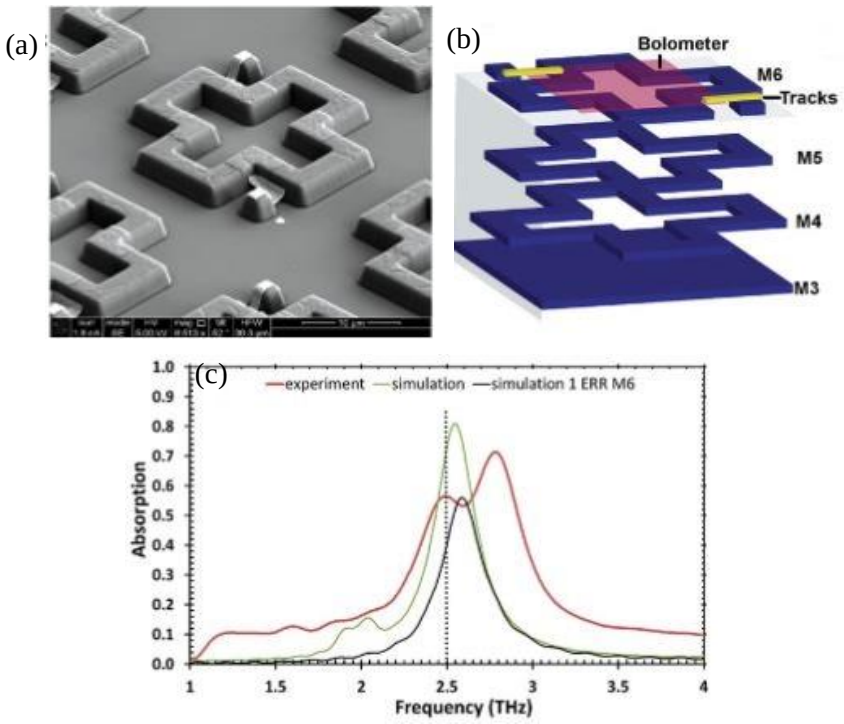

Figure 1.32: (a) SEM micrograph of the (EER), (b) 3D schematic diagram of the monolithic resonant terahertz detector, and (c) Experimental and simulation results.

CHAPTER 2: BACKGROUND THEORY

This chapter presents a brief overview of the main infrared detectors. It also explains the figure of merits of the uncooled microbolometer, including the voltage responsivity, the voltage detectivity, the temperature coefficient of resistance, and it explains the sources of noise that impact the microbolometer performance.

2.1 Infrared Detectors

2.1.1 Photon Detectors

Photon detectors are devices used for the detection of light by counting the photons of the light. A photon detector surface absorbs the photons and produces electrical effect (current, voltage) proportional to the number of absorbed photons [87]. Figure 2.1 shows the Photovoltaic cell configuration. There are four main configurations of photon detectors: the PIN photodiode, the avalanche photodiode (APD), the Schottky barrier photodiode, and the photoconductor [88].

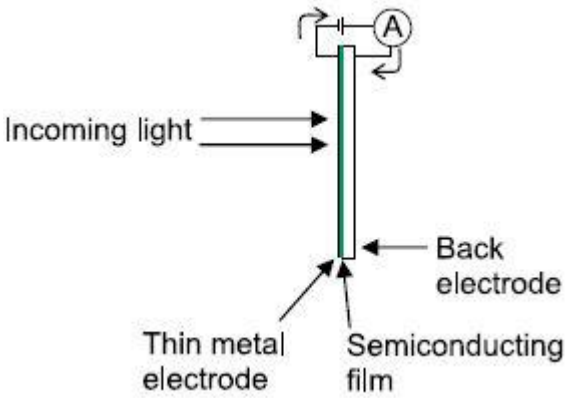

Figure 2.1: Photovoltaic cell configuration.

The mechanism of photon detectors is based photoexcitation, which implies generation of free carriers in the detector. The photons, through photoconductive or

photovoltaic effect, are converted into electron-hole pairs in which the photon has the energy equal or greater than the band gap energy of the material, E_g [89]. Mathematically this can be expressed as (1):

$$h\nu \geq E_g \tag{1}$$

Where ν is the optical frequency of the photon in Hz and ħ is the Plank constant. ν can be expressed $\nu = c\lambda$, where c is the speed of the light λ is the wavelength. The lowest energy photon can be detected at the wavelength (cut-off) λc is expressed by (2,3):

$$\lambda_c = \frac{h_c}{E_g} \tag{2}$$

$$\lambda_c(\mu m) = \frac{1.238}{E_g(eV)} \tag{3}$$

For photon detectors, the cutoff wavelength is determined by materials energy gap. For materials with smaller energy gap, electrons are thermally excited into the conduction band, which results in unwanted dark current. The dark current along with its shot noise can be minimized by cooling the detectors cryogenically. However, the addition of a cooler increase the cost of photon detectors. The majority of semiconductor materials suitable for photon emission are based on a combination of elements in the third group of the periodic table such as Gallium Arsenide (GaAs), Silicon, Lead Sulfide (PbS), Indium Antimonide (InSb), Lead Selenide (PbSe), and used as photon detectors.

2.1.2 Thermal Detectors

Thermal detectors are light detectors which are based on measuring light-induced temperature rise. The temperature in the thermal detector changes due to the absorbed radiation. This temperature change causes difference in some measurable quantities

such as resistance, voltage, capacitance, or inductance [90].

Thermal detectors are used for applications that does not require high speed and high sensitivity. The most substantial advantage of thermal detectors over photon detector is that they can achieve wider spectral window and exhibit a nearly constant responsivity over broader spectral regions [91], [92] . A thermal detector comprises an absorber which is thermally insulated from the substrate (heat sink) to give a big temperature change upon incident radiation. Several physical mechanisms can be used to measure this change in temperature [93]. The main types of detection mechanisms are briefly described below.

Thermopile detector is an electronic device that converts thermal energy into electrical energy. The detector works on the principle of thermoelectric effect, which generates voltage when its dissimilar metals experience a temperature difference. It consists of a series of thermocouple pairs with a junction located on either side of a thermal resistance layer [94]. The output from the thermocouple pair output voltage is proportional to the temperature difference and the heat flux across the thermal resistance layer. Connecting thermocouple pairs in series increases the magnitude of the voltage output. Thermopiles can be constructed with a single thermocouple pair, composed of two thermocouple junctions, or multiple thermocouple pairs [95]–[100].

Pyroelectric detector is a thermal detector that produces temperature fluctuations when it interacts with infrared radiation. This temperature fluctuation results in a charge change on the surface of pyroelectric crystals, which produces a corresponding electrical signal. Pyroelectric crystals are asymmetry due to their single polar axis, which causes the polarization to change with temperature [101]. When the crystal is heated and cooled, a surface charge with opposite polarity is created. Pyroelectric

detectors can only operate in AC mode, as free charges will cancel the obtained polarization in DC [102].

2.2 Microbolometer Detector

A microbolometer is an element whose resistance changes with temperature, associated with the absorption of IR radiation. In operation, it requires a current bias and a modulated IR source for determining and producing a time varying signal in accordance with ohm's law. The rate of heat transfer is an important factor in determining the speed of thermal detection process. The reduced thermal mass of the microbolometer will result in heating up the sensing layer faster. Figure 2.2 shows the basic principle of microbolometer operation. The separation of sensing material from the substrate will reduce both the thermal mass and heat loss. After heating the detector

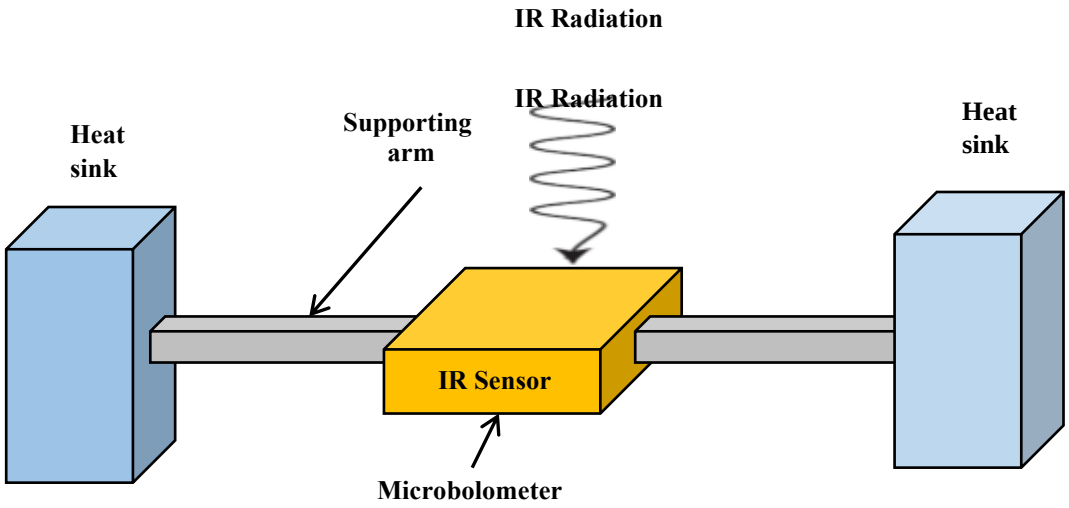

Figure 2.2: Microbolometer with thermal isolation concept.

element above the ambient temperature, the temperature gradient serves as the driving force for the heat flow. There are three main conduction mechanisms in the thermal detectors, i.e., conduction, conviction, and radiation. The conduction mechanism is the

dominant one. The conduction mechanism occurs through the support arms and the substrate (heat sink). Therefore, the electrode arms must be carefully designed and fabricated to reduce the thermal conductance path to thermally isolate the IR sensitive layer from the heat sink, i.e., the substrate. This will reduce the rate of heat loss and hence increase the sensitivity of the detector. The conviction mechanism occurs in the presence of a surrounding atmosphere. Thus, the device should be packaged in vacuum to reduce the heat loss. The detector is at the background limit if the principal heat loss mechanism is radiative. The temperature change of the thermometer area of a pixel when radiation falls on the pixel can be described by solving the heat flow equation (4):

$$C\frac{d(\Delta T)}{dt} + G(\Delta T) - \eta P_o e^{jwt} = 0 \tag{4}$$

Where, $\Delta T = T_D - T_O$ is the difference between the detector temperature T_D and the ambient temperature of the heat sink T_o, C is the heat capacity or thermal mass (J/K), G is the total thermal conductance to the substrate (heat sink), which is usually dominated by the thermal conductance of the support structure (W/K), P_o is the total radiation power amplitude falling on the pixel (W), η is the fraction of the incident radiation absorbed, ω is the optical modulation frequency, and t is time. The equation is given by (5):

$$\Delta T = \frac{\eta P_o}{G(1+\omega^2\tau_{th}^2)^2} \tag{5}$$

Where τ_{th} is the thermal response time (s), defined by the ratio of the device's thermal mass to its thermal conductance, ω is the optical modulation frequency. The thermal conductance G_{th} between the microbolometer and its surrounding is measured via the method of resistive or Joule heating [103]–[106].

2.3 Figure of Merits of the Microbolometer

The performance of the uncooled microbolometer is characterized by multiple figure of merits including the voltage responsivity, detectivity, noise equivalent temperature difference, and temperature coefficient of resistance (TCR) [107].

2.3.1 Voltage Responsivity

One key figure of merits to consider when designing and optimizing uncooled microbolometer performance is voltage responsivity R_v. Responsivity is the ability of the device to convert the incoming radiation into an electrical signal. The detector output signal may be current or voltage. Thus, the voltage responsivity, R_v, is defined as the detector output voltage per unit of detector input power [108] (6):

$$R_v = \frac{\eta \beta I_b R}{G\sqrt{1 + \omega^2 \mathcal{T}_{th}^2}} \tag{6}$$

where η is the absorptivity, β is the TCR of microbolometer, I_b is the bias current, R is the temperature dependent resistance of the device, G_{th} is the thermal conductance, τ_{th} is the thermal time constant of the microbolometer. The voltage responsivity is expressed in V/W.

2.3.2 Detectivity

Detectivity, D*, measures the signal-to-noise ratio and normalizes the performance of the detector with respect to the detector size. It has the unit of cm-$Hz^{1/2}$/W. It can be expressed by (7):

$$D = \frac{R_v \sqrt{A\Delta f}}{v_n} \tag{7}$$

Where Vn is the total noise voltage observed in the electrical bandwidth Δf, A is the area of the detector [109].

2.3.3 Temperature Coefficient of Resistance

The Temperature Coefficient of Resistance (TCR) shows how rapidly the resistance of a material responds to a change in temperature. The performance of the microbolometer can be improved significantly when the IR sensing material has a high TCR value, acceptable resistivity value and a low voltage noise. The TCR can be determined by (8):

$$TCR = \frac{1}{R(T)} \frac{dR(T)}{dT(T)} \tag{8}$$

Where R(T) is temperature dependent resistance of the thin films at temperature T. The R(T) can be expressed in terms of activation energy Ea and temperature T (9):

$$R(T) = R_o \, exp \left(\frac{Ea}{K_B T}\right) \tag{9}$$

Where R_o is an Arrhenius perfector and is constant. plugging equation (8) in equation (9), results in (10):

$$TCR = -\frac{E_a}{K_B T^2} \tag{10}$$

By taking the natural logarithm on both sides of equation (9), leads to (11):

$$ln\big(R(T)\big) = E_a \frac{1}{K_B T} + ln(R_o) \tag{11}$$

This is a linear equation. The ln(R(T)) versus $1/K_BT$ plot is a straight line with a slope equal E_a.

The conduction mechanism in amorphous semiconductors can be best described and represented by the model developed by Mott [110]. These localized states are also called band tails, which are formed due to the disorder. Another set of states is formed in the mid-gap due to point defects in the structure of the semiconductor. Several different conduction mechanisms are possible, but for the material of interest around

room temperature the dominant conduction mechanism is mostly the excitation of carriers from the mid-band states into the localized band tails and hopping within the band tail states. The electrons are localized close to the Fermi level and conduction can occur by extended state conduction and band tail conduction [111].

2.4 Noise Sources of the Microbolometer

Noise Power Spectral Density (PSD) describes the power present in the signal as a function of frequency, per unit frequency power. PSD is expressed in Watts per hertz (W/Hz). It is an unavoidable part of any electronic circuits or devices. The noise is unwanted, and it degrades the quality of devices and systems by interfering with the original signal. It is also defined as the random and uncorrelated fluctuations in current, and voltage of physical quantity. It is expressed as (S_v) (12):

$$S_v = \frac{V_n^2}{\Delta f} \tag{12}$$

Where V_n is the noise voltage (RMS) and Δf is the frequency bandwidth. The nature of the materials that are used in the microbolometer exhibit some noise and it cannot be eliminated from the device or system [112]. Schottky predicted the occurrence of frequency-independent white noise in 1918 [113]. Awhile after , Johnson successfully measured it but faced unexpected “flicker” noise at low frequency referred to as 1/*f*-noise [114]. This low-frequency 1/*f*-noise decreases the performance of semiconductor devices that operates mainly at low frequencies. In order to allow the detector to reach the background limited noise performance, a reduction of the noise level must be considered to improve the new generation of uncooled thermal cameras. There are several types of noise that exist in the uncooled microbolometer: which include the noise generated by the sensitive element (Johnson noise), 1/*f*-noise, temperature

fluctuation noise, shot noise, background noise, and random telegraph noise [115], [116]. The total voltage noise can be expressed as the sum of squares of noise contributions due to Johnson noise, 1/*f*-noise, temperature fluctuation noise, and background noise.

2.4.1 Flicker Noise or *1/f*-noise

Flicker noise or 1/*f*-noise is observed at low frequencies [117], often because of the fluctuations that take place in both carrier concentration and carrier mobilities originated from carrier trapping and de-trapping mechanisms and surface state scattering. The 1/*f*-noise also depends on the employed deposition techniques, materials, and dimensions and electrical contacts. Another prospective of 1/*f*-noise is its own volume dependency. Therefore, increasing the thickness of the IR sensitive film will result in reducing the noise level significantly. However, this will result in large thermal mass and lower performance of the microbolometer and a larger thermal time constant [118]. The electrical noise increases at lower frequencies due to the increase contribution of 1/*f*-noise, while at high frequencies reaches to Johnson noise [119]. The 1/*f*-noise can be determined using Hooge's empirical equation [120] (13):

$$S_{\frac{1}{f}} = \frac{K_f (I_b R)^{\beta}}{f^{\gamma}} \tag{13}$$

Where $S_{1/f}$ is the voltage noise PSD f^{γ} is the electrical frequency with γ close to 1 for 1/*f*-noise [121], K_f is the 1/*f*-noise coefficient. It is given by $\alpha_{H/N}$, where α_H provides the magnitude of 1/*f*-noise, *N* is the number of fluctuators in the sample which is volume dependent. Thus, K_f is dependent on the volume normalized inherent noise and Its affected by the quality of the crystal and the scattering mechanisms, I_b is the bias current and R is the resistance of the device [120]. The product $I_b \times R$ is the applied DC bias

voltage (V_{DC}) with the ideal value of β is 2 indicating that by doubling the DC bias current it doubles the PSD voltage noise. The ideal value of γ is 1 indicating that 1/*f*-noise is the dominant noise at low frequencies. The values of γ, β, and K_f were determined by taking the logarithm of equation (14):

$$log_{10}\left(S_{\frac{1}{f}}\right) = \beta log_{10}(I_B) - \gamma log_{10}(f) + log_{10}(k_f) + \beta log_{10}(R) \qquad (14)$$

This is a straight-line equation with the slope equals β, and the last two terms are constants for a specific frequency. To calculate the value of β, we plotted Log_{10} ($S_{1/f}$) as a function of log_{10} (I_B) using 1, 5 and 10 Hz for 3 bias currents. We first determined the slope (β) for each current and then the average β was calculated by taking the average of the slopes for the 3 bias currents. Similarly, the value γ was calculated from the average slope of log_{10} ($S_{1/f}$) versus log_{10} (f) plots for the same 3 bias currents in the frequency range 1-10 Hz. The average value of K_f was determined by substituting the calculated value of γ and β for each bias current into equation (13) at 10 Hz.

2.4.2 Johnson Noise

Johnson noise or thermal noise is an electronic noise generated by the thermal agitation of the charge carriers (usually the electrons) inside an electrical conductor at equilibrium, which happens regardless of any applied voltage. The motion of the carriers in any resistive element causes a thermal motion without any direct current flow in the material. The thermal motion of the carriers leads to fluctuating charge gradients across the resistor. Mathematically Johnson noise is given by (15):

$$v_j^2 = 4k_BTR \qquad (15)$$

Where T is the resistors absolute temperature in kelvins and *R* is the resistance of the detector in ohms. K_B is Boltzmann's constant in joules per kelvin.

2.4.3 Background Temperature Noise

Background temperature noise (V_{BG}) arises from the radiative heat exchange between the microbolometer at temperature, T_d, and the surrounding environment at temperature T_b [122] and its expressed by (16):

$$V_{BG}^2 = \frac{V_{BG}^2}{\sqrt{f}} = \frac{(I_b R\beta)^2[8A\eta\sigma K_B(T_d^5 + T_b^5)]}{G^2(1+\omega^2\tau^2)} \tag{16}$$

Where T is the temperature of the detector and K_B is Boltzmann's constant, G is the thermal conductance.

2.4.4 Temperature Fluctuation Noise

This kind of noise in the uncooled microbolometers arises from the fluctuations in the heat exchange between the heat sink and the isolated detector. It is also called thermal fluctuation noise due to the variance in temperature caused by the temperature fluctuation [122], It is given by (17):

$$V_{TF}^2 = \frac{\Delta V_{TF}^2}{\Delta f} = \frac{(2I_b R\beta T)^2 K_B}{G(1+4\pi^2 f^2\tau^2)} \tag{17}$$

The summation of total individual noise represents the total microbolometer noise and it is given by (18):

$$V_n^2 = V_j^2 + V_{1/f}^2 + V_{BJ}^2 + V_{TF}^2 \tag{18}$$

The performance of the microbolometers can be improved substantially and reach the temperature fluctuation noise performance if the noise is eliminated or reduced. Our uncooled microbolometer have mainly been operated in the regime where Johnson noise is the dominant noise and 1/*f*-noise is the dominant noise at low frequencies. We

have studied and reduced voltage noise PSD and 1/*f*-noise by different annealing techniques including vacuum annealing and forming gases annealing at 300 ^{o}C.

2.5 Metasurfaces

Metasurfaces are composed of periodic subwavelength metallic/dielectric structures that resonantly couple to the electric and magnetic fields of the incident electromagnetic waves, exhibiting unprecedented properties. They are a novel class of functional materials that are designed around unique micro-and nanoscale patterns or structures, which cause them to interact with light and other forms of energy [123], [124]. Their structures enable properties and capabilities that is mostly unavailable to obtain using conventional material discovery or manufactures technologies. Metasurfaces are networks of antenna elements that permit electromagnetic scattering from an engineered structure. Over the past decade, metamaterial have developed from being only a theoretical concept to the research field and marketed applications. Three dimensional metamaterials can be extended by arranging electrically small scatterers or holes into a two-dimensional pattern on a surface interface. The metasurface name has been given to the surface version of the metamaterial (the term metafilm has also been employed for certain structures). They have the advantage of seizing less physical space than full three-dimensional metamaterial structures. Therefore, metasurfaces offer the possibility of less-lossy structures. They can be fabricated using standard lithography techniques. They have been used widely with uncooled infrared detectors to improve the electrical performance of the detector and to provide spectral selectivity which cannot be achieved by the conventional microbolometer.

Spectral selectivity can also be achieved using Fabry-Perot cavity where multiple pixels used in focal plane array (FPA) must be fabricated with different cavity heights.

This poses significant manufacturing challenge. Several groups have experimented with dynamically tuning the microbolometer's cavity, either through piezoelectric actuation [79], electrostatic actuation [54], liquid crystal based changes in the refractive index [125], or by using movable micromirror underneath the microbolometer pixel [56], [126], [127]. These approaches provide the ability to tune the wavelength response. However, the actuation requirements significantly complicate the fabrication, and reduce the resolution of the FPA.

An alternative to change the height of the cavity is to use metasurface to control the spectral response. This approach has been recently explored using metasurface elements including asymmetric cross-shaped nanoparticle antenna [128], multiple metamaterial structure in a single device or unit cell [129], 2D absorber with Au dimples [130], split ring resonators [131], and 1D and 3D metal-insulator-metal devices with a through-hole [132], a metal cross pattern into a graphene layer [61], plasmonic crystal absorbers [63], and many others [76], [133], [134]. In his project, we have used the Metasurfaces to improve the temperature coefficient resistance, lower the resistance of the microbolometer, and to provide spectral selectivity by changing the geometry of the fabricated metasurface.

CHAPTER 3: MICROBOLOMETER DESIGN

This chapter presents the design process of the uncooled microbolometer for infrared detection, and the interaction of the metasurface with the microbolometer in the Long Wavelength Infrared Radiation (LWIR).

3.1 Metasurface Design

We have selected a metal-insulator-metal (MIM) configuration in order to achieve a perfect absorption at the desired resonant wavelength over a narrow-band in the long wavelength region (LWIR). The MIM configuration is accomplished by embedding the $Si_xGe_yO_{1-x-y}$ semiconducting layer between the metasurface (also known as FSS) circular disk array and a thin dielectric layer of SiO_2, which electrically isolating $Si_xGe_yO_{1-x-y}$ from an Al ground plane. This structure is equivalent to a composite material with an effective impedance that can be engineered by adjusting the disk array geometry rather than the material composition. In this case, the metasurface geometry provides a spectrally selective absorptivity. This configuration permits the insulator to be significantly thinner than quarter waver resonant cavity and thus reduces the thickness of the dielectric layer which is critical to minimize the thermal mass of the microbolometer. Incident electromagnetic (EM) energy with the correct characteristics is converted to heat by the metasurface. When the metasurface is coupled to a microbolometer platform, the resulting FPA can resolve attributes of the scene beyond the intensity of the incident radiation.

The objective is to design a perfect IR absorber at a desired wavelength. This can be accomplished by integrating the metasurface disks into the sensing layer.

Metasurfaces are networks of antenna elements that permit electromagnetic scattering from an engineered structure. Metasurfaces have been used in photonic crystals, RF interference mitigation, strain sensing and structural health monitoring [135]–[137]. They are circular disks patterns arranged on a hexagonal close packed lattice. This geometry was chosen since the disks are comparably large and easier to fabricate using conventional lithography techniques than other shapes such as squares and crosses. After simulation, the disks were built into finite pixel models of the microbolometer. The geometry of the metasurface absorber is shown in Figure 3.1. Geometric parameters representation in which (p) is the periodicity of the metasurface and (d) is diameter of the metasurface disk. When the wavelength is equal to the period of the metasurface, higher order diffraction will be observed. The diameter of metasurface disk is related to the resonant wavelength in order to get resonance in infrared range; since we focus on the wavelength range between 8-14 μm, the diameter in the range of 1-3 μm is used. The metasurface disk array is made of (75 nm) thick gold. The gold material was selected because of its minimal losses in the IR which reduces the bandwidth of the resonant mode. The disk diameter and periodicity were simulated and

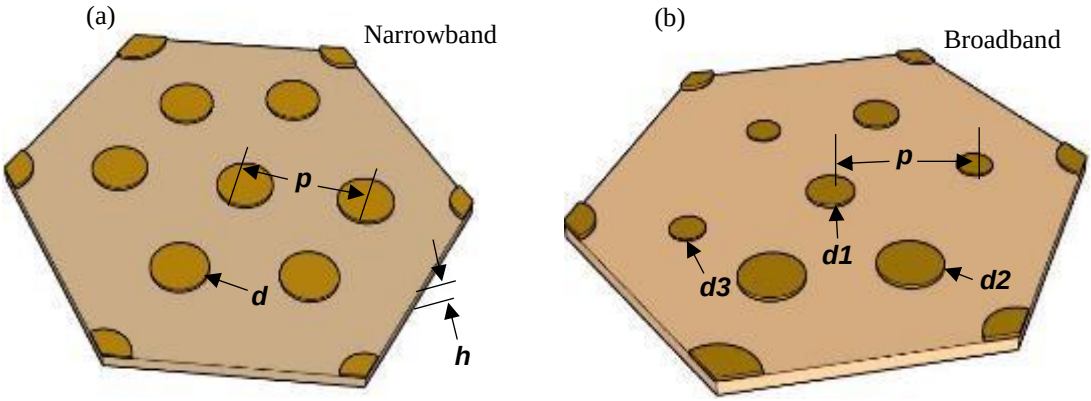

Figure 3.1: The geometry for the metasurface absorbers for (a) Narrowband with the same metasurface diameters and (b) Broadband with different metasurface diameters.

optimized to achieve unity absorptance at distinct wavelengths in the LWIR. The magnitude of the absorptance depends on the impedance matching that can be achieved by adjusting the periodicity, while the resonant wavelength is highly depended on the disk diameter. In general, the bandwidth decreases with larger periodicity.

3.2 Design I: Single Cavity Microbolometer

3.2.1 Device Design and Mask layout

The microbolometer is designed with pixel sizes of 40×40 μm^2 and 25×25 μm^2 A 3-D view of a single microbolometer design is shown in Figure 3.2. It consists of a thin Si_3N_4 bridge suspended above a silicon substrate. The bridge is supported by two narrow arms of Si_3N_4 and NiCr. The arms serve as support structures, conductive legs, and thermal isolation legs. The Si_3N_4 was chosen for its excellent thermal properties and high infrared absorption. The $Si_xGe_yO_{1-x-y}$ sensing layer was sandwiched between the Al metasurface disk array and a layer of SiO_2 separating $Si_xGe_yO_{1-x-y}$ from an Al ground plane and patterned on center of the Si_3N_4 bridge. NiCr was used as the contact and electrode material as it makes excellent contact with Si-Ge-O resulting in linear behavior, and it has a relatively low thermal conductivity, providing better thermal isolation. A gold (Au) thin film was patterned under the polyimide sacrificial layer to define the traces and the bonding pads. The microbolometer was fabricated by sputtering the device layers on top of the polyimide sacrificial layer. Subsequent etching of the sacrificial layer provides the air gap that thermally isolates the microbolometer. The objective of the metasurface is to absorb the maximum amount of radiation over one band (8-14 μm) while reflecting the other portions of the spectra. The pixel and the supporting bridge are designed with low thermal mass and low thermal conductance to reduce the thermal time constant and maximize the responsivity and detectivity. The

$Si_xGe_yO_{1-x-y}$ sensing layer was sandwiched between the metasurface and a layer of Si_3N_4 separating Si_xGeyO_{1-x-y} from an Al ground plane. There is no ¼-wave cavity which provides additional freedom for future support leg design.

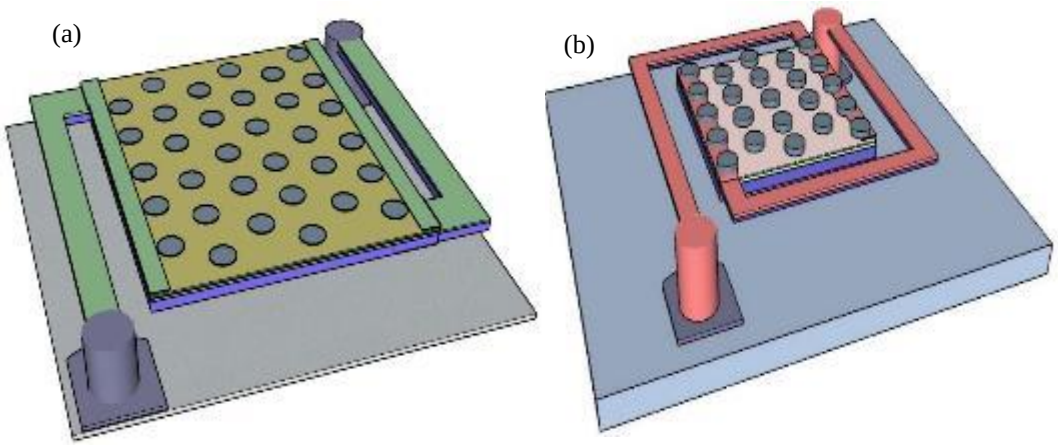

Figure 3.2: The designed microbolometer showing the metasurface on top of the sensing layer for (a) 40×40 μm^2 and (b) 25×25 μm^2.

The layout of the microbolometer was designed to implement the fabrication process of the microbolometer. A set of four-inch quartz masks were used to translate the pattern from the mask to the device for each layer. The transformation of the mask pattern can be either the exact copy or a reverse copy depending on the used photoresist type. If a positive photoresist is used, then the exact pattern will be transferred to the wafer and if the used photoresist is negative, the reverse pattern will be transformed to the wafer. The pattern on the mask was drawn using L-edit v14.1 software and fabricated by an external company. The pattern on the mask is made of a thick layer of chromium. A total of 6 masks were used to fabricate the microbolometer on a 3" oxidized silicon wafer as shown in Figure 3.3. Mask 1 is used for electrical traces and bonding pads patterning, mask 2 is used to pattern the holes for the microbolometer anchors through the Polyimide sacrificial layer, mask 3 is used to pattern the support structure to hold the microbolometer, mask 4 is used to pattern the pixel layer, mask 5

is used to pattern the electrical contacts, and mask 6 is used to pattern metasurface discs for the narrowband and broadband design .Each wafer consists of 160 dies, with a total of 6,400 device in one wafer. metasurface unit cell consists of metasurface element, semiconductor, dielectric, and ground plane, which is equivalent to a composite material such that the geometry determines the ensemble properties. The objective of

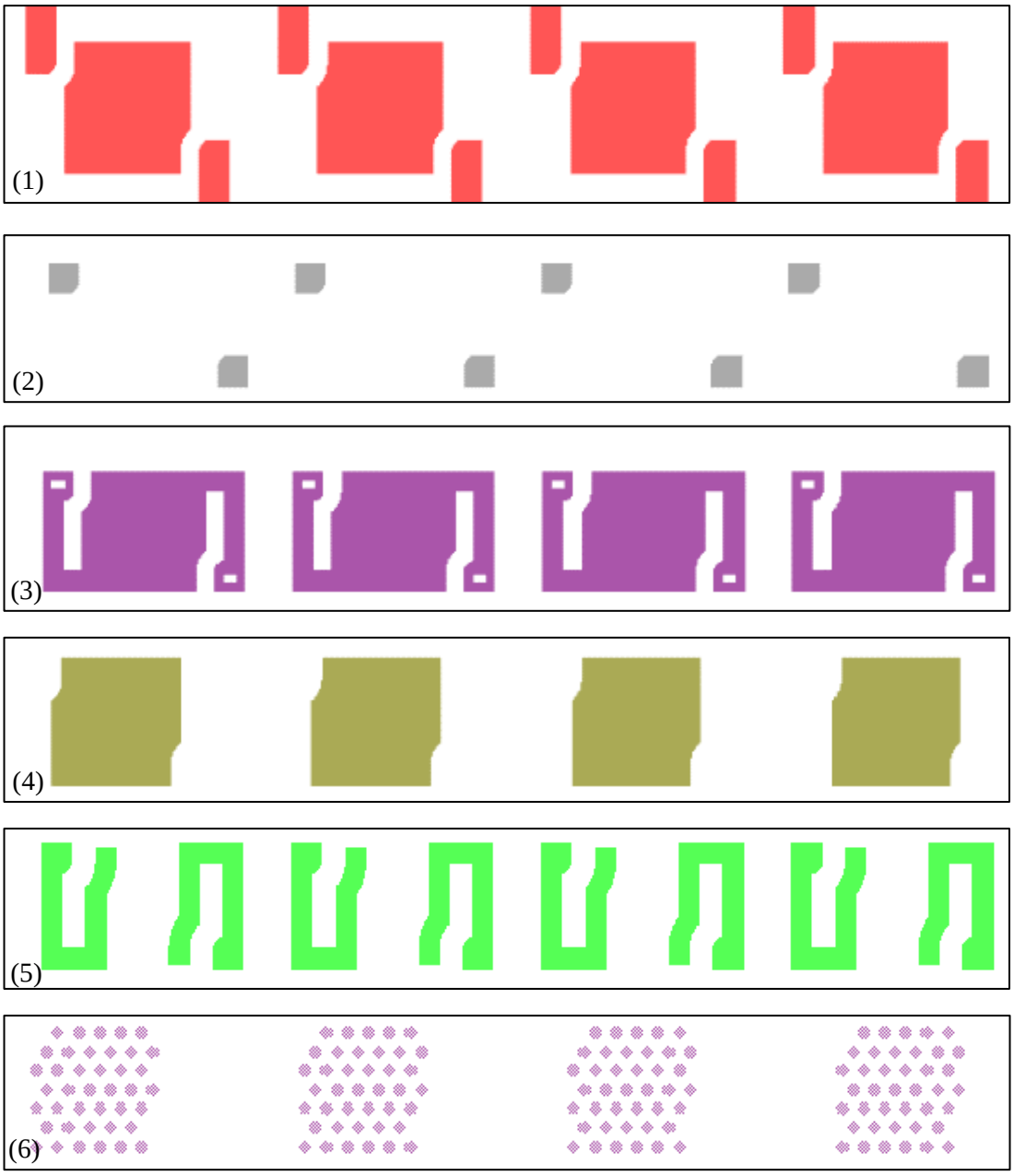

Figure 3.3: Shows the six different masks that are used to fabricate the single cavity microbolometer.

the metasurface is to absorb the maximum amount of radiation over one band (8-14 μm) while reflecting the other portions of the spectra. The pixel and the supporting bridge are designed with low thermal mass and low thermal conductance to reduce the thermal time constant and maximize the responsivity and detectivity.

3.3 Deign II: Two-Microbolometer Stack

3.3.1 Device Design and Layout

In the second design, we have designed the device with Two-microbolometer stack and with dual-air cavity, fabricated on top of each other as shown in Figure 3.4. Each microbolometer captures a portion of the spectrum in order to maximize the IR absorptance over two distinct spectral windows in the LWIR. To demonstrate this concept, we synthesized a device with two spectral regions between λ=8-14 μm atmospheric transmission. The bottom microbolometer has a metasurface that selectively absorbs radiation between λ=8-14 μm, while reflecting radiation outside this range. The top structure is designed with a resonant Fabry-Pérot cavity located between the top microbolometer pixel and the bottom metasurface in order to absorb incident radiation between 7.5-9 μm and transmit any unabsorbed radiation outside this window. The metasurfaces, a class of perfect absorber, can be engineered to provide an impedance match to free-space for radiation with specific attributes. Metasurface perfect absorbers generally consist of a metallic antenna element separated from a metallic ground plane by a dielectric layer. The geometry of the antenna elements determines the absorptance conditions. For example, linear dipoles can be designed to respond only to radiation parallel to the dipole and the resonant wavelength scales with the size of the element. The two-band design can be used to measure the absolute temperature of an object by comparing the relative signals in the two spectral bands.

This approach will perform significantly better than a single-color sensor which estimates the temperature based on the radiant intensity and requires knowledge of the surface emissivity of an object to determine its temperature. The absorbed energy in each microbolometer raises the pixel's temperature in order to be sensed. So, when incident radiation is absorbed by the metasurface in the bottom microbolometer it will be heated and conduct this energy to the sensing layer. Therefore, the bottom microbolometer is designed with metal-insulator-metal (MIM) configuration, which allows selecting the desired resonant wavelength over the long wavelength region (LWIR). In this configuration, the $Si_xGe_yO_{1-x-y}$ semiconducting layer (293 nm) was encapsulated between the Aluminum (Al) ground plane (169 nm) and the metasurface, which is designed with a hexagonal close packed arrays of circular discs pattern, with a thin dielectric layer of SiO_2 (43 nm) electrically isolating it from the ground plane. This is equivalent to a composite material such that the geometry determines the ensemble properties. The metasurface is arranged to be a perfect absorber over a narrow-band by matching a structure with a groundplane to free-space. The disc array is made by patterning Al with a thickness of (73) nm, and varied diameters (d) and periodicities (p) of 1.11 µm and 2.38 µm; 1.64 µm and 2.64 µm; and 1.94 µm and 2.94 µm, respectively. In this configuration, the metasurface geometry control the absorbed wavelength by changing the diameter, periodicity, and height of the discs. We have used Al as a ground plane in order to achieve high reflectivity out of band. The incident infrared radiation is partially transmitted through the top partially absorbing Fabry-Pérot microbolometer pixel. The metasurface in the bottom microbolometer is reflective out of band and serves as the bottom surface of a Fabry-Pérot cavity. Over this region the top microbolometer acts the same way it would in a traditional

microbolometer and with appropriate design, the resonant cavity maximizes the IR absorption in the microbolometer over this range. The resonant Fabry-Pérot cavity can be created between the incoming and reflected waves if the cavity depth is tuned accordingly: $d_n=[(2n\text{-}1)\text{-}(\varphi_1\text{-}\varphi_2)]\ \lambda/4$, where d_n is the air gap depth, n is an integer, and φ_1, and φ_2 are the phase differences between the incoming and reflected light. An important portion of this is to adjust the impedance matching of the entire structure over the longer band while preserving absorptance in the top microbolometer in the shorter wavelength band. This effort is facilitated by the ability to control the absorption in the top surface by tuning the Si-Ge-O properties.

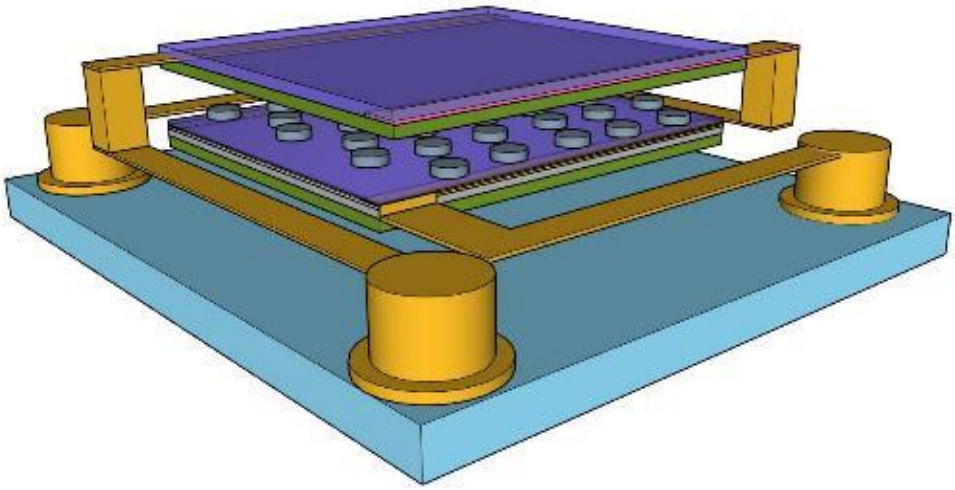

Figure 3.4: A 3-D view schematic of the two stack microbolometer on a single pixel area of 40×40 μm^2.

A total of 9 masks were used to fabricate the dual band microbolometer on a 3" oxidized silicon wafer. Figure 3.5 shows the set of masks that were used to fabricate the device. For the bottom microbolometer: mask 1 is the used for the purpose of patterning the electrical contacts and bonding pads, mask 2 is used to pattern the holes for the microbolometer anchors through the Polyimide sacrificial layer, mask 3 is used for the purpose of building the holding structure of the microbolometer, mask 4 is the

used for the pixel layer patterning, mask 5 is implemented to pattern the electrical layer contacts, and mask 6 was made for the metasurface layer patterning. The top microbolometer starts with mask 7, which is used for patterning the holes to make the anchors through the polyimide, mask 8 is made to pattern the holding structure, and mask 9 is used for the electrical contact's layer.

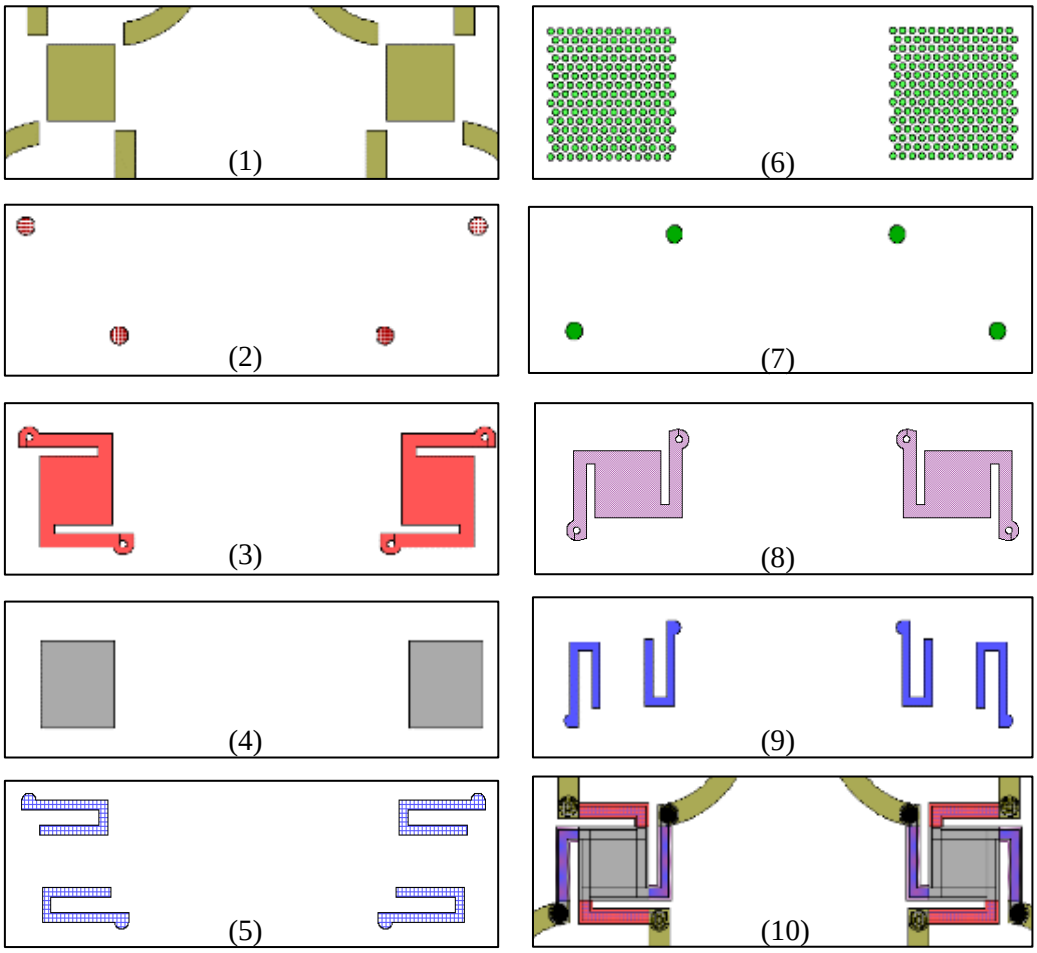

Figure 3.5: Layout of 9 masks used to fabricate the two-microbolometer stack numbered in sequence from (1-9). The completed device with overlaid masks is shown in (10).

CHAPTER 4: MICROBOLOMETER FABRICATION

This chapter explains the microfabrication procedure of the single cavity design and the two-microbolometer stack design in details. Also, the equipment used in the microfabrication procedure.

4.1 Microfabrication Techniques

1) Photolithography

Photolithography is a method of transferring pattern(s) on a layer of photoresist by selectively exposing it to a radiation source. Photoresist is a photo sensitive material, which undergoes changes in its chemical and physical properties, due to exposure to a radiation source. A patterned hard mask is used to selectively expose the photoresist. Post exposure the photoresist coated substrate is placed in a developer solution, which etches away either the exposed or unexposed area, depending on the chemical nature of photoresist. Photoresist is generally composed of three major components: polymer, photo active compound, and solvent.

Specialized equipment such as a spin-coater is used to form a photoresist layer of uniform thickness. The substrate is placed on a vacuum chuck and the photoresist is dispensed on it. It is then spun at a high speed to produce a uniform thickness photoresist film. The thickness of the photoresist layer is given by the following equation [63]:

$$t = \frac{kp^2}{\sqrt{W}} \tag{19}$$

where k is spinner constant, p is resisted solids content (indication of viscosity)and w is the rotational speed in 1000 RPM. From the equation, it is known that the final

thickness of the photoresist layer does not depend on the initial volume of dispersed photoresist nor on the acceleration rate.

Post spin-coating, the level of solvent in the photoresist is reduced but is still high which may result in different developing rates across the wafer. To further reduce the amount of solvent a soft baking is performed, which makes the photoresist denser and improves its adhesion to the substrate of the underlying layer. If adhesion to the underlying layer is poor, sometimes an adhesion promoting layer is used before the photoresist is coated. In most cases, a hot plate is used to soft bake the wafer.

After soft baking, the substrate with photoresist layer is ready for selective exposure. A specialized tool called ‘mask-aligner’ is used to align the substrate to a photomask shown in Figure 4.1. A photomask is generally a square piece of soda lime glass or quartz glass, containing fine Chromium (Cr) pattern(s). The mask-aligner also houses an ultraviolet (UV) light source, which is directed through the mask and selectively exposes the photoresist as shown in Figure 3.6. A certain amount of energy, also known as the ‘dose’ is required to chemically change the exposed areas of the photoresist and can be controlled by changing the exposure time. Post UV-exposure, the exposed area either degrades (positive photoresist) or polymerizes (negative photoresist) due to UV induced chemical reaction. The substrate with exposed photoresist is developed in a developer solution, after UV exposure. For a positive tone photoresist, the UV exposed area gets dissolved in the developer, and the unexposed area remains. For a negative tone photoresist, the un-exposed area gets dissolved, while the exposed area remains. Post development hard bake is optional, and it is performed after pattern formation at a higher temperature than soft and post exposure baking. The hard bake reflows the photoresist and hardens it, so that it can withstand aggressive

etching conditions. Photoresist is mostly used as an etching mask, but it can be used as a sacrificial layer for lift-off purpose. Once the photoresist layer has served its purpose,

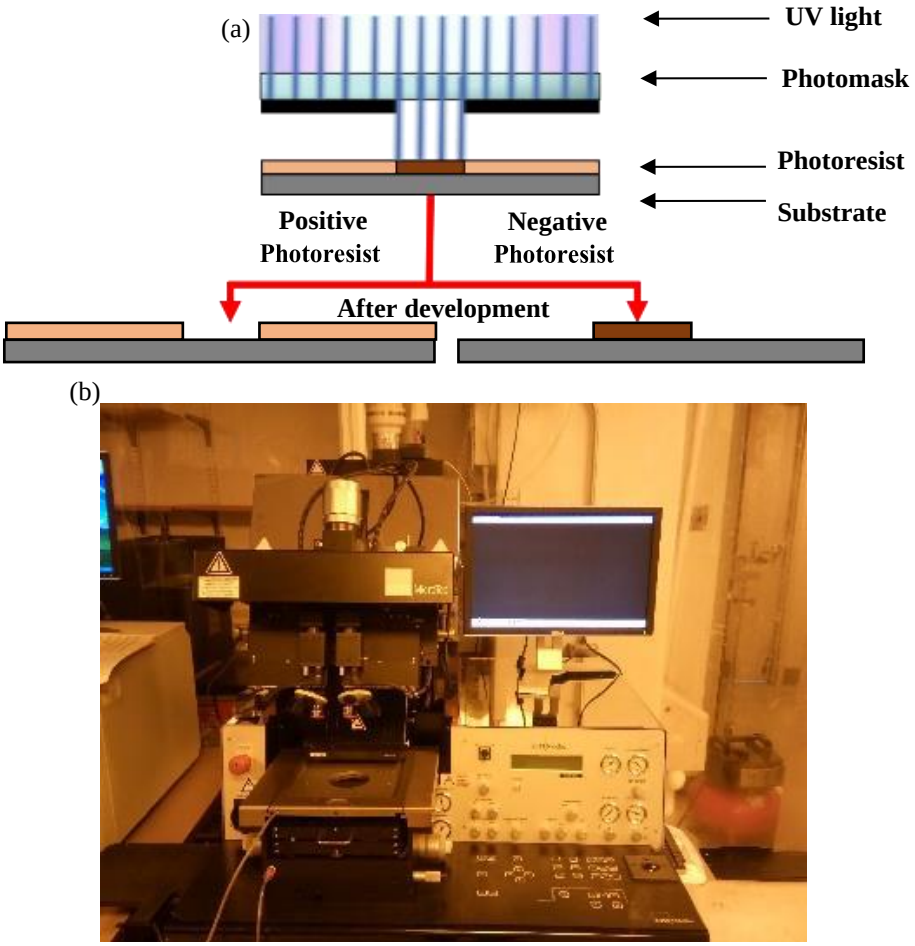

Figure 4.1: Schematic showing the photolithography process of positive and negative photoresist (b) Karl-Suss MA6/MA6 mask aligner used for the UV exposure.

it is stripped away using specialized photoresist stripping chemicals or oxygen plasma ashing.

2) Reactive Ion Etching System

Reactive Ion Etching (RIE) System is one of the dry etching technologies that are used in the microfabrication process shown in Figure 4.2. It has different properties than wet etching. RIE utilizes gases and chemical reactive plasma to etch the material deposited on wafers. Oxygen (O_2) and Methane (CHF_4) gases are used in the process of

ashing and suspending the microbolometer. The plasma technique where radio frequency (RF) discharged or excited ions and radicals are used to etch substrate or thin films in a low-pressure chamber under low pressure (vacuum) in the presence of an electromagnetic field. High-energy ions excited from the plasma attack and react with

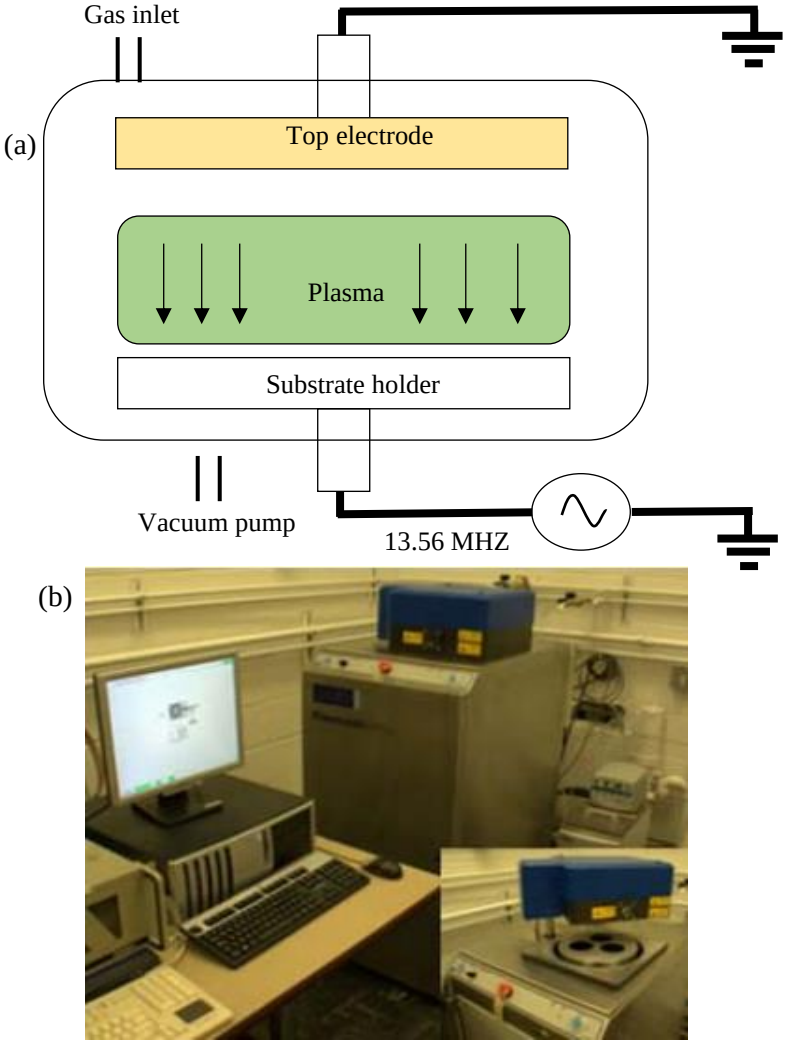

Figure 4.2: (a) Schematic showing the RIE chamber (b) Oxford Plasma lab 80 plus Reactive Ion Etching (RIE) system.

surface of the material. The main privileges of the reactive ion etching RIE over other standard etching is providing directional etching on the material surface and providing a much stronger etching. The reactive ion etching was used in our project to remove the sacrificial layer of Polyimide 1620 and suspend the microbolometer.

3) Oxygen Plasma

Oxygen (O_2) plasma etching is a popular processing technique, which is extensively used for ashing organic polymers, photoresist and can be used for surface treatments. Specialized processing chambers such as a capacitive coupled plasma (CCP) chamber is used for plasma etching, as shown in Figure 4.3. For O_2 plasma etching, large amount of oxygen is flown into the vacuum chamber and plasma is struck using a radio

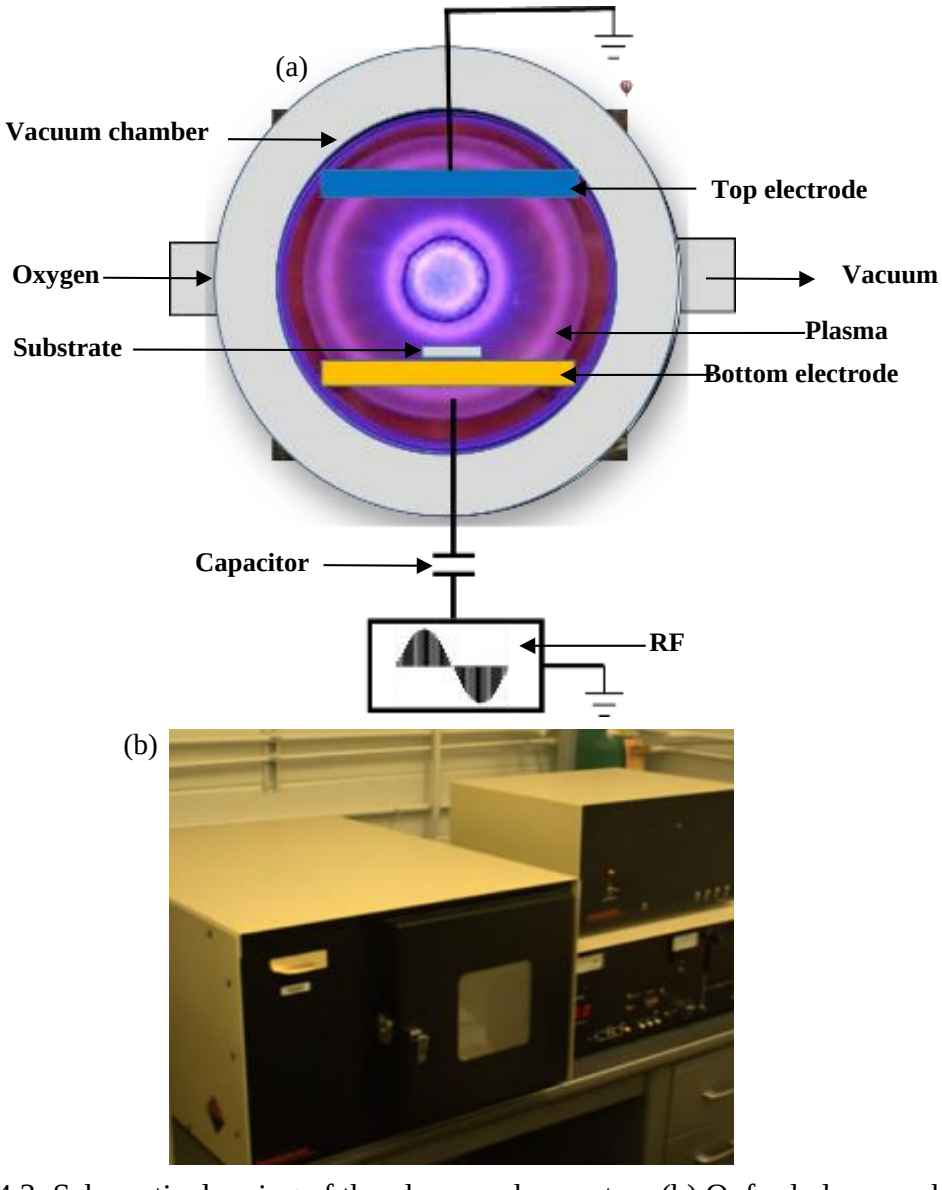

Figure 4.3: Schematic drawing of the plasma asher system (b) Oxford plasma asher machine used in the process of fabrication.

frequency RF power supply, operating at 13.56 MHz. Plasma is generated between the top and the bottom electrode. The top electrode is grounded, whereas, the bottom electrodes is connected to a capacitor, which prevents the DC current from flowing.

To sustain a stable plasma, moderate vacuum conditions are required, which increase the mean free path of the charges and ions. Oxygen plasma consists of electrons, ions, oxygen molecules and oxygen radicals. As electrons and Oxygen molecules collide, Oxygen radicals are generated. This process is defined as dissociation which is expressed as following (20):

$$O_2 + e^- = O + O + e^- \quad (20)$$

The dissociated Oxygen radicals are highly reactive, and reacts with organic polymers generating chemical byproducts. In the vacuum chamber under low pressure conditions, these chemical by products exists in gaseous form and are readily pumped out of the vacuum chamber. As organic material is removed, it exposes, more polymers to the oxygen radicals. The process is the basic principle of photoresist removal using oxygen plasma (21):

$$C_xH_yO_z + O = CO_x + H_2O \quad (21)$$

4) Sputter deposition

Sputter deposition is a physical vapor deposition (PVD) method of depositing uniform thin films with the help of a plasma source. Sputtering is usually referred as atoms ejection from a solid target by bombarding it with accelerated inert gas ions (Argon ion in most cases). A gas discharge is initiated by plasma and the positively charged gas ions are accelerated towards the negatively charged target material. After colliding with the target, gas ions remove some target atoms by momentum transfer. These atoms spread into the chamber and condense as a thin film on the substrate.

Figure 4.4 shows the schematic illustration and the instrument used for DC-sputtering. The target and the substrate face each other in a vacuum chamber with distance of couple of centimeters. The target is connected to the negative side of the DC power supply, acting as the cathode and the substrate and chamber walls are connected to the positive side of the power supply and act as the anode. After reaching a high vacuum level, an argon atmosphere with a pressure of 1-10 mTorr is achieved. By applying a

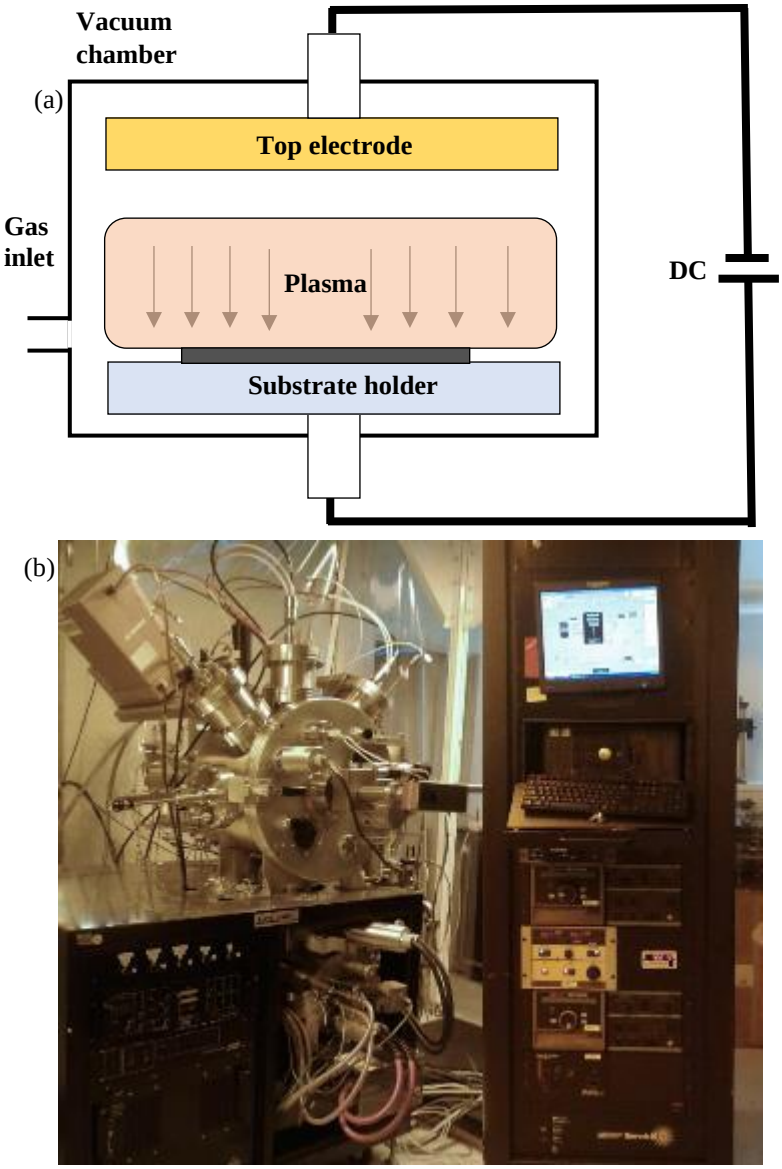

Figure 4.4: (a) Schematic illustration of the DC sputtering system (b) Kurt Lesker AXXIS Multi-Deposition DC sputtering system used in the microfabrication.

DC voltage, the gas discharge is ignited. The created Argon ArP + P-ions are accelerated towards the target and eject atoms target. The free atoms of substrate material are deposited on the substrate as a thin film. DC sputtering is suitable for all conductive target materials. For sputtering insulating materials as well as conducting materials, RF- sputtering is used. In the RF-circuit shown in Figure 4.5 a negative potential is built up at the target due to the different mobility of heavy ions and light electrons in a high frequency electric field (13.56 MHz). Since the positive charges don't need to flow through the target to complete the circuit, sputtering of dielectric

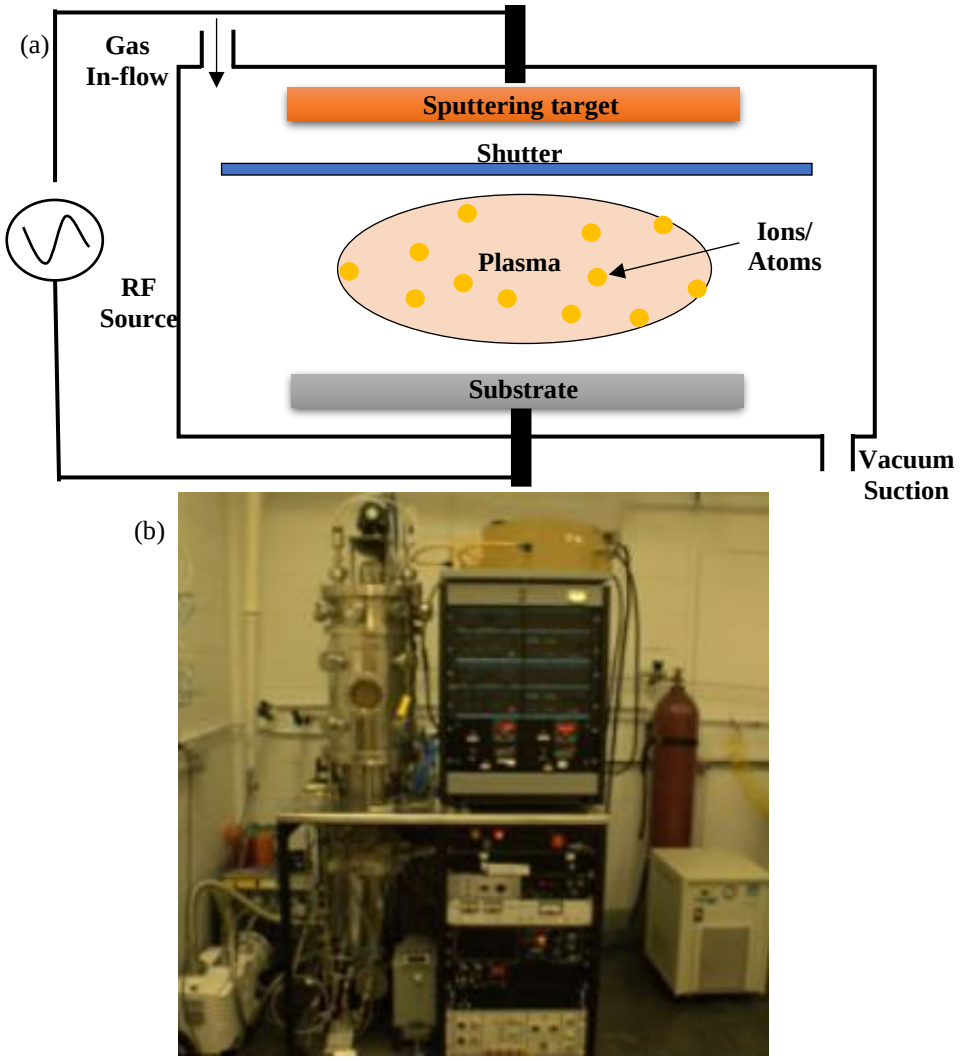

Figure 4.5: Schematic drawing of the RF sputtering system (b) Kurt Lesker Co-Deposition used in the microfabrication process.

materials is also possible by RF sputtering. In addition, there is a higher level of ionization caused by the oscillating movement of the free electrons in the RF field resulting in faster deposition rates [138]. Figure 4.5 (b) shows a photo and a detailed sketch of the RF magnetron sputtering chamber used.

5) Etching and Lift off process

One of the steps in the fabrication process after transferring the photoresist pattern to the substrate is etching the unwanted portion of the layer to create metallic pattern. The etching schematic is shown in Figure 4.6. In the etching process, a liquid (wet etching) or plasma (dry etching) chemical agent removes the uppermost layer of the substrate in the regions that are not covered by photoresist. In semiconductor fabrication, dry etching techniques are generally used since it is more anisotropic, to

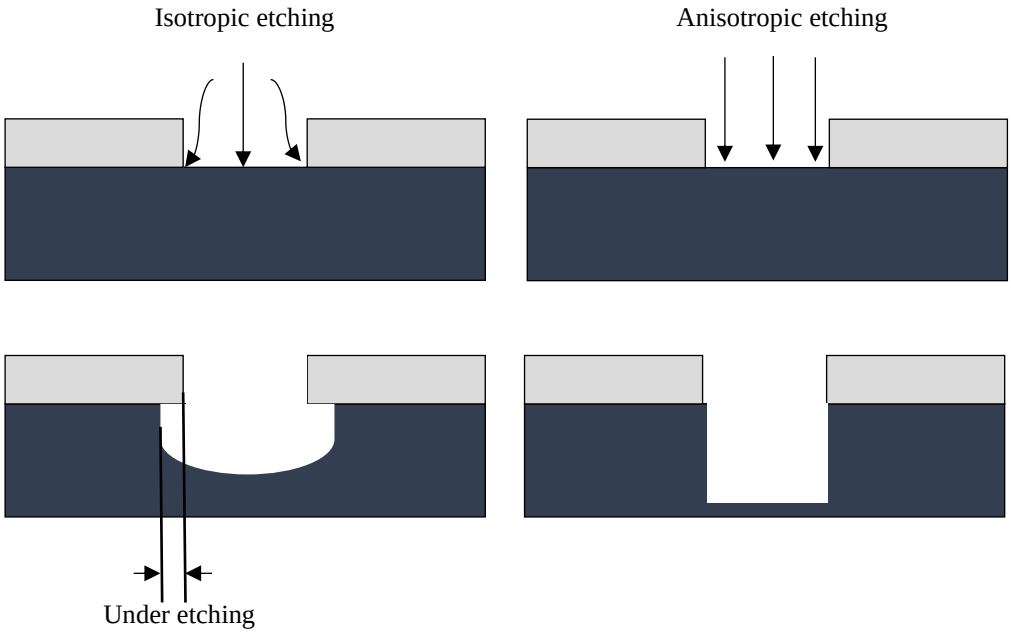

Figure 4.6: shows the schematic difference between anisotropic and isotropic etching.

avoid significant undercutting of the photoresist pattern. This is essential when the width of the features to be defined is similar to or less than the thickness of the material

being etched, i.e., when the aspect ratio close to unity. Wet etch processes are generally isotropic in nature, which is often indispensable for MEMS. Lift-off process is an alternate technique for wet chemical etching or reactive ion etching, it is a common technique to pattern metal or dielectric films. Lift-off process is implemented when suspended structures must be released from the underlying layer used to create structures of a target material on the surface of a substrate using a sacrificial layer, usually a photoresist layer. Figure 4.7 shows standard Lift-off process for pattern generation using negative photoresist. In lift-off processes a sacrificial material, such as photoresist, is first deposited and patterned on the substrate. The material of interest is then deposited on top, and the sacrificial material is subsequently removed, leaving behind only the material deposited directly on the substrate. These processes are useful for patterning materials that cannot be etched without affecting underlying materials on

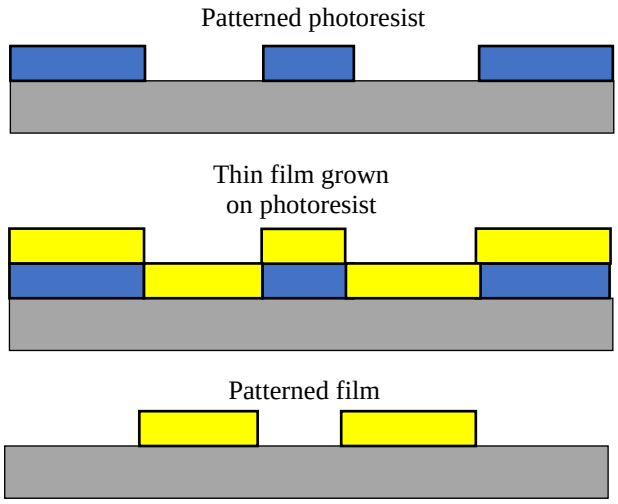

Figure 4.7: Schematic of general process of Lift-off.

the substrate. Lift-off is applied in cases where a direct etching of structural material would have undesirable effects on the layer below. It is a cheap alternative to etching in a research context. Finally, lifting off a material is an option if there is no access to an etching tool with the appropriate gases.

4.2 Microfabrication Procedure

4.2.1 Single Cavity Microbolometer

The fabrication process of the single cavity microbolometer include several steps as illustrated in Figure 4.8. For patterning different layers rather than using etchants, the lift-off technique was employed with conventional photolithography techniques because of it is simplicity. The deposition of different layers was performed by using RF magnetron sputtering from a three-inch sputter target. Prior to the deposition, the

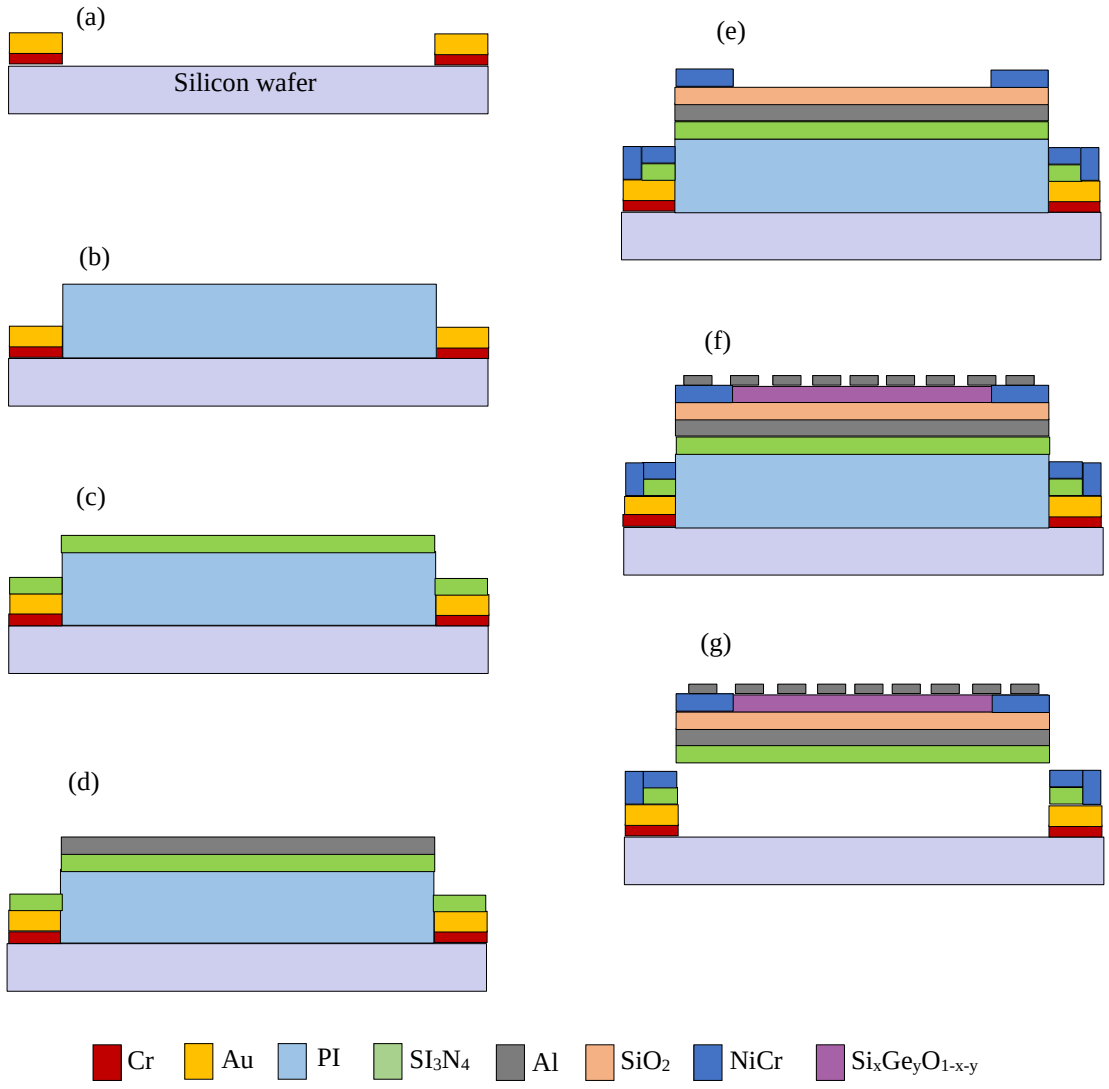

Figure 4.8: Cross sectional view showing the fabrication steps of the microbolometer.

sputtering chamber was evacuated at low pressure of 4 mTorr with a base pressure below 3×10^{-6} Torr. A 3-inch oxidized silicon wafer was used to build the microbolometer. The fabrication is as follow:

1) Pattern the trace lines and bonding pads

A negative photoresist (NR9-1000py) layer was patterned on an oxidized Si wafer at location corresponding to the lead lines and bonding pads. This is followed by sputter-deposition of a thin layers of Cr (73 nm) and Au (170 nm). The wafer was then immersed in acetone with slight ultrasonic agitation to lift-off the unwanted Cr/Au layer forming the lead lines and bonding pads shown in Figure 4.9.

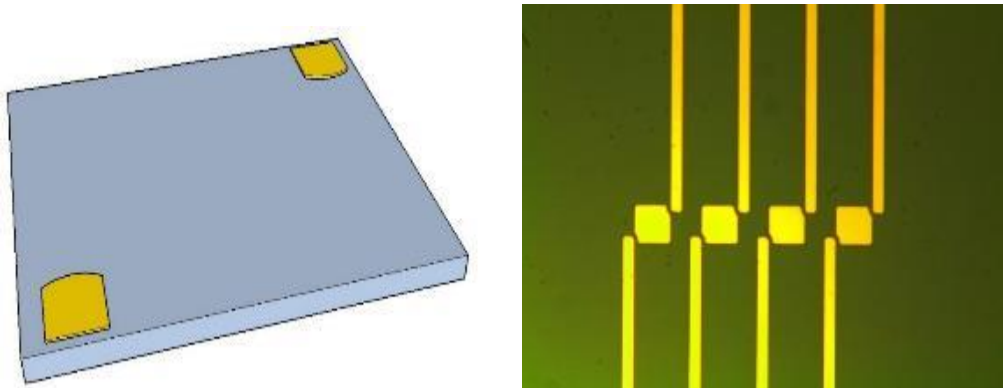

Figure 4.9: Optical images of patterned trace lines and bonding pads for the electrical connection.

2) Pattern the Polyimide sacrificial layer

To create the air cavity for thermally isolating the microbolometer from the substrate, a polyimide sacrificial layer (PI2610) was spin coated, soft baked in oven at 140 ^{o}C for 40 minutes in N_2 environment. The temperature was ramped up to 270 ^{o}C and the polyimide was cured for 2 hours in N_2 environment to obtain a layer with a thickness of 2.1 µm. The temperature was ramped down to 90 ^{o}C before removing the wafer from the oven. A layer of photoresist (3.4 µm Shipley 1827) was spin coated and patterned and the polyimide was then etched at location corresponding to the

microbolometer anchors. Reactive Ion Etch (RIE) system was used to etch the anchors with an O_2 flow of 50 Sccm and CHF_3 flow of 10 Sccm, the RF power used was 150 W and etching time of 12 mins as shown in Figure 4.10.

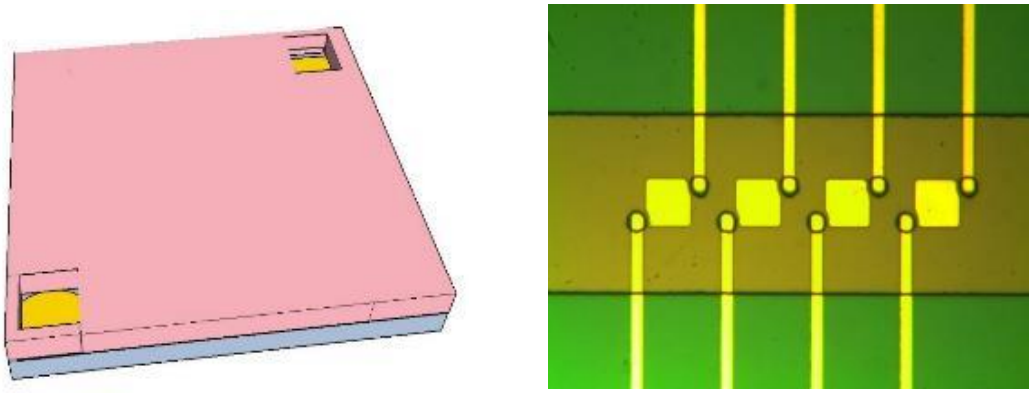

Figure 4.10: Optical images after patterning the polyimide sacrificial layer at locations corresponding to the microbolometer anchors.

3) Pattern the support structure

Prior to depositing Si_3N_4, a photoresist layer (NR9-1000PY) was patterned followed by sputter deposition and patterning using lift-off technique of a layer of Si_3N_4 with a thickness of 291 nm to serve as a support bridge as shown in Figure 4.11.

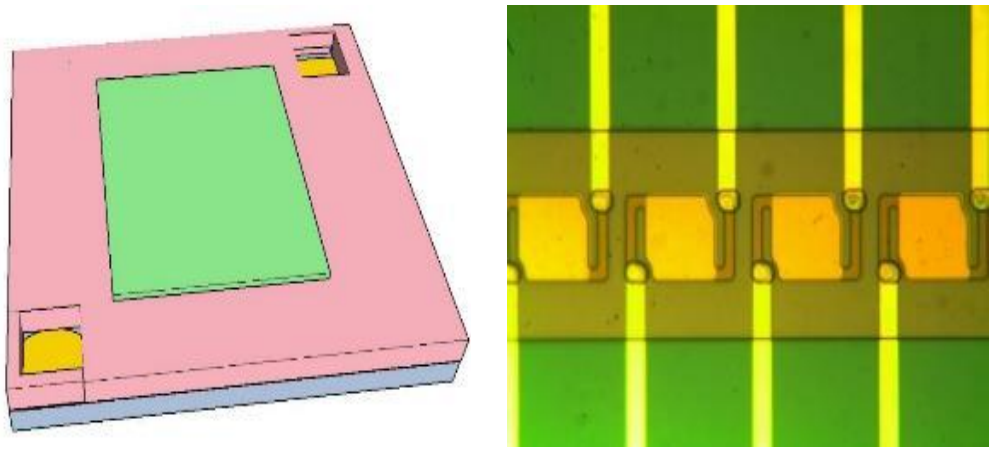

Figure 4.11: Different design for the supporting structure layer after depositing Si_3N_4.

4) Pattern the ground reflector and passivation layer

Negative photoresist NR9-1000PY was spin coated and patterned using the pixel layer mask. This is followed by sputtering and patterning a layer of Al (169 nm) to form the ground plane, and a layer of SiO_2 (43 nm) to isolate the subsequent layer of Si-Ge-O from the ground plane. The two layers were lifted-off by sonication in acetone as shown in Figure 4.12.

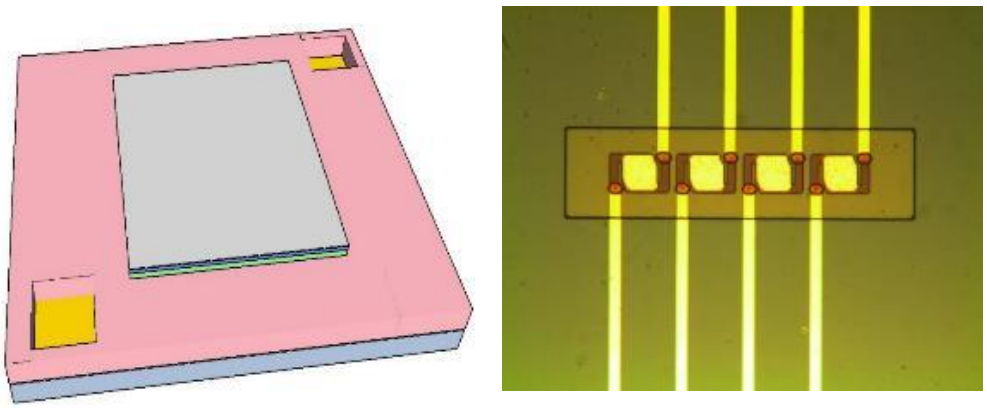

Figure 4.12: Patterned Aluminum back plate and SiO_2 passivation layer.

(5) Pattern the electrode layer

The electrode and electrical contacts were formed by sputtering and patterning a layer of NiCr (80% Ni and 20 % Cr) with a thickness of 83 nm, using liftoff process as shown in Figure 4.13. NiCr was selected due to its low thermal conductivity and

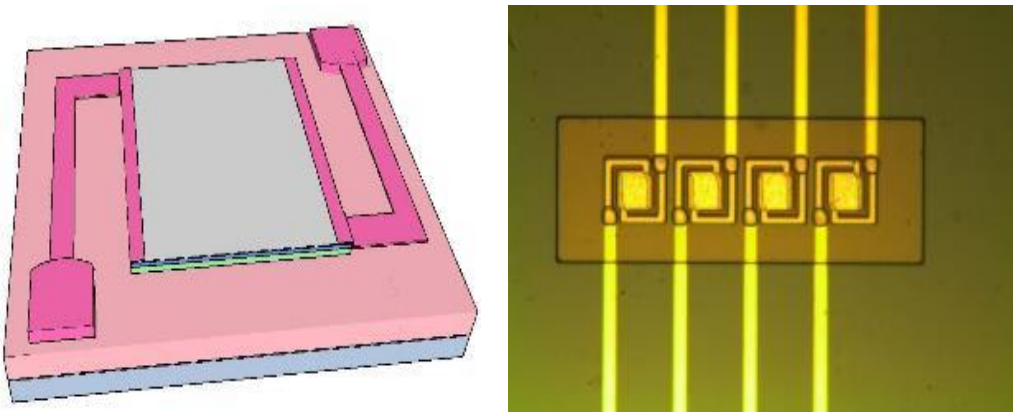

Figure 4.13: Ni-Cr contacts patterning and deposition.

excellent ohmic contact with Si-Ge-O. Then, the wafer was cleaned with methanol and DI water after lift-off by acetone.

(6) Pattern the sensing layer

Silicon Germanium Oxide ($Si_{344}Ge_{0.602}O_{0.054}$) IR sensing layer was sputter deposited with the thickness of 293 nm and patterned using negative photoresist (NR9-1000py) and lift-off process achieve the required pattern as shown in Figure 4.14.

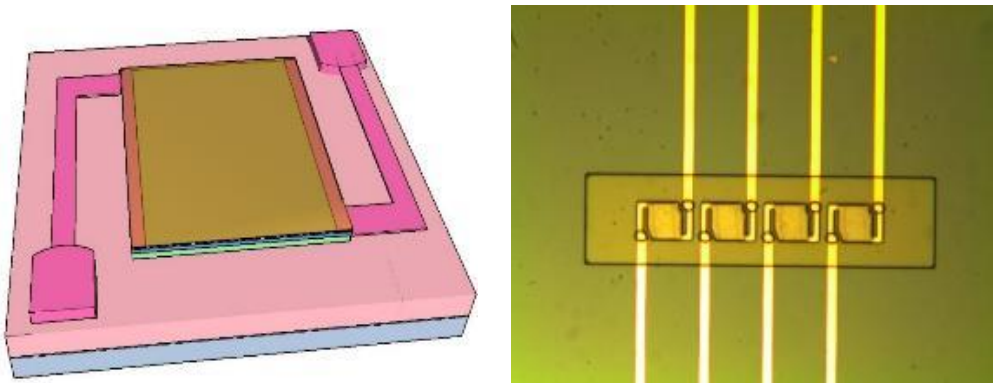

Figure 4.14: The deposition of the $Si_{344}Ge_{0.602}O_{0.054}$ sensing layer with the thickness of 293 nm.

7) Pattern the metasurface layer

A thin layer of Shipley 1805 PR was spin coated and patterned for the Al metasurface layer, the material was then deposited and with circular disk arrays with a varying p (distance between the center of two adjacent disks) and d (diameter of the disks). The thickness was 73 nm with lift-off process, as shown in Figure 4.15.

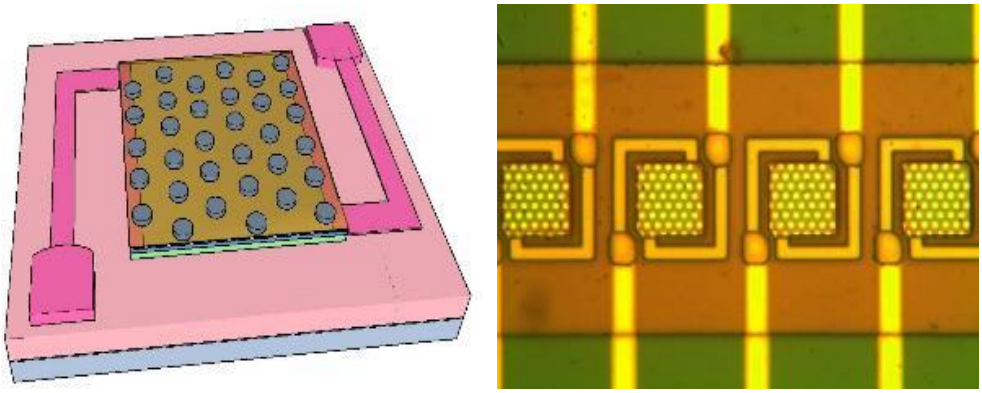

Figure 4.15: Metasurface patterned and deposited on top of the sensing layer.

8) Polyimide removal (Ashing)

In the final step, the fabricated silicon wafer was diced and prepared for the ashing. the polyimide sacrificial layer was ashed away using Branson IPC Oxygen Plasma Asher for 4 hours at 200W of RF power and at 300 mTorr. Ashing was performed for 30 minutes intervals and the substrate was left aside for cooling time of around 10-15 minutes between each cycle. The polyimide was removed isotropically underneath the arms and pixel of the fabricated microbolometer as shown in Figure 4.16. SEM micrographs of the fabricated devices are shown in Figure 4.17.

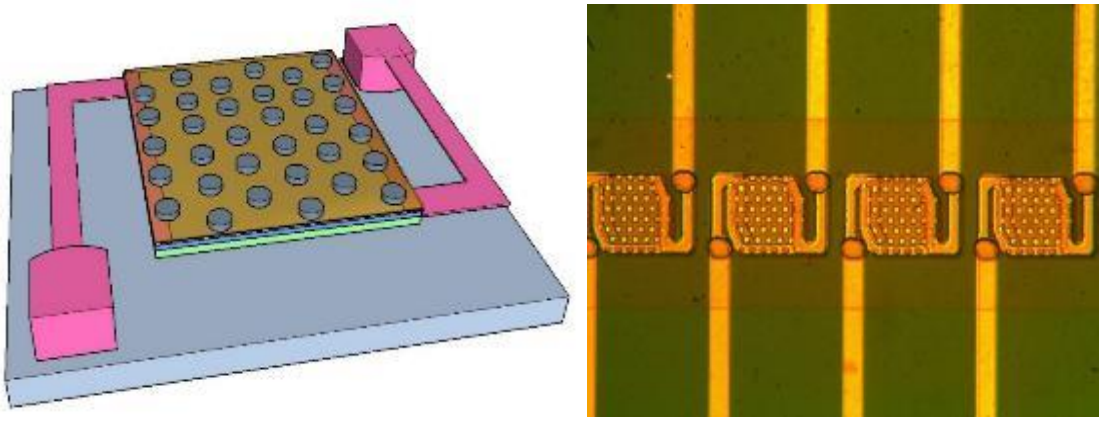

Figure 4.16: Finished microbolometer suspended after ashing the Polyimide.

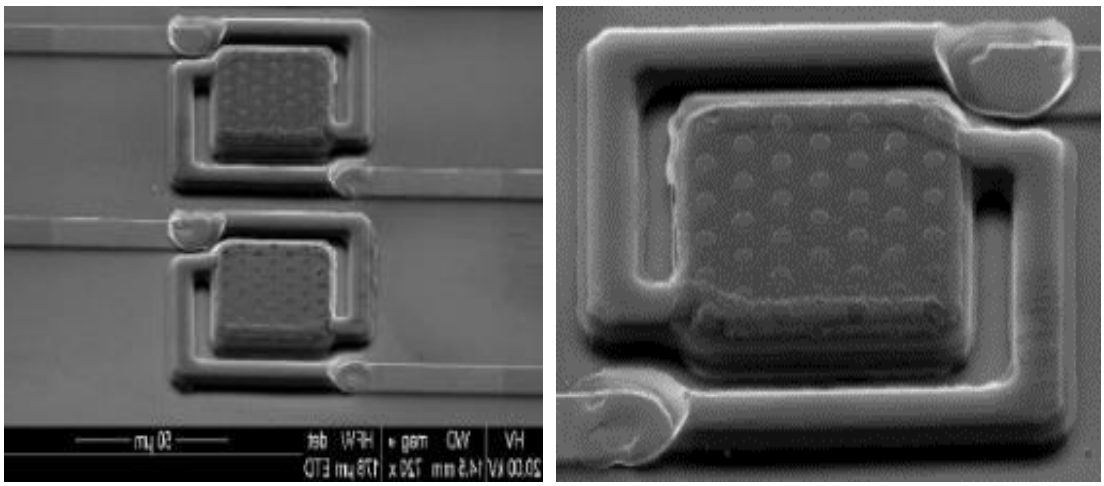

Figure 4.17: SEM images of the fabricated single cavity microbolometer.

4.2.2 Two-Microbolometer Stack Fabrication

The microbolometer was fabricated using surface micromachining processes. The metasurface disks is designed with hexagonal close-packed array of circular metallic discs separated from a metallic ground plane by a thin layer of Si-Ge-O. The supporting bridge are designed with low thermal mass and low thermal conductance to reduce the thermal time constant and maximize the responsivity and detectivity. The fabrication process includes several layers with the cross-section view shown in Figure 4.18. For patterning different layers rather than using etchants, the liftoff technique was used because of it is simplicity. The deposition of different layers was performed by using RF magnetron sputtering from a three-inch sputter target. Prior to the deposition, the

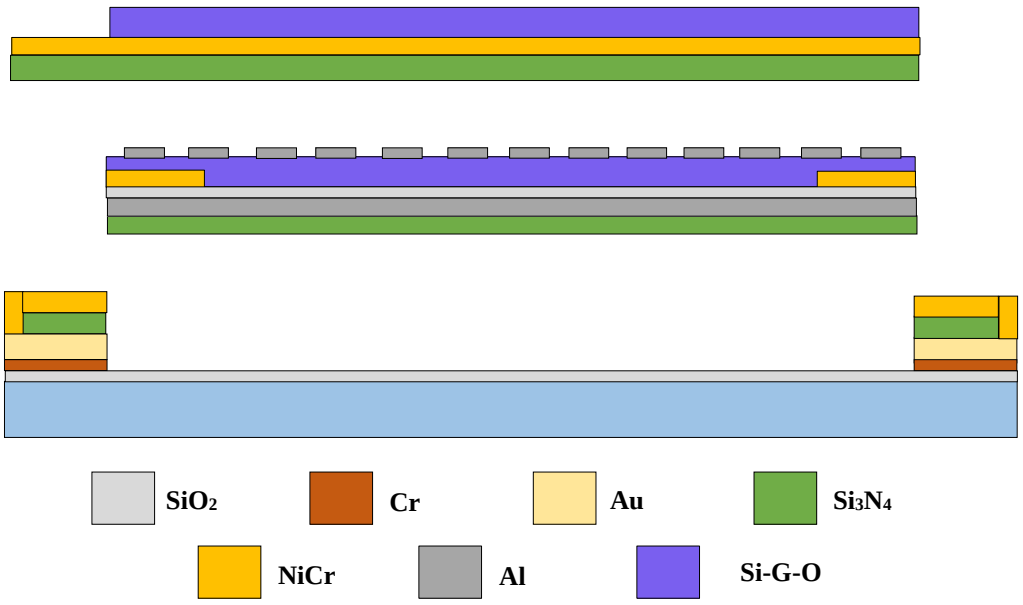

Figure 4.18: Side view showing the fabrication layers used for the two stack microbolometers.

sputtering chamber was set 4 mTorr with a base pressure below 3×10^{-6} Torr. A 3-inch oxidized silicon wafer was used to build the microbolometer. The two-microbolometer stack was fabricated on top of silicon substrate using sputtering, photolithography, lift off, polyimide sacrificial layer and surface micromachining processes. Initially, the

silicon oxide substrate is cleaned with acetone, methanol and DI water and followed by piranha etch for 5 min.

1) Pattern the trace lines and bonding pads

A negative photoresist (NR9-1000py) layer was patterned on an oxidized Si wafer at location corresponding to the lead lines and bonding pads for both microbolometers followed by sputter-deposition of a thin layers of Cr (70 nm) and Au (173 nm). The wafer then immersed in acetone with 3 minutes ultrasonic agitation to lift-off the unwanted Cr/Au layer forming the lead lines and bonding pads as shown in Figure 4.19.

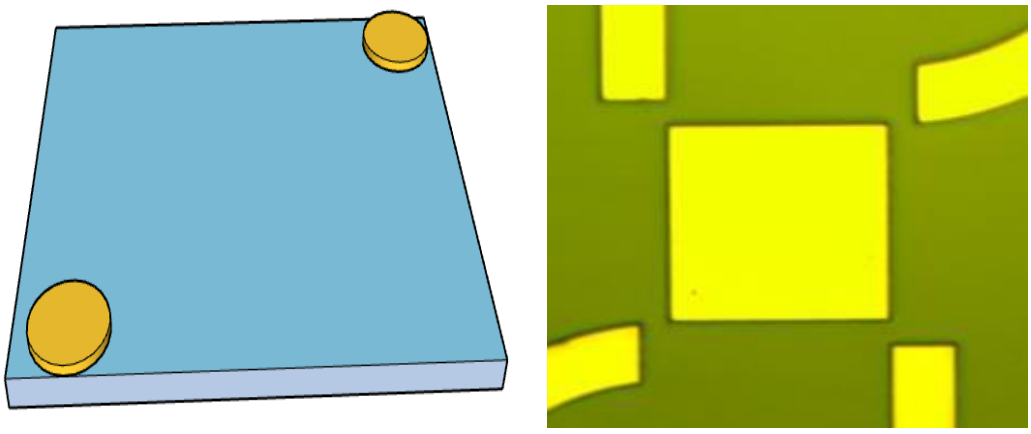

Figure 4.19: Traces and boding pads for the electrical connection.

2) Pattern the first Polyimide sacrificial layer

The air cavity was created using a polyimide sacrificial layer (PI2610), for thermally isolating the microbolometer from the substrate. It was spin coated, soft baked in oven at 140 ^{o}C for 40 minutes in N_2 environment. The temperature was ramped up to 270 ^{o}C and the polyimide was cured for 2 hours in N_2 environment to obtain a layer with a thickness of 2.1 µm. The temperature was ramped down to under 100 ^{o}C before removing the wafer from the oven. A layer of photoresist with a thickness of 3.4 µm AZ4620 was spin coated and patterned, and the polyimide layer was then etched at

locations corresponding to the bottom microbolometer anchors, using Reactive Ion Etch (RIE) system as shown in Figure 4.20.

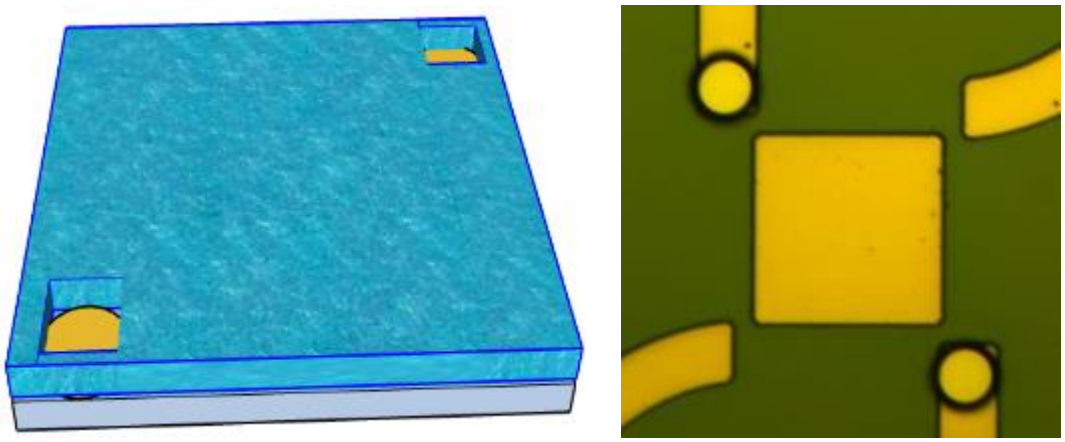

Figure 4.20: Polyimide sacrificial layer coated, and anchors opened for the electrical connection.

3) Pattern the supporting structure

Prior to depositing first Si_3N_4 bridge structure for the bottom microbolometer, a photoresist layer of NR9-1000py was patterned followed by sputter deposition and patterning, using lift-off technique, of a layer of Si_3N_4 with a thickness of 291 nm as shown in Figure 4.21.

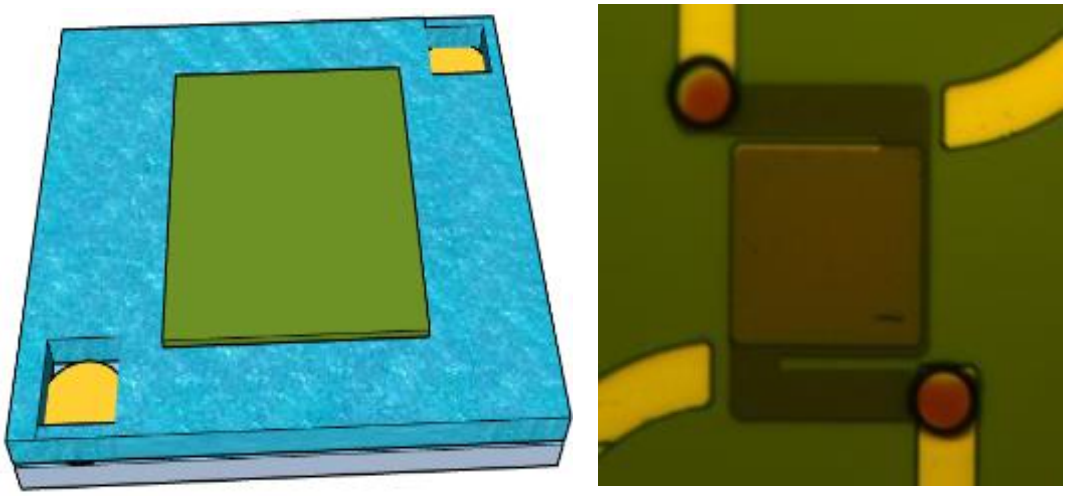

Figure 4.21: patterning and depositing the Si3N4 holding structure of the microbolometer.

4) Pattern the pixel layer and deposit ground plane and passivation layer

Patterning the pixel layer using NR9-1000py photoresist followed by sputtering and a layer of Al (169 nm) to form the ground plane, and a layer of SiO_2 (43 nm) to isolate the subsequent layer of Si-Ge-O from the ground plane. The unwanted Al and SiO_2 were lifted off by immersing the wafer in acetone and the help of sonication for 3 minutes as shown in Figure 4.22.

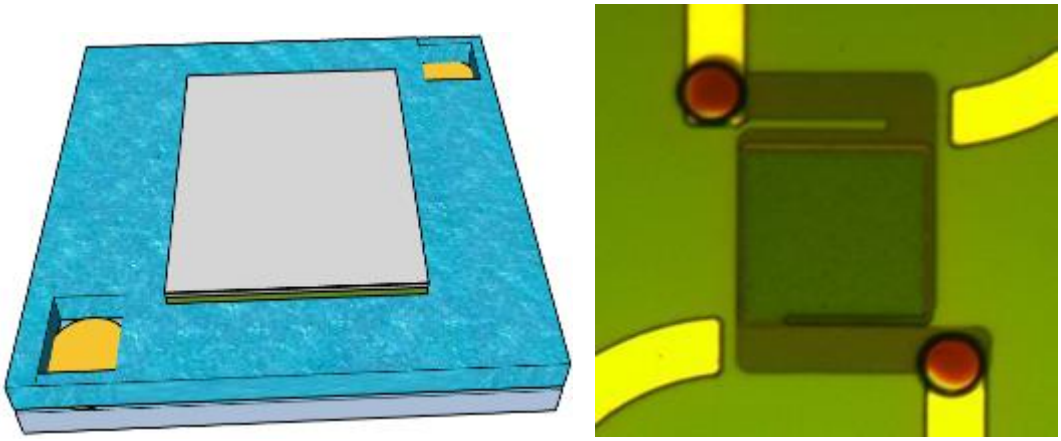

Figure 4.22: Al and SiO_2 layers patterning and deposition.

5) Pattern the electrode layer on the top of the pixel layer

The electrode and electrical contacts were formed by patterning and sputtering a layer of NiCr (80% Ni and 20 % Cr) with a thickness of 83 nm, using liftoff process, the wafer was cleaned by methanol and DI water after lift-off by acetone as shown in Figure 4.23.

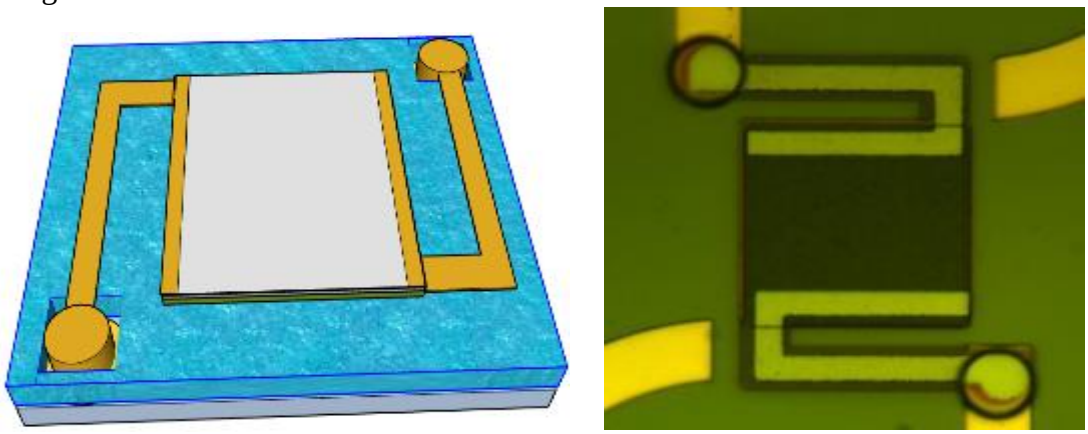

Figure 4.23: Electrode layer of NiCr pattering and deposition.

6) Pattern pixel layer, deposit sensing layer

The pixel layer was patterned using NR9-1000py photoresist to define the region of sensing layer. Then $Si_{0.09}Ge_{0.72}O_{0.19}$ films were co-sputtered from Si and Ge targets simultaneously from two deposition targets in an Ar/O_2 environment at room temperature, low pressure 4 mTorr. The films were then patterned with a thickness of 293 nm, using lift-off process as shown in Figure 4.24.

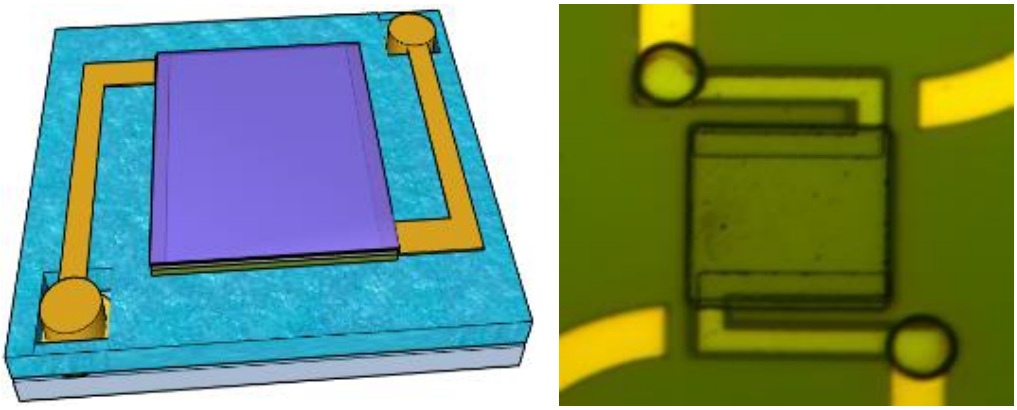

Figure 4.24: Pixel layer patterning and deposition of the sensing layer.

7) Patterning the metasurface layer

A thin photoresist sacrificial layer (SC-1805) was spin coated and patterned to serve as a mold. The Al metasurface layer was then deposited with circular disk arrays. The thickness was 73 nm, the photoresist was lifted-off and the wafer was cleaned by methanol and DI water as shown in Figure 4.25.

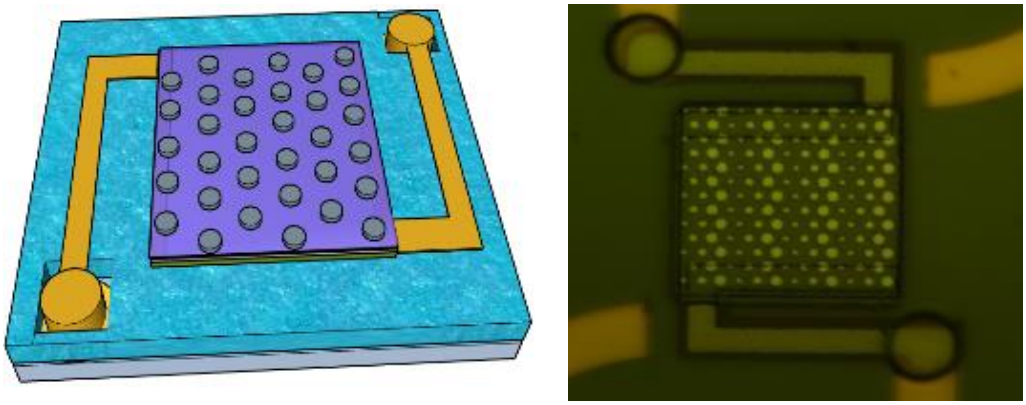

Figure 4.25: Metasurface of different geometry pattering and deposition.

8) Pattern the second polyimide sacrificial layer

The top conventional microbolometer was started by spin coating and curing of the polyimide (PI2610) sacrificial layer of 2 µm thickness to isolate the top microbolometer from the bottom one and provide thermal isolation, and create resonant cavity, polyimide (PI2610) was spin coated, soft baked in oven at 140 ^{o}C for 40 minutes in N_2 environment. The temperature was ramped up to 270 ^{o}C and the polyimide was cured for 2 hours in N_2 environment to obtain a layer with a thickness of 2.1 µm. The temperature was ramped down to under 100 ^{o}C before removing the wafer from the oven. An AZ4620 photoresist with a thickness of 3.4 µm was spin coated to serve as an etch mask for PI2610. The RIE system was used to etch PI2610 layers through the photoresist mask. Then the substrate was cleaned by flushing acetone, methanol, and DI water as shown in Figure 4.26.

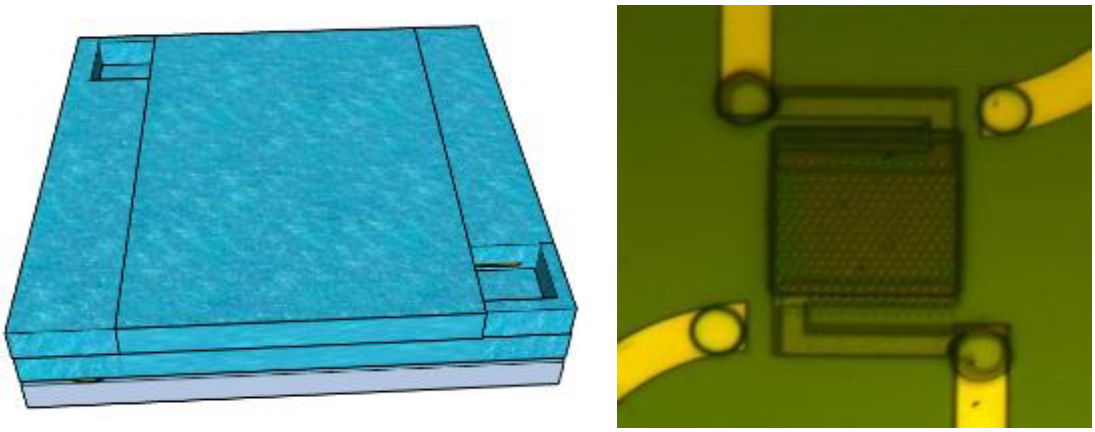

Figure 4.26: Second sacrificial polyimide coated for the top microbolometer suspension.

9) Pattern holding structure layer and deposit Si_3N_4

The bridge structure for the top microbolometer was created by pattering NR9-1000py photoresist and sputter deposition of Si_3N_4 layer with a thickness of 291 nm. Sonication system was used for lift-off with acetone as shown in Figure 4.27.

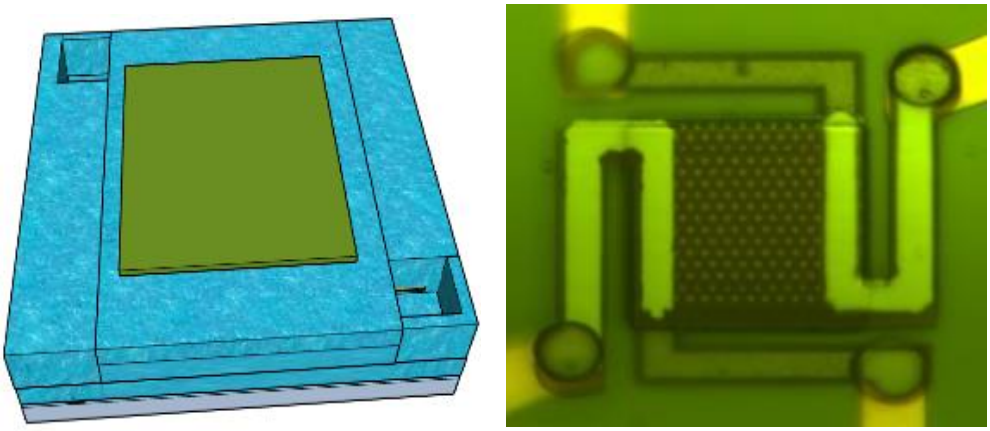

Figure 4.27: Holding structure layer of Si_3N_4 patterned and deposited.

10) Pattern the electrode layer on the top of the pixel layer

NR9-1000PY photoresist was spin coated and patterned with electrode contacts mask. NiCr layer was deposited by sputtering system with a thickness of 83 nm as shown in Figure 4.28. Then, the wafer was cleaned by methanol and DI water after liftoff process by acetone and sonication.

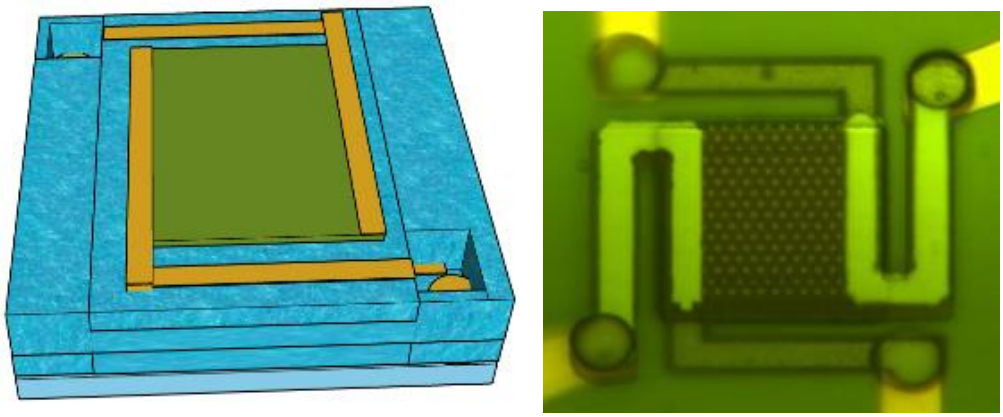

Figure 4.28: Electrode layer made of NiCr for the electrical connection of the top microbolometer.

11) Pattern pixel layer for sensing layer deposition

The second $Si_{0.09}Ge_{0.72}O_{0.19}$ sensing layer was sputter deposited for the top microbolometer with a thickness of 293 nm A thin photoresist sacrificial layer (NR9-1000PY) was spin coated and patterned to serve as mold for depositing $Si_{0.09}Ge_{0.72}O_{0.19}$ sensing layer with a composition candidate that has high TRC and low resistivity. After

that, the photoresist sacrificial layer was lifted-off and the wafer was cleaned by methanol and DI water as shown in Figure 4.29.

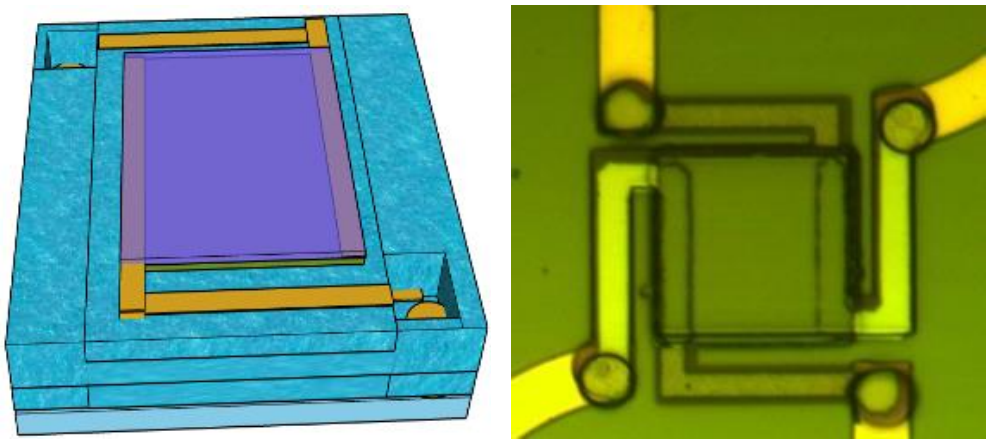

Figure 4.29: $Si_{0.09}Ge_{0.72}O_{0.19}$ sening layer pattened and deposited for the top cavity microbolometer.

12) Polyimide ashing to suspend the microbolometer

In the final step, the two-microbolometer stack was suspended by removing the polyimide sacrificial layer using plasma ashing system under oxygen environment. The polyimide was ashed using Branson IPC Oxygen Plasma Asher for 5hrs at 200W of RF power and 0.3 Torr of O_2. Ashing was performed at 30min intervals with a cooling time of 10-15min between each cycle. The polyimide was removed isotopically underneath the arms and pixel of the fabricated Two-microbolometer stack as shown in Figure 4.30.

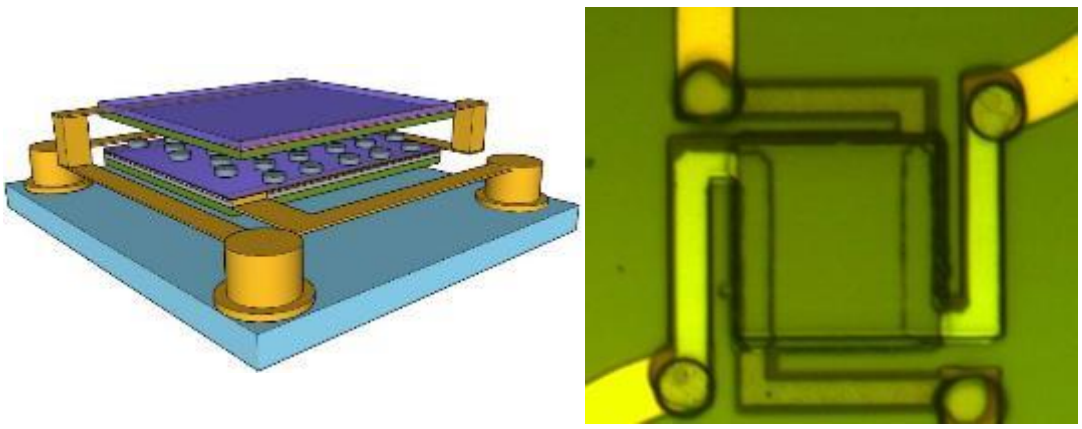

Figure 4.30: Polyimide ached using Oxygen plasma to suspend the two-microbolometer stack.

SEM micrographs of the fabricated Two-microbolometer stack is shown in Figure 4.31.

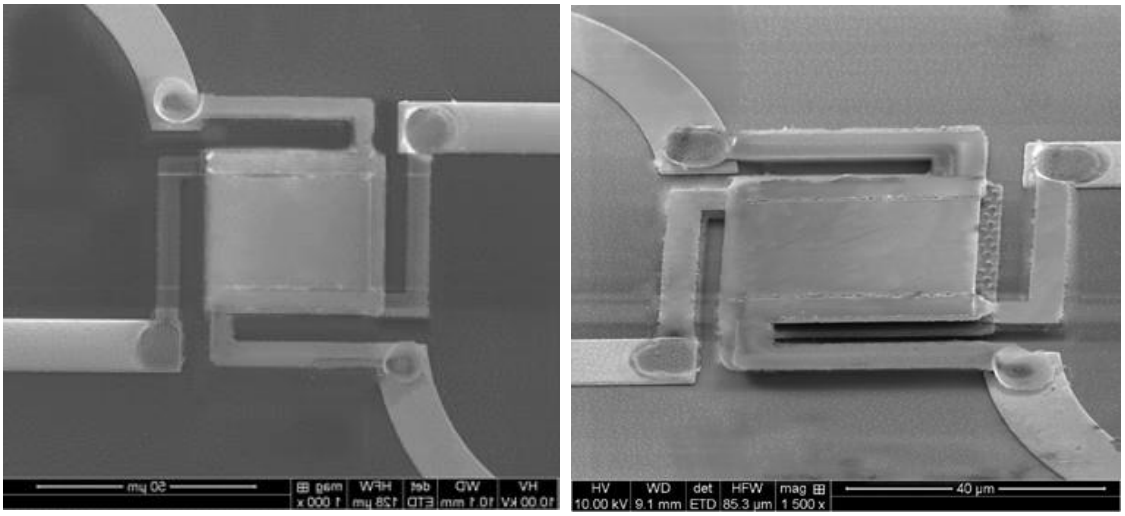

Figure 4.31: SEM micrograph of the two-microbolometer stack suspended on a silicon wafer.

CHAPTER 5: CHARACTERIZATION AND EXPERIMENTAL SETUP

This chapter discusses the experiments performed on the microbolometer in details. This includes the following experiments Temperature Coefficient of Resistance (TCR), resistivity, voltage noise Power Spectral Density (PSD), optical measurements, thermal conductance, and time response.

5.1 Temperature Coefficient of Resistance and Resistivity

The 4-point probe method is typically used to characterize and measure the resistivity and TCR of any semiconductor material as a function of temperature, as shown in Figure 5.1 (a). A spherical protrusion current emanating from the outer probe is assumed. The differential resistance is given by (22):

$$\Delta R = \rho\left(\frac{dx}{A}\right) \tag{22}$$

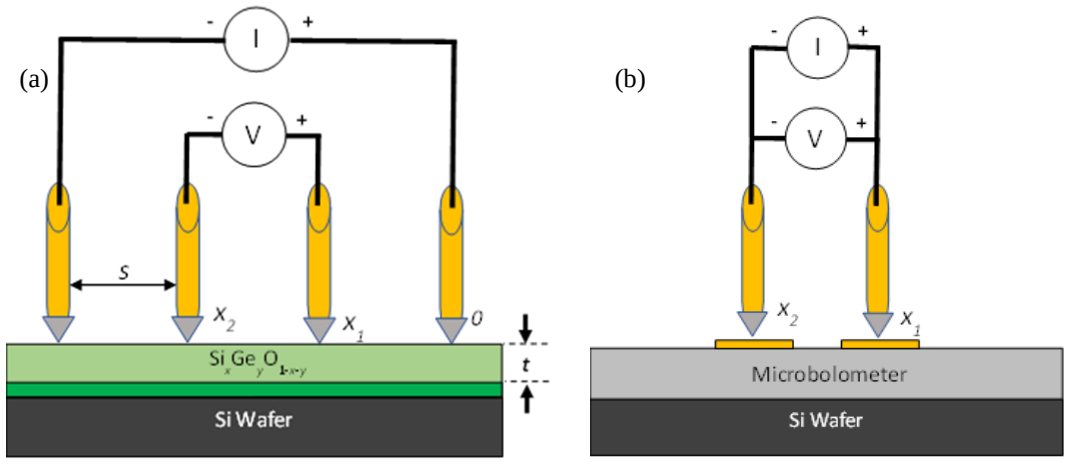

Figure 5.1: (a) Schematic of a 4-point probe for the material and (b) Schematic of a 2-point probe for the detector.

dx is the differential length, and A is the surface area penetrated by the current from one probe. Determining the resistance between the voltage measurement tips, one integrates between x_1 and x_2 (23):

$$R = \int_{x_1}^{x_2} \rho \frac{dx}{2\pi x^2} \tag{23}$$

The relation between the measured resistance and the calculated resistivity of the sensing layer can be expressed by the following equation (24):

$$\rho = \frac{\pi t}{\ln 2}\left(\frac{V}{I}\right) \tag{24}$$

where ρ is the sheet resistivity, t is the film thickness, I is the applied current and V is the measured voltage. We revised the 4-point probe to a 2-point probe to be suitable to measure the TCR and resistance of the fabricated microbolometer, as shown in Figure 5.1 (b). The positive wires of the current source and voltmeter were connected together. Also, the negative wires of the current source and voltmeter were connected in the same manner. The resultant of this connection is a 2-point probe that can be connected to the microbolometer pads to measure the resistance and TCR. The fabricated microbolometer was mounted onto a stage with 2- point probe setup in the Janis VPF-100 cryostat. The resistance-temperature (R-T) and TCR characteristics of the microbolometer were studied with the help of a programmable current source (Keithley Model 220) with a fixed current of 100 nA and a high precision voltmeter (Keithley model 2182 nano-voltmeter). Lakeshore 336 temperature controller was used to vary the temperature from 0°C to 70°C with 2°C intervals. Figure 5.2 shows the TCR setup with the mounted microbolometer. During the testing 150 data points were taken and averaged at each temperature set-point to study the R-T characteristics.

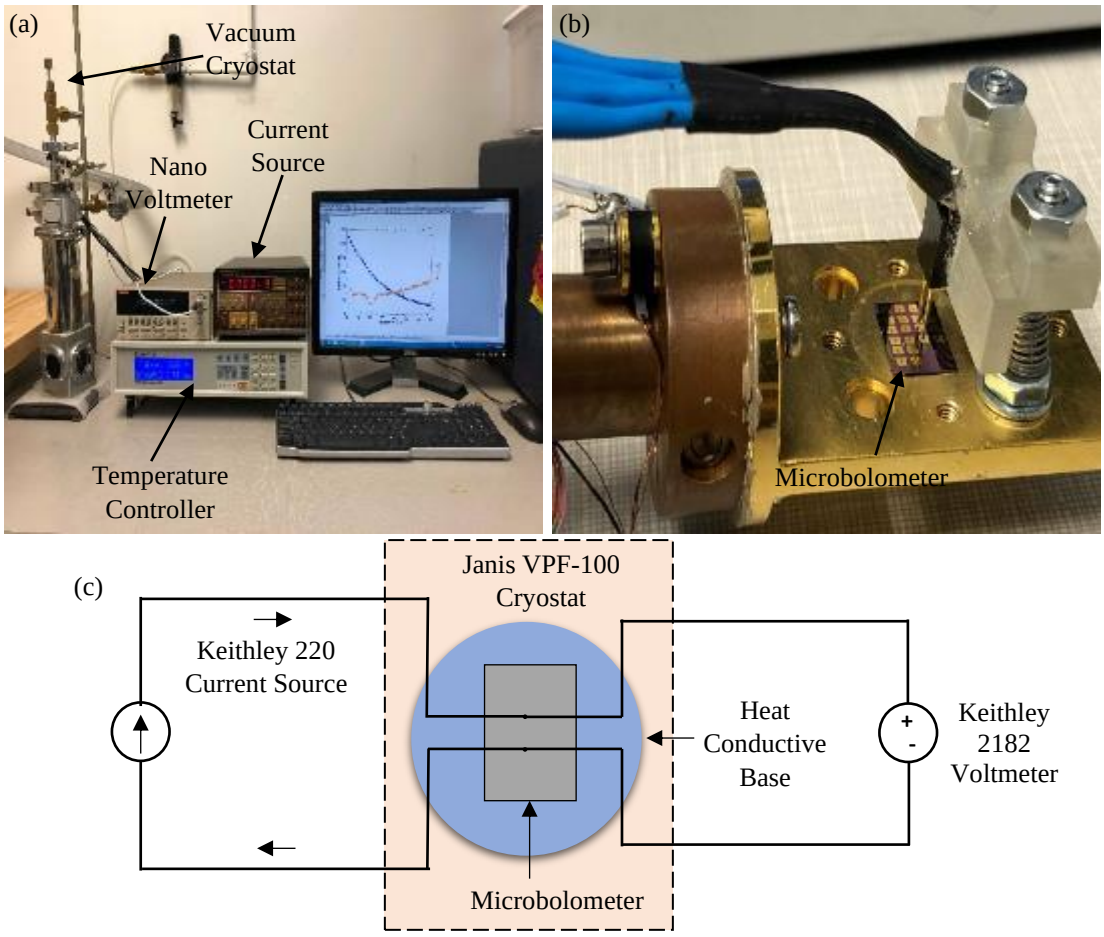

Figure 5.2: (a) TCR and resistivity set up (b) Microbolometer under test (c) Schematic drawing of the 2-point probe.

5.2 Voltage Noise Power Spectral Density (PSD)

The noise measurements were performed in air inside a cryostat (DE 202 cold head), inside an EM shielded box in order to reduce any external noise such as 60 Hz noise. The output voltage was fed to a dynamic signal analyzer (HP 35670A) through a low noise preamplifier (Signal Recovery Model #5113). The microbolometer was connected to a 1 MΩ metal resistor voltage biased using Nickel-Cadmium (Ni-Cd) battery that generates current ranged from 80 nA to 320 nA. The noise voltage power spectral density (PSD) of amorphous $Si_xGe_yO_{1-x-y}$ based microbolometers were

optimized and reduced by annealing the devices in vacuum and in forming gases at 300 °C for 1 to 5 hours of annealing duration. Many devices with two different pixel areas 25×25 μm^2 and 40×40 μm^2 with different compositions of $Si_xGe_yO_{1-x-y}$ were measured before and after annealing at different bias currents. Figure 5.3 shows the schematic diagram of the noise and the testing equipment set up.

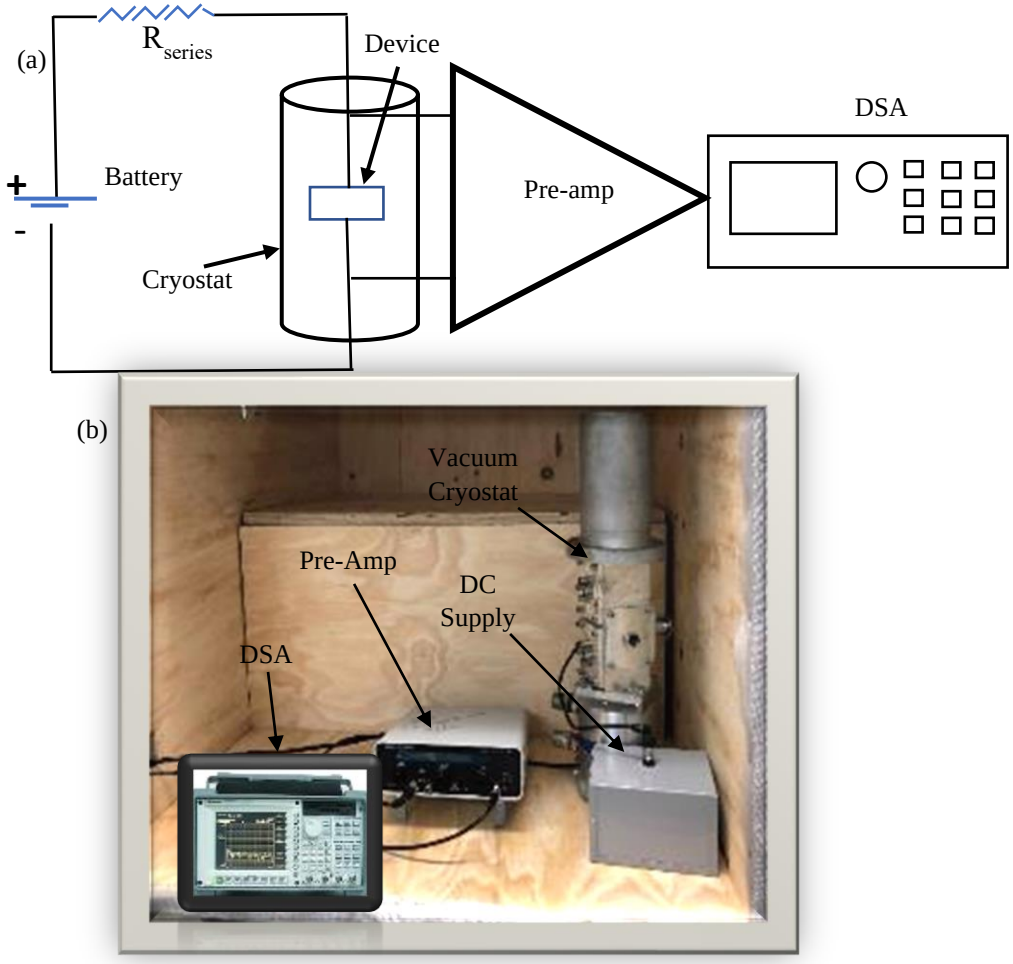

Figure 5.3: (a) voltage noise schematic diagram and (b) shows the testing setup.

5.3 Optical Measurements

The optical response of the microbolometers were measured as a function of wavelength and as a function of chopping frequency using Newport 60090 blackbody light source, a 6575 infrared ceramic element with radiation wavelength between 0.6–16 μm, a 60077 ZnSe condenser, a Newport monochromator, and an optical long

pass filter with transmittance between 1.25–16 µm as shown in Figure 5.4. The measurements were performed in vacuum inside a cryostat through a ZnSe window (2–16 µm), and inside an EM shielded box. The microbolometer was mounted on a vertical stage inside the cryostat allowing the chopped light, which is controlled by a chopper

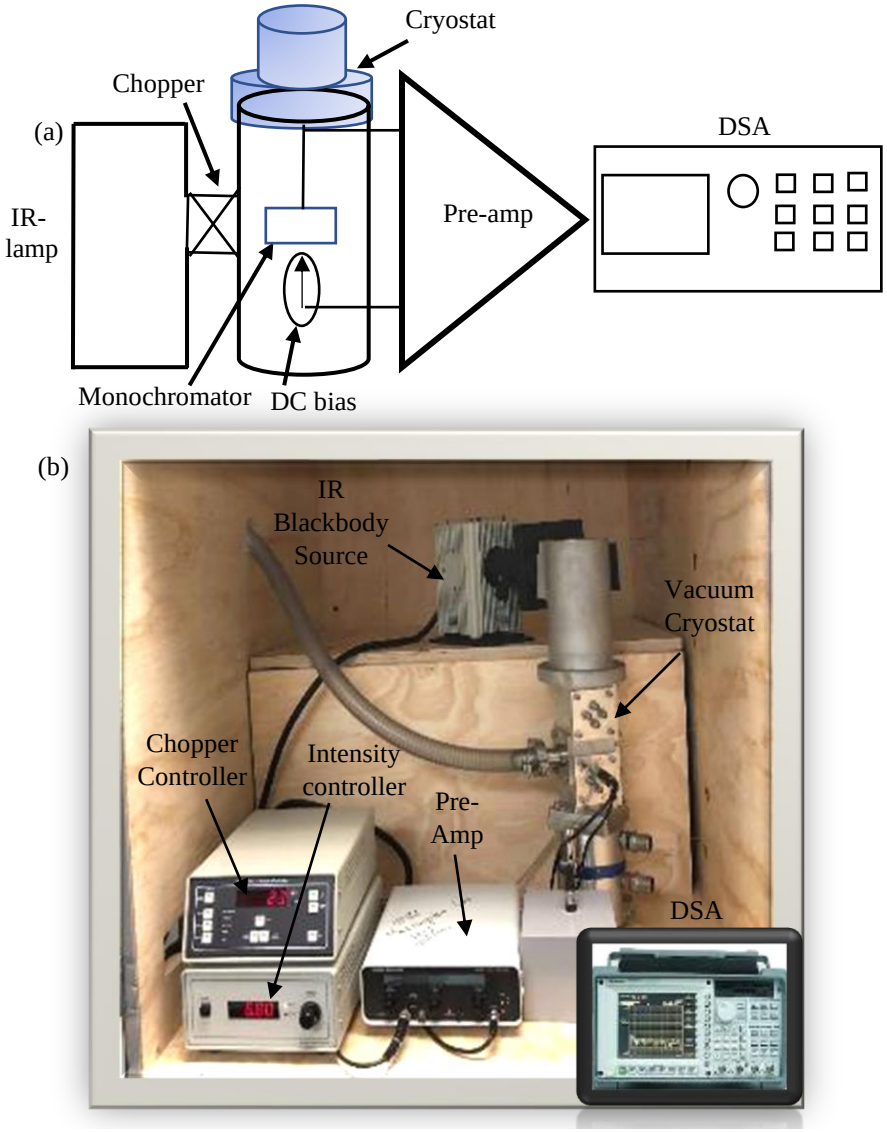

Figure 5.4: Optical testing as function of chopping frequency (a) schematic view (b) testing setup.

frequency controller to fully illuminate the microbolometer surface through the ZnSe window. The devices were connected to a preamplifier (PAR5113) and a Hewlett-

Packard 35670A dynamic signal analyzer, and were DC biased from 80 to 320 nA. The dynamic signal analyzer simultaneously measured the signal amplitude and noise per unit bandwidth for each chopper frequency.

The spectral responsivity and detectivity of the fabricated microbolometers were also measured in vacuum at room temperature, the schematic and setup are shown in Figure 5.5. The signal and noise were recorded for each wavelength between 4–16 µm

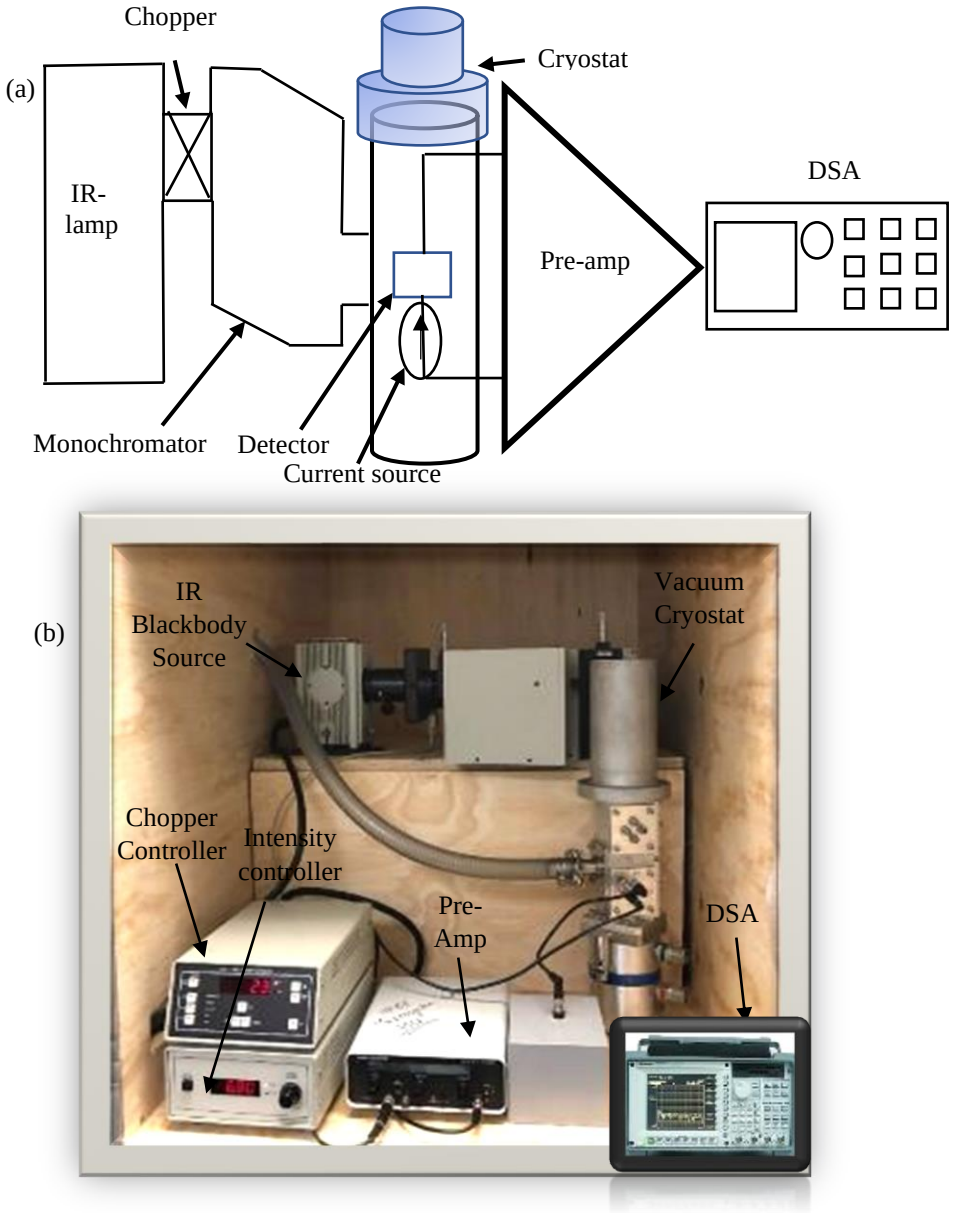

Figure 5.5: (a) Spectral response schematic view and (b) testing setup.

while the light was chopped at 23 Hz. The response was calibrated at each chopping frequency and at each wavelength with a Newport pyroelectric detector (70363) with known responsivity and area. The spectral response of the microbolometer was measured in vacuum as a function of wavelength over the range of 4 to 16 μm.

5.4 Thermal Conductance

Thermal conductance (G_{th}) is an important parameter that characterizes the isolation of the detector. High thermal isolation was achieved using the electrode arms and suspending the microbolometer after etching the polyimide sacrificial layer. Small value of G decreases the rate of heat loss from the microbolometer to the substrate and so increases the responsivity and detectivity of the device. A bias current was forced into the detector with the help of a programmable current source (Keithley Model 220) and the voltages change was recorded. In addition, the resistance change was measured and recorded at different currents from low to high. The following equation was used to calculate G (25):

$$R(T) = R_o + \frac{1}{G}\frac{dR}{dT} I_b^2 R(T) \qquad (25)$$

R_o and R(T) are the resistance value at low and high bias currents, respectively. The resistance versus power dissipated is the equation of a straight line with a slope equal to (26):

$$Slope = \frac{dR}{dT}/G \qquad (26)$$

The dR/dT is calculated from the R-T measurement curve. Also, it could be calculated from the TCR measurement and averaged. The slope was extracted from the measured resistance versus dissipated power at a fixed substrate temperature.

5.5 Thermal Response Time

The measured responsivity as a function of chopping frequency at multiple bias currents is fitted to the following equation with a weight ($W=1/R_v$) (27):

$$Rv(f) = \frac{R_{v\,max}}{(1 + (\frac{f}{fc})^{1/2})^2} \tag{27}$$

The values of the cut off frequency and maximum responsivity were extracted from the fitting data. The thermal response time is calculated by the following equation (28):

$$\tau_{th} = \left(\frac{1}{2\pi fc}\right) = \frac{C}{G} \tag{28}$$

The thermal mass C is the device's thermal response time multiplied by the thermal conductance G_{th}. The cut off frequency fc is the frequency at the highest responsivity value obtained from the device measurement.

CHAPTER 6: RESULTS AND DISCUSSION

This chapter discusses the testing and characterization of the fabricated metasurface uncooled microbolometers including voltage responsivity and detectivity, thermal response time, thermal conductance, resistance versus temperature characteristics and the corresponding TCR versus temperature, and absorptivity.

6.1 Design I: Metasurface Enabled Microbolometer

6.1.1 TCR and I-V Characteristic Curves

Lakeshore 336 temperature controller was used to vary the temperature from 0°C to 70°C with 2°C intervals. Figure 6.1 shows The TCR and the resistance results of the tested microbolometer. The TCR of the measured device at room temperature from 0°C to 70°C with 2°C intervals with $Si_{0.344}Ge_{0.602}O_{0.054}$ sensing layer was -3.07 %/K. 150 data points were taken and averaged at each temperature set-point to study the R-T characteristics. The typical two-wire resistance of the devices were ranged from 200k to 593k.

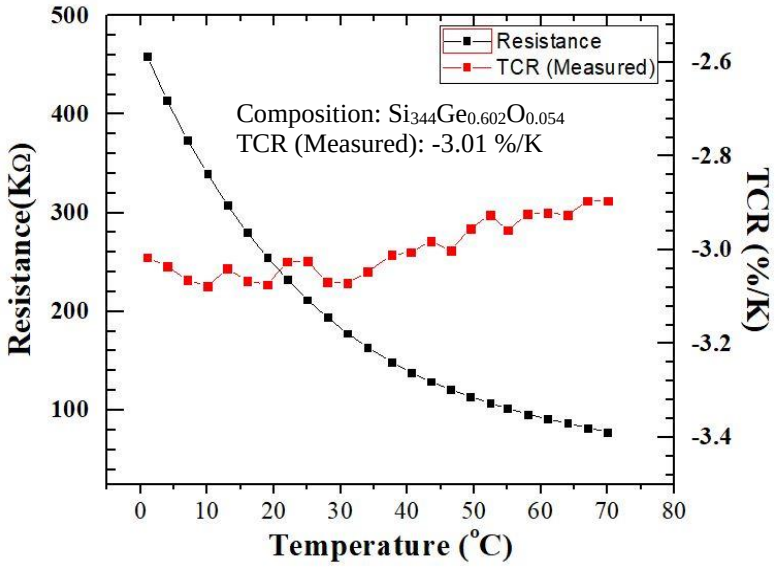

Figure 6.1: Resistance and TCR versus temperature of the tested microbolometer.

6.1.2 Voltage Noise PSD Results

We have measured the voltage noise PSD of the fabricated wafers as a function of frequency at bias current between 80-320 nA before and after annealing. Figure 6.2 shows the noise PSD spectrum before annealing for two devices with different pixel area of 40×40 μm^2 and 25×25 μm^2. The Figure clearly demonstrates that the noise increases as the biasing current increase. The lowest noise voltage PSD with

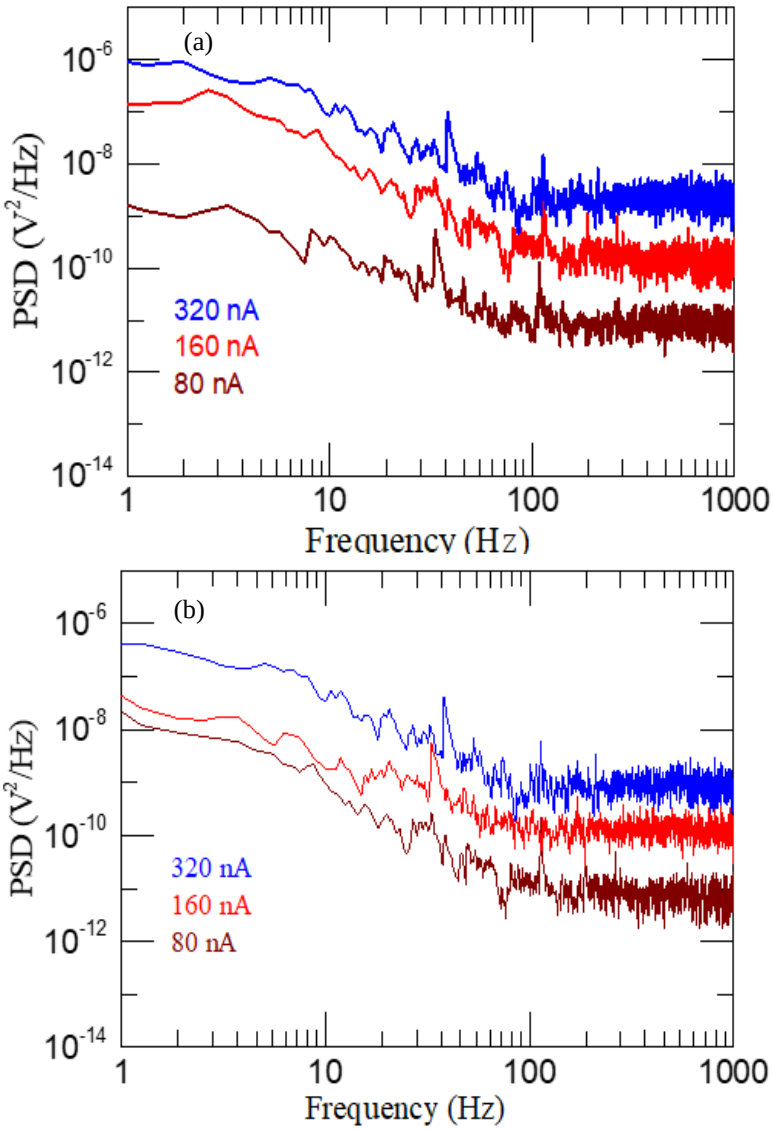

Figure 6.2: Voltage noise PSD before annealing for three different biased current from 80 nA to 320 nA for the device area of (a) 40×40 μm^2 and (b) 25×25 μm^2.

corresponding corner frequency for the devices were 9.01×10^{-12} V^2/Hz at 110 Hz and 9.006×10^{-11} V^2/Hz at 200 Hz for 40×40 μm^2 and 25×25 μm^2, respectively. Figure 6.3 Shows the voltage noise PSD before and after annealing in vacuum at 300 °C for duration from 1 hour to 4 hours using a bias current of 80 nA for microbolometer pixel

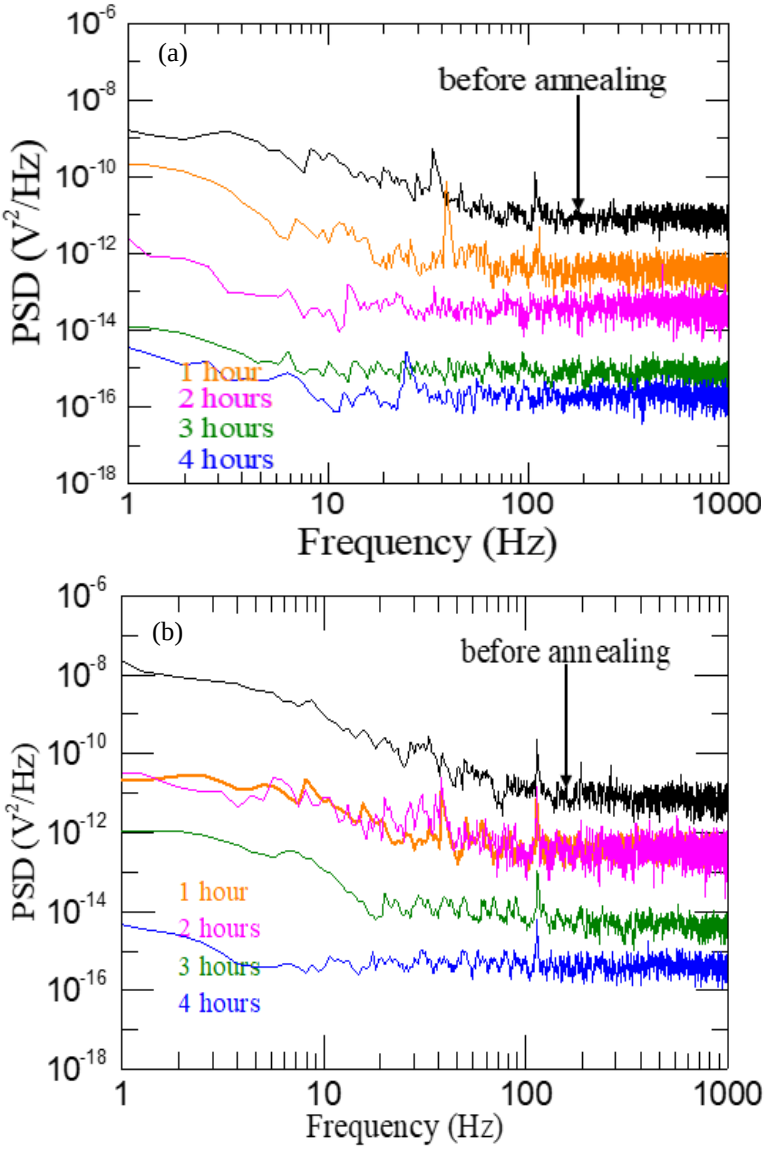

Figure 6.3: Voltage noise PSD after annealing in vacuum for 4 hours at a biased current of 80 for the device area of (a) 40×40 μm^2 and (b) 25×25 μm^2.

size of 40×40 μm^2 and 25×25 μm^2. The voltage noise PSD of the device decreases as the annealing time is increased. After 4 hours of annealing, the voltage noise started to

increase. The lowest measured noise in vacuum annealing for the metasurface integrated microbolometer was 1.06×10^{-16} V^2/Hz. The corner frequency of the device, where Johnson noise meet 1/*f*-noise was lowered to 10 Hz (from 110 Hz) after 4 hours annealing. In addition, the corresponding Hooge's parameters γ, β and K_f for the device were 1.02, 2.01, 2.637×10^{-14}, respectively. The Hooge's parameters and 1/*f*-noise at the corner frequency for the annealing duration are shown in Table 2 and Table 3. We can see from the tables that the average value of γ is close to 1, ranged between 1.02 to 1.19 for the fabricated device. This indicates that the 1/*f*-noise is dominant at low frequencies, and it is higher before annealing. The corresponding 1/*f*-noise coefficient K_f was changed from 5.75×10^{-10} to 2.637×10^{-14} after 4 hours of annealing at 300 °C. The value of K_f started to decrease after annealing time interval. The K_f depends on the quality of the crystal, and on the scattering mechanisms that determine the mobility μ [139]. This decrease in K_f is attributed to the reduction of 1/*f*-noise and the increase of β with increasing the annealing time. The vacuum annealing results show that annealing the devices has reduced the voltage noise PSD significantly on devices that have extremely high 1/*f*-noise before annealing. The lowest measured noise voltage PSD after annealing on the fabricated device was changed from 6.28×10^{-10} V^2/Hz at 10 Hz (before annealing) to 1.06×10^{-16} V^2/Hz at 10 Hz (after annealing). This indicates an improvement factor of 8.5×10^4. As the annealing time of the device increase, the electrical noise level was reduced, and the corner frequency was shifted from 110 Hz to 10 Hz which indicated that Johnson noise can be observed above 10 Hz. Below that, the noise is dominated by 1/*f*-noise. Which indicated that annealing at a specific time reduced the trapping states and defects. The fabricated device seems to have high PSD voltage noise before annealing. This could be due to the composition concentration of

the Si and Ge in the sensing film. Another contributing source of 1/*f*-noise is the bond formation of $Si_xGe_yO_{1-x-y}$ sensing layer in terms of Si-O and Ge-O bond formation [140]. These bonds have resulted in large number of defects in the film and hence

Table 2 : Hooge's parameters of the device with different annealing time intervals for pixel size of 40×40 μm^2.

Annealing at 300 °C	Time (hrs)	PSD at 10 (Hz)	PSD (V^2/Hz) at corner frequency (Hz)	K_f	γ	β
Before annealing	0	6.28×10^{-10}	9.01×10^{-12} (110)	5.75×10^{-10}	1.19	1.78
Vacuum	1	5.76×10^{-12}	5.31×10^{-13} (100)	2.87×10^{-11}	1.13	1.8
	2	3.42×10^{-14}	4.93×10^{-14} (80)	4.93×10^{-13}	1.18	1.85
	3	8.02×10^{-16}	1.02×10^{-15} (20)	2.99×10^{-14}	1.06	1.97
	4	1.06×10^{-16}	1.06×10^{-16} (10)	2.63×10^{-14}	1.02	2.01
Forming gases	1	7.32×10^{-11}	8.13×10^{-13} (90)	1.36×10^{-10}	1.17	1.79
	2	1.12×10^{-11}	1.96×10^{-13} (85)	8.61×10^{-11}	1.14	1.8
	3	2.02×10^{-12}	1.52×10^{-13} (80)	6.13×10^{-12}	1.14	1.82
	4	8.25×10^{-13}	1.31×10^{-14} (70)	6.31×10^{-13}	1.12	2.15

contributed to the presence of 1/*f*-noise. In the same manner, G-O and Ge-Ge bonding leads to dangling bond of Ge [141]. Although we have not observed any sharp peak in the spectrum, which confirmed the presence of dangling bonds, suggesting amorphous nature of all films, and lack of long-range order. Moreover, the presence of deep traps and recombination centers in the Si-Ge bond, and the metal-semiconductor contact between NiCr and $Si_xGe_yO_{1-x-y}$ film might have contributed to the increase in 1/*f*-noise level [142], [143]. The metal semiconductor interface might add to the noise level due to the cleanliness of the contacts and the formation chance of Schottky junction. After 4 hours of annealing in vacuum at low pressure of 1.5×10^{-6} mTorr, we have obtained significant reduction in the noise level, which indicates that the annealing in vacuum has reduced the number of dangling bonds, recombination centers, and impacted the

metal-semiconductor interface. After 4 hours of annealing, the voltage noise PSD started to increase significantly due to the increase of dangling bonds, low field mobility, and the oxide traps [144], [145].

Table 3: Hooge's parameters of the device with different annealing time intervals for pixel size of 25×25 μm^2.

Annealing at 300 °C	Time (hrs)	PSD at 10 (Hz)	PSD (V^2/Hz) at corner frequency (Hz)	K_f	γ	β
Before annealing	0	3.15×10^{-9}	2.24×10^{-11} (100)	8.31×10^{-9}	1.21	1.73
Vacuum	1	7.37×10^{-11}	1.03×10^{-12} (70)	2.01×10^{-10}	1.2	1.79
	2	4.51×10^{-11}	9.21×10^{-14} (70)	6.21×10^{-13}	1.15	1.81
	3	1.95×10^{-15}	3.1×10^{-24} (25)	1.21×10^{-13}	1.09	1.89
	4	8.96×10^{-16}	8.96×10^{-16} (7)	7.12×10^{-14}	1.05	1.96
Forming gases	1	4.98×10^{-11}	1.98×10^{-11} (80)	2.32×10^{-10}	1.2	1.69
	2	6.56×10^{-10}	4.12×10^{-12} (80)	5.13×10^{-12}	1.8	1.71
	3	7.30×10^{-11}	6.0×10^{-13} (75)	1.94×10^{-12}	1.16	1.83
	4	2.01×10^{-13}	9.36×10^{-14} (73)	4.31×10^{-13}	1.13	1.86

We also measured the noise in forming gases system. The forming gas passivation of the samples was done by using MILA mini lamp annealer- Rapid Thermal Annealing (RTA) System. The chamber of the RTA was evacuated by a roughing pump before starting the passivation to avoid the possible oxidation of the samples. A flow mixture of %5 H_2 and %95 N_2 pure forming gas was used for the passivation. The temperature inside the RTA chamber was ramped to 300 °C at a ramp rate of 25 °C/min. The microbolometer was annealed for 4 hours. The PSD noise measurement was performed after each hour. Similar to vacuum measurements, the voltage noise was decreased in the first 4 hours and then starts to increase again. The lowest measured noise when the devices were annealed in forming gases was 1.31×10^{-14} V^2/Hz at the corner frequency of 70 Hz. It can be seen from Figure 6.4 that as the passivation time progressed, the

voltage noise decreased through 4 hours of passivation time, clearly indicating the passivation of dangling bonds in the $Si_xGe_yO_{1-x-y}$ sensing layer, where the hydrogen atoms effectively passivated the defects at the grain boundaries and thus reduced the

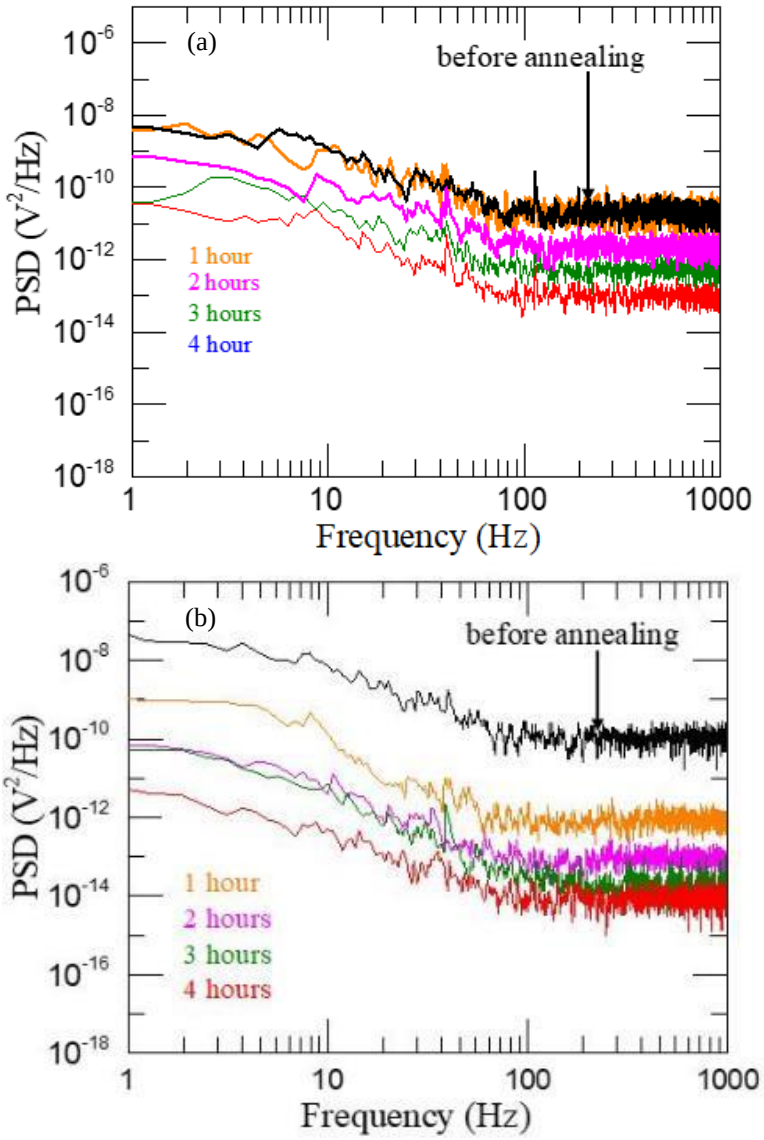

Figure 6.4: Voltage noise PSD of the after annealing in forming gases for 4 hours at a biased current of 80 for the device area of (a) 40×40 μm^2 and (b) 25×25 μm^2.

recombination centers. A comparison between the results demonstrated that annealing in vacuum resulted in much lower noise than in forming gases as shown in Figure 6.5. The corner frequency after 4 hrs of annealing in vacuum is lower than the corner

frequency after annealing in forming gases, which indicates lower 1/*f*-noise and better device performance and characterization. The 1/*f*-noise is believed to originate from the defects and dangling bonds in the sensing layer. The hydrogen passivation using forming gases helps to fix the dangling bonds and defects in which played an important role in reducing the electrical 1/*f*-noise. As the passivation time increased, the 1/*f*-noise decreased leading the hypothesis of reducing the number of dangling bonds with passivation time. The dangling bonds contributed to trap states and scattering centers

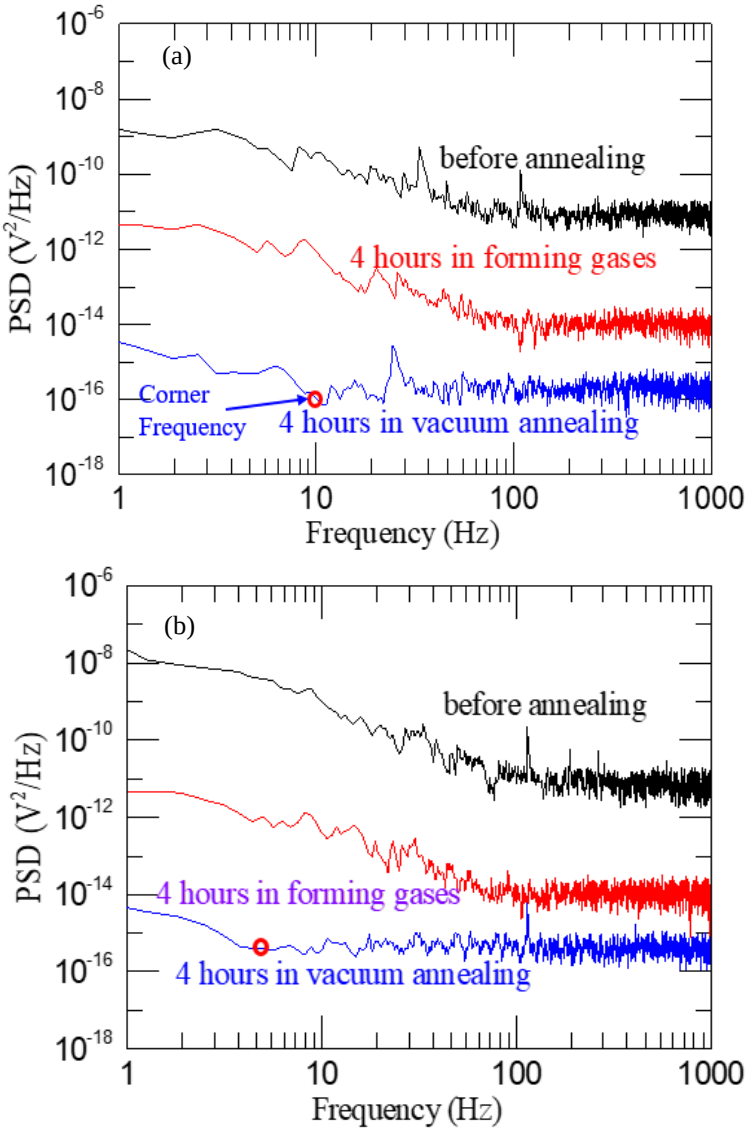

Figure 6.5: Comparison of the Voltage noise PSD at 4 hours annealing in vacuum and in forming gases at a bias current of 80 nA for (a) 40×40 μm^2 and (b) 25×25 μm^2.

for the carriers which lead to the increase of 1/*f*-noise. It was found that the passivation done for excess time (above 4 hours) increased the electrical 1/*f*-noise of the device slightly. After 1, 2, and 3 hrs of passivation time, the noise spectrum does not have any flat portions in the frequency range of 1 Hz to 100 kHz indicating the absence of Johnson noise while the 1/*f*-noise dominates over the Johns on noise. 1/*f*-noise was lowered eventually after 4 hours of annealing in vacuum and forming gases. After that, optical measurement was performed on the samples with low 1/*f*-noise.

6.1.3 Optical Measurements as a Function of Chopper Frequency

The microbolometer was tested as a function of chopping frequency. A typical voltage spectrum in vacuum at bias current 80 nA chopped at 80 Hz is shown in Figure 6.6. The Figure displays a strong voltage response at the chopper frequency. Different geometry of the fabricated metasurface on top of the sensing layer were tested for

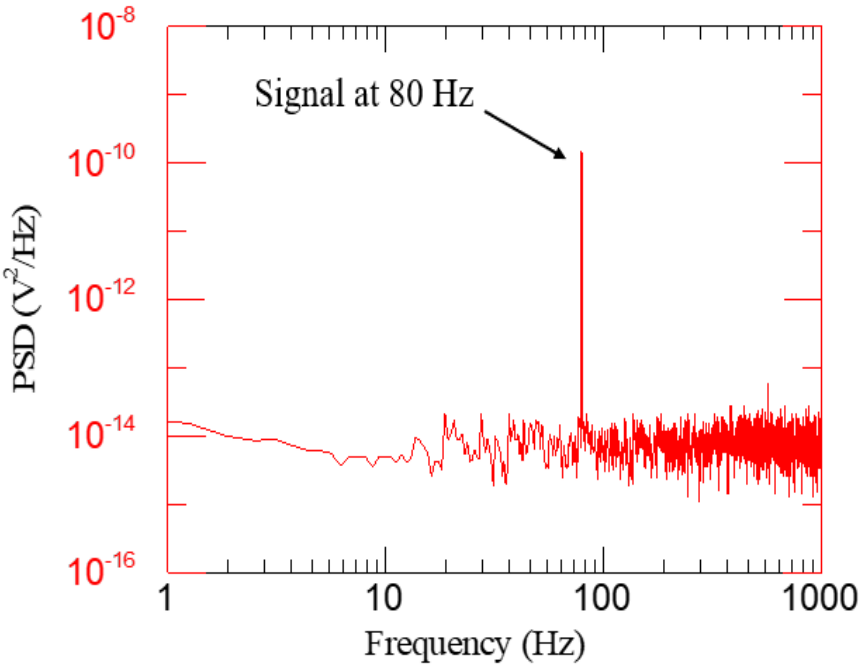

Figure 6.6: Voltage spectrum density (PSD) in vacuum at bias current of 320 nA chopped at 80 Hz.

responsivity and detectivity as a function of chopping frequency at different bias current as shown in Figure 6.7 and Figure 6.8. The highest measured voltage responsivity and detectivity for the 320 nA were 2.17×10^4 (V/W) and 6.94×10^8 (cm-$Hz^{1/2}$/W), respectively. The measured thermal conductance and thermal response time for devices

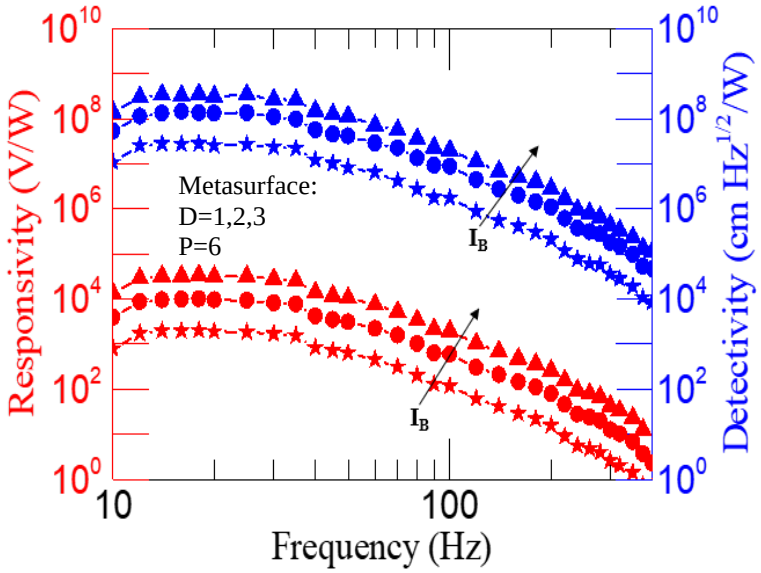

Figure 6.7: Measured R_v and D as a function of chopper frequency at different current biases with different metasurface geometry at fixed wavelength.

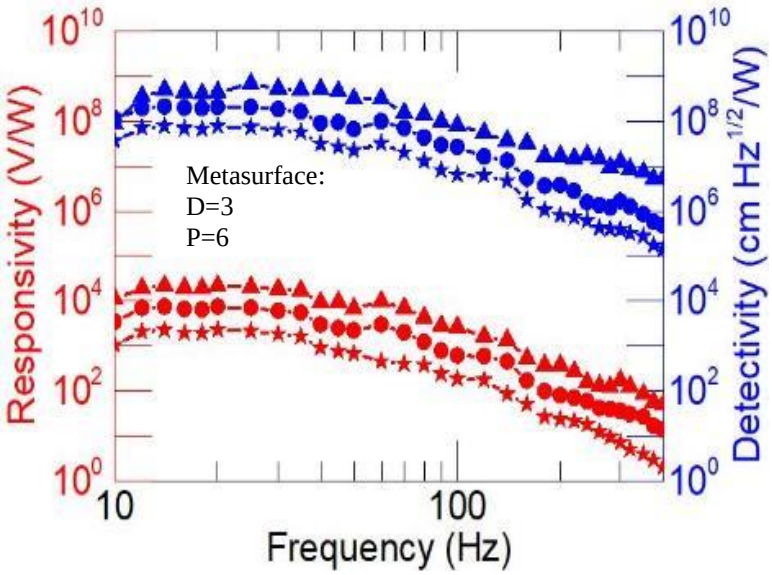

Figure 6.8: Measured R_v and D as a function of chopper frequency at different current biases measured in vacuum at fixed wavelength.

were 5.38×10^{-8} W/K and 3.53 ms, respectively. The absorptivity was calculated to be 25.81%, by fitting the measured data for responsivity, thermal conductance, and thermal response time. The thermal mass was calculated from the measured thermal conductance and thermal response time to be as 2.44×10^{-10} J/K respectively. The values obtained here for responsivity and detectivity are much larger than SiGeO, and amorphous Si microbolometers, and comparable to VO_x devices. A summary of the measured and fitted data for the two devices are presented in Table 4.

Table 4: Microbolometer properties and figure of merits.

Description	Properties
Responsivity R_v (V/W)	2.17×10^{4}
Detectivity D* (cm-$Hz^{1/2}$/W)	6.94×10^{8}
Thermal response time τ_{th} (ms)	3.53
Thermal mass C (J/K)	2.44×10^{-10}
Thermal Conductance G_{th} (W/K)	5.38×10^{-8}
Absorptivity η (%)	25.81

6.1.4 Optical Measurements as a Function of Wavelength

The spectral response of the fabricated microbolometers were analyzed and tested using the monochromator for the wavelength range of 4-16 μm. The use of the metasurface shows selective spectral absorption depending on the diameter and the periodicity arrangement on top of the sensing layer. Figure 6.9 shows the spectral response responsivity and detectivity measurements of the combination of all tested metasurface geometries were plotted together as a function of wavelength. The decrease of the response in the 4 to 8 μm band is most likely due to partial oxidation of the

absorber layer resulted from the exposure to the oxygen during the plasma ashing of the polyimide layer to suspend the device. The highest responsivity and responsivity as a function of wavelength achieved for the broadband metasurface were 3.6×10^4 V/W and 7.81×10^8 cm-Hz$^{1/2}$/ W, respectively. Furthermore, the results shows a shift in the spectral response with respect to the metasurface, which explains the spectral selectivity of the device over the long Wavelength Infrared (LWIR) region. The broadband

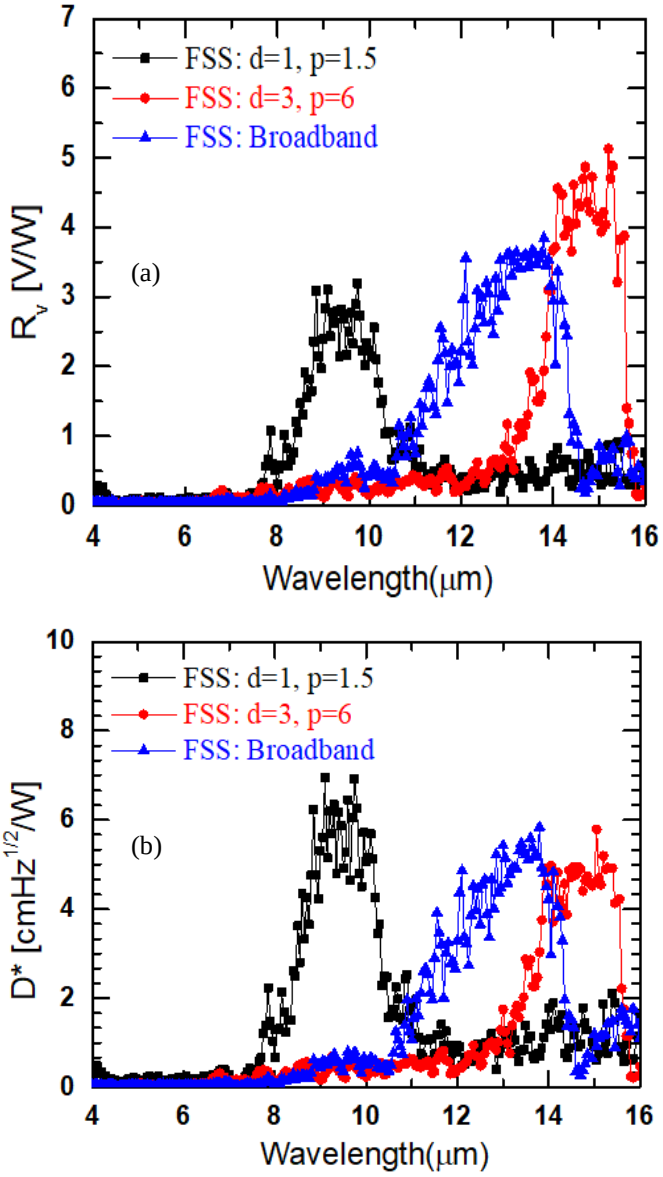

Figure 6.9: The combination of metasurface geometries were plotted over 4- 16 μm wavelength range for (a) responsivity and (b) detectivity.

spectral response was achieved at window between 10.5-15 µm using the combination of metasurface diameters of 1 µm, 2 µm, and 3 µm, and a periodicity of 6 µm.

6.2 Design II: Two-Microbolometer Stack

6.2.1 TCR and I-V Characteristic Curves

Temperature coefficient of resistance of the two-microbolometer stack was studied. Many devices were tested for temperature from 0°C to 70°C with 2°C intervals as shown in Figure 6.10. 150 data points were taken and averaged at each temperature set-

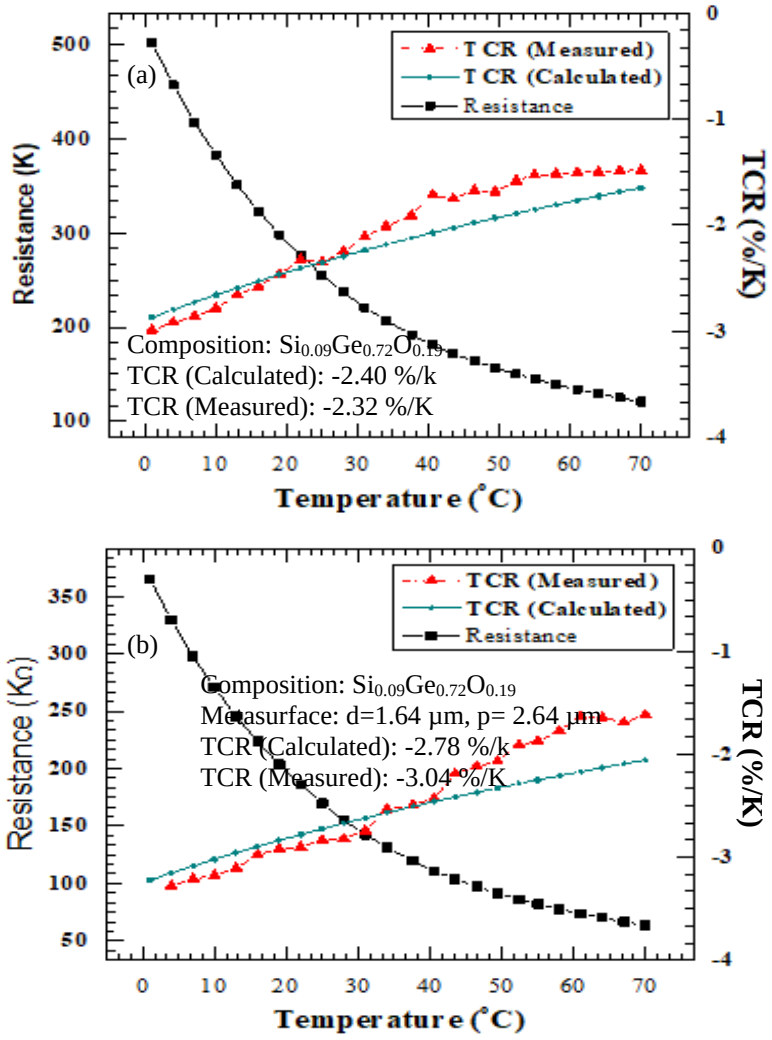

Figure 6.10: TCR versus temperature for (a) bottom microbolometer and (b) top microbolometer.

point to study the R-T characteristics. A candidate composition sensing layer of $Si_{0.09}Ge_{0.72}O_{0.19}$ was tested on the bottom and top microbolometer. The bottom microbolometer showed a TCR of -3.04 %/K, while it was -2.23 %/K for the top microbolometer. The presence of the metasurface on the bottom microbolometer have increased the TCR compared to the top conventional Fabry-Perot based microbolometer. TCR and resistance comparison for the top and bottom microbolometer is shown in Figure 6.11.The devices showed linear *I-V* characteristics up to 1.5 µA with no evidence of joule heating as shown in Figure 6.12.

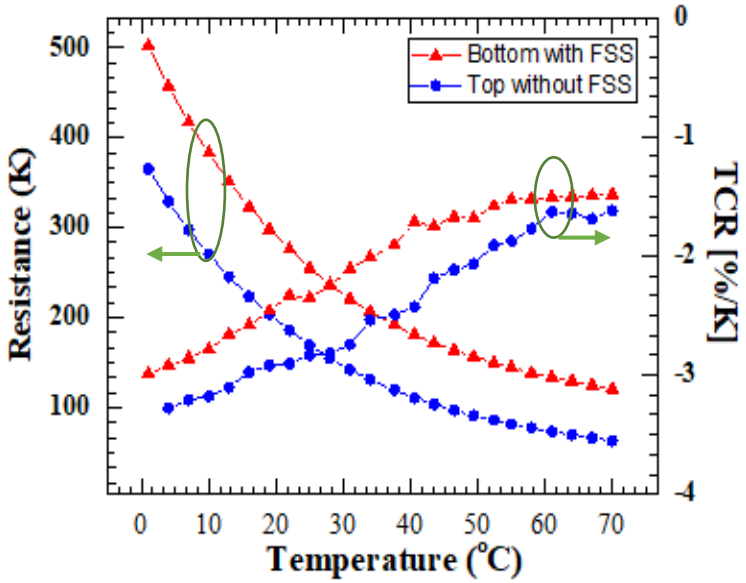

Figure 6.11: TCR and Resistance comparison for the top and bottom

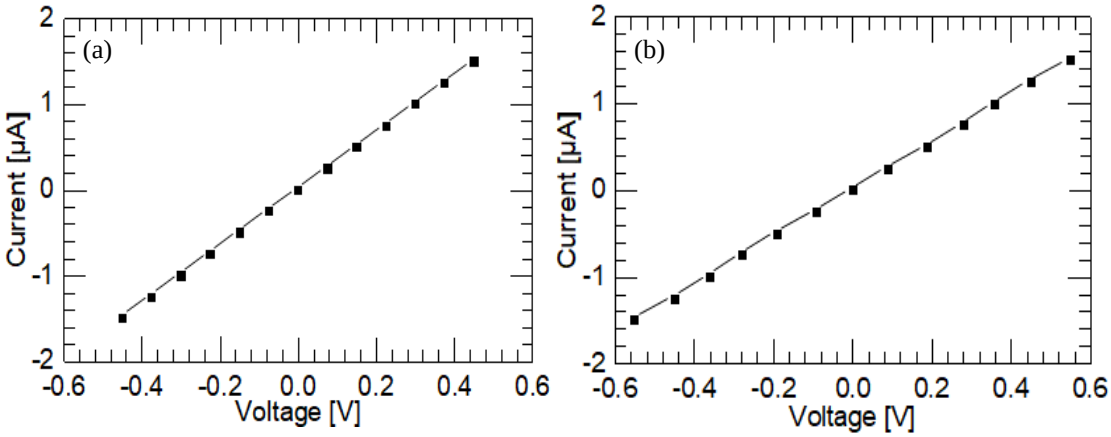

Figure 6.12: Current-voltage characteristics for (a) bottom microbolometer and (b) top microbolometer.

6.2.2 Voltage Noise PSD Results

We have measured the voltage noise PSD of the fabricated Two-microbolometer stack as a function of frequency at bias current between 80-320 nA before and after annealing. Figure 6.13(a) shows the voltage noise PSD at 3 different biased currents. We can notice that there is a high 1/*f*-noise and there is no clear flat region for the Johnson noise in the frequency range of 1 to 1000 Hz. The devices were annealed in

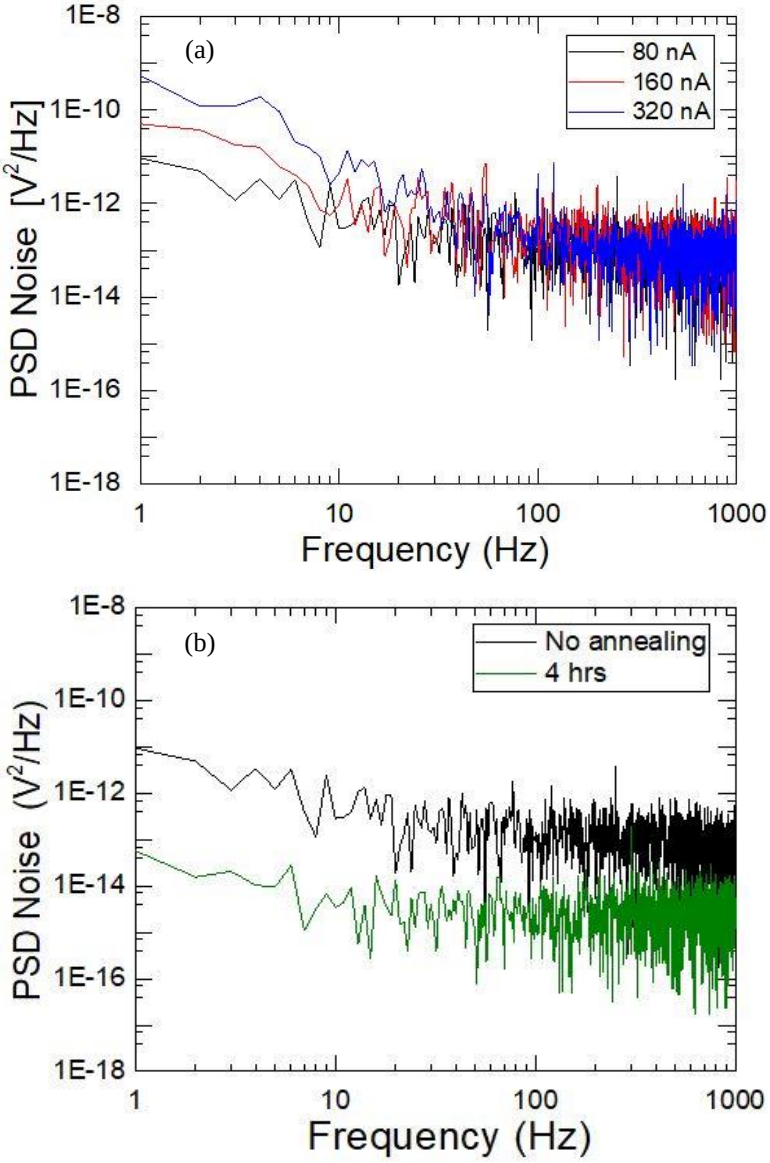

Figure 6.13: (a) voltage noise PSD at 3 different biased currents (b) voltage noise PSD after 4 hours of vacuum annealing at temperature of 300 ºC at 80 nA.

vacuum at 300 °C for duration from 1 hour to 4 hours and the PSD noise was measured after 4 hours of annealing as shown in Figure 6.13(b). The results demonstrate that the voltage noise was reduced with the lowest measured voltage noise PSD at the corner frequency 8 Hz was 3.41×10^{-15} V^2/Hz for the device that was biased with 80 nA. The voltage noise before annealing at the same bias current and corner frequency was 8.51×10^{-12} V^2/Hz at 8 Hz. This is 2.49×10^3 times reduction in noise, The corresponding Hooge's parameters γ, β and K_f for the bottom microbolometer device before and after annealing in vacuum were 1.31, 1.88, 3.81×10^{-12}, and 1.11, 1.93, 6.92×10^{-13} , respectively. The value of γ is close to 1 after annealing which indicates that the 1/*f*-noise is dominant at low frequencies. The decrease in K_f after annealing is attributed to the reduction of 1/*f*-noise. The K_f value depends on the quality of the crystal, and on the scattering mechanisms that determine the mobility μ. The β value was close to 2 when the device was annealed for 4 hours.

6.2.3 Optical Measurements as a Function of Chopping Frequency

The optical response of the Two-microbolometer stack was measured using the same setup used for the single cavity design. The responsivity and detectivity were measured in vacuum at room temperature and plotted as a function of chopper frequency at different bias currents for the bottom ant top microbolometers with different metasurfaces as shown in Figure 6.14 and Figure 6.15. The highest measured voltage responsivity and detectivity for the bottom microbolometer were 1.07×10^4 (V/W) and 7.98×10^7 (cm-$Hz^{1/2}$/W) respectively, while it was 2.06×10^3 (V/W) and 1.5×10^6 (cm-$Hz^{1/2}$/W) respectively, for the top microbolometer, both at a bias current of 320 nA. Figure 6.16 shows the responsivity and detectivity of the bottom and

microbolometers at a bias current of 320 nA. The measured thermal conductance and thermal response time for the two stack microbolometer were 7.78×10^{-8} (W/K) and 3.54

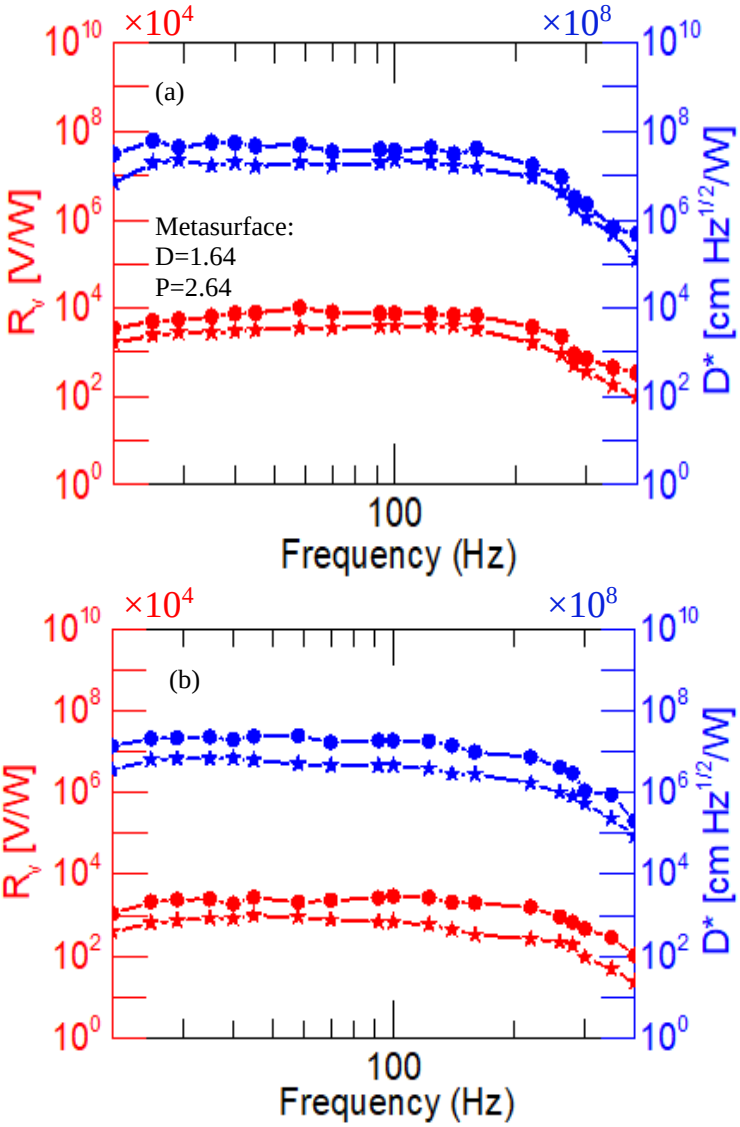

Figure 6.14: Measured voltage Responsivity and detectivity as a function of chopper frequency at different biased currents measured in vacuum for (a) bottom microbolometer and (b) top microbolometer.

ms, respectively for the bottom microbolometer, while it was 5.24×10^{-8} (W/K) and 4.31 ms, respectively for the top microbolometer. The absorptivity for the bottom and top microbolometers were calculated to be 37.54%, and 21.15 % respectively, by fitting the

measured data for responsivity, thermal conductance, and thermal response time. The thermal mass was calculated from the measured thermal conductance and thermal response time to be as 2.75×10^{-10} (J/K), and 2.25×10^{-10} (J/K), for the bottom and top microbolometers respectively. A summary of the measured and fitted data for the two-microbolometer stack design are presented in Table 5.

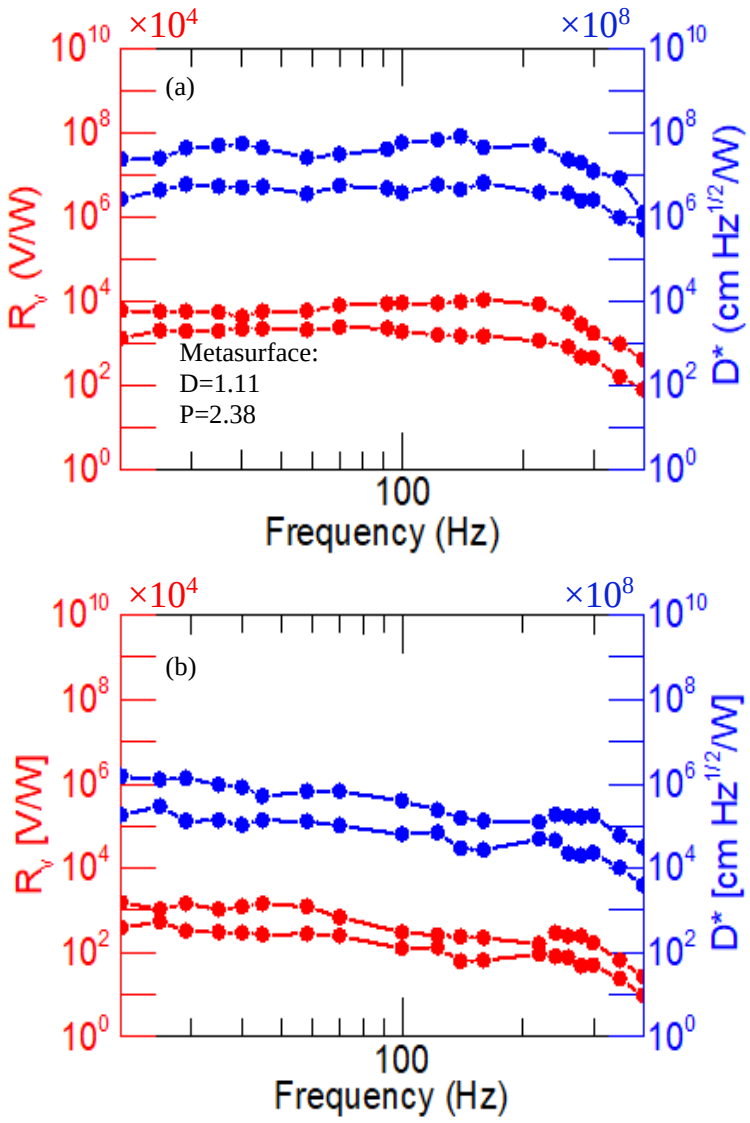

Figure 6.15: Measured voltage Responsivity and detectivity as a function of chopper frequency at different biased currents measured in vacuum for (a) bottom microbolometer and (b) top microbolometer.

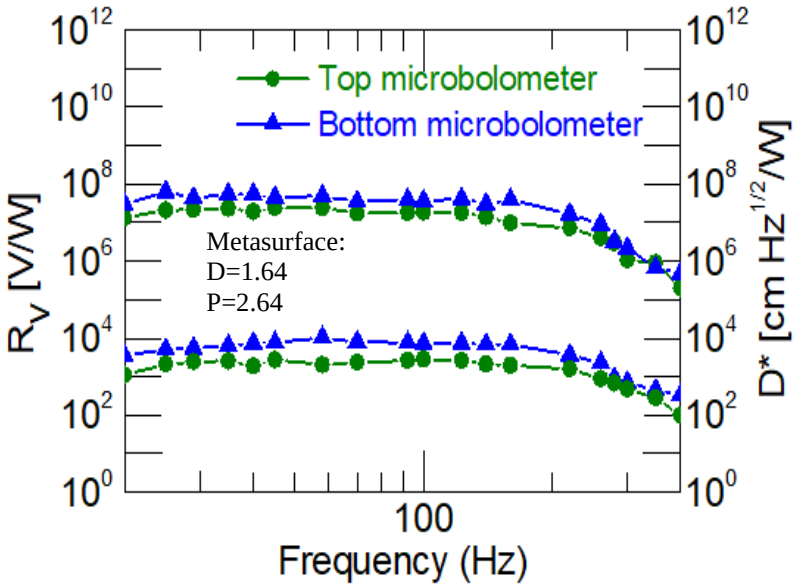

Figure 6.16: The responsivity and detectivity of the bottom and top microbolometers at a bias current of 320 nA.

Table 5: Summary of the Two-microbolometer stack properties.

Description	Bottom Microbolometer/FSS	Top Microbolometer
Responsivity R_v(V/W)	1.07×10^{4}	2.06×10^{3}
Detectivity D* (cm-Hz$^{1/2}$/W)	7.98×10^{7}	1.52×10^{6}
Thermal Conductance G_{th} (W/K)	7.78×10^{-8}	5.24×10^{-8}
Thermal response time τ_{th} (ms)	1.13	1.52
Absorptivity η (%)	37.54	21.15
Thermal mass C (J/K)	2.74×10^{-10}	2.25×10^{-10}

6.2.4 Optical Measurements as Function of Wavelength

The optical response of the two-microbolometers stack were measured as a function of wavelength using Newport 60090 blackbody light source, a 6575 infrared ceramic element with radiation wavelength between 0.6-16 µm, a 60077 ZnSe condenser, a Newport monochromator, and an optical long pass filter with transmittance between 1.25-16 µm. The measurements were performed in vacuum inside a cryostat through a

ZnSe window (2–16 µm), and inside an EM shielded box. The microbolometer was mounted on a vertical stage inside the cryostat allowing the chopped light, that is controlled by a chopper frequency controller to fully illuminate the microbolometer surface through the ZnSe window. The devices were connected to a preamplifier (PAR5113) and a Hewlett-Packard 35670A dynamic signal analyzer, and were DC biased from 80 to 320 nA. The dynamic signal analyzer simultaneously measured the signal amplitude and noise per unit bandwidth for each chopper frequency. The spectral

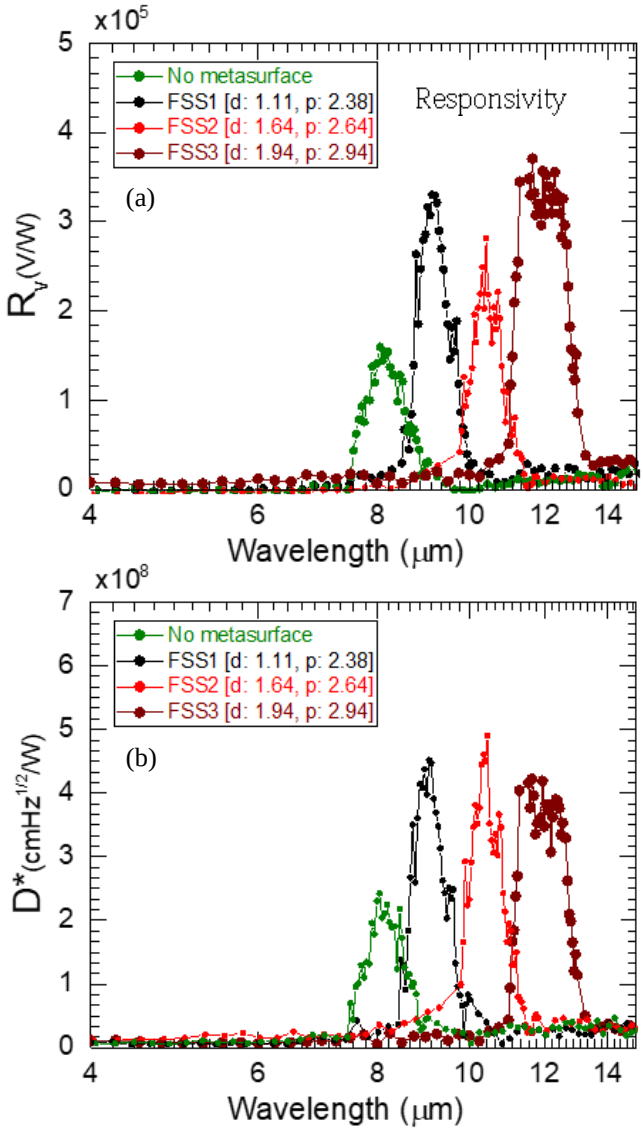

Figure 6.17: Different metasurface geometries showing multispectral response (a) responsivity (b) detectivity.

responsivity and detectivity of fabricated microbolometers were also measured in vacuum at room temperature. Each microbolometer in the Two-microbolometer stack was measured as shown in Figure 6.17 with different metasurfaces. The measurement demonstrates that the spectral response changes as a function of metasurface. Narrow band was achieved at certain wavelength depending on the geometry of the metasurface. When the disk diameter and periodicity changed, the spectral response was shifted to a different spectral window. Also, each microbolometer captures a portion of the spectral window with the top microbolometer response peak at 8 μm. These results demonstrate the ability of metasurface to tune the spectral response and multispectral absorption by stacking two microbolometers on a single pixel size.

CHAPTER 7: CONCLUSION

This thesis presents the design, fabrication, and testing of two microbolometer architectures, with focus on device architecture. Two designs are investigated. In the first design, the devices are fabricated with the legs positioned on the side of the microbolometer pixel. This is facilitated by the use of the metasurface which removes the need for a Fabry-Perot 1/4 cavity. The metasurface potentially allows spectrally dependent IR absorption. The second design extends this architecture to include a second microbolometer suspended above the first microbolometer to form a single pixel and with dual-air cavity, fabricated on top of each other.

The first microbolometer was designed and fabricated with a pixel area of 25×25 μm^2 and 40×40 μm^2. The integration of the metasurface disk arrays on top of the $Si_{344}Ge_{0.602}O_{0.054}$ sensing layer improved the TCR, Resistivity, and absorptance of the device at narrowband and broadband across the LWIR window. The $Si_{0.09}Ge_{0.72}O_{0.19}$ sensing layer was suspended using polyimide sacrificial layer of 2 µm and the structure was held by a SI_3N_4 support layer of 340 *nm* above the substrate to provide thermal isolation which lowers the thermal conductance and increase the responsivity and detectivity of the device. The single cavity microbolometer results demonstrated that the current voltage relationship is linear up to 1 µA. Joule heating was observed only above 1 µA in some devices. The typical two-wire resistance of the devices ranged between 200 kΩ to 593 kΩ. The measured TCR at 295 K for devices with area 40×40 μm^2 was -3.07 %/K. The highest measured voltage responsivity and detectivity for the microbolometer with a pixel size of 40×40 μm^2 were 4.37×10^4 V/W and 1.19×10^9 cm-$Hz^{1/2}$/W respectively, while it was 2.89×10^4 V/W and 8.62×10^8 cm-$Hz^{1/2}$/W

respectively, for the pixel size of 25×25 μm^2, both at a bias current of 80 nA. The measured thermal conductance and thermal response time for single cavity devices with area of 40×40 μm^2 and 25×25 μm^2 were 6.94×10^{-8} W/K and 3.53 ms, and 2.4×10^{-8} W/K and 4.79 ms, respectively. The absorptivity was calculated to be 25.81%, and 21.7%, respectively. The thermal mass was calculated from the measured thermal conductance and thermal response time to be as 3.07×10^{-10} J/K, and 1.15×10^{-10} J/K, respectively. The voltage noise power spectral density (PSD) of the fabricated devices were characterized. The devices were first annealed in vacuum at 300 ^oC, and in forming gases. The results demonstrated that annealing in vacuum lowered the noise much more than that of annealing in forming gases. The lowest measured noise in vacuum annealing for the metasurface integrated microbolometer was 2.16×10^{-16} V^2/Hz. The corner frequency of the device, where Johnson noise meet 1/*f*-noise was lowered to 10 Hz (from 70 Hz) after 4 hours annealing. In addition, the corresponding Hooge's parameters γ, β and K_f for the device were 1.02, 2.01, 2.637×10^{-14}, respectively.

The second microbolometer was design and fabricated with a pixel area of 40× 40 μm^2. Each microbolometer captures a portion of the spectrum to maximize the IR absorptance over two distinct spectral windows in the LWIR. The bottom microbolometer has a metasurface that selectively absorbs radiation between λ=8-14 μm, while reflecting radiation outside this range. The top structure is designed with a resonant Fabry-Pérot cavity located between the top microbolometer pixel and the bottom metasurface in order to absorb incident radiation between 7.5-9 μm and transmit any unabsorbed radiation outside this window. The highest measured voltage responsivity and detectivity for the bottom microbolometer were 1.07×10^4 V/W and 7.98×10^7 cm-$Hz^{1/2}$/W respectively, while it was 2.06×10^3 V/W and 1.52×10^6 cm-

$Hz^{1/2}/W$ respectively, for the top microbolometer, both at a bias current of 320 nA. The results show that the bottom microbolometer showed better performance than the top microbolometer due to the presence of the metasurfaces specially in terms of responsivity and detectivity. The results demonstrated that the current voltage relationship is linear up to 1.5 µA. Joule heating was observed only above 1.5 µA. The measured TCR at 295 K for device was -3.01 %/K for the bottom microbolometer. The measured thermal conductance and thermal response time for the device were 7.78×10^{-8} W/K and 1.13 ms, respectively for the bottom microbolometer, while it was 5.24×10^{-8} W/K and 1.52 ms, respectively for the top microbolometer. The absorptivity for the bottom and top microbolometers were calculated to be 37.54 %, and 21.15 %, respectively. The thermal mass was calculated from the measured thermal conductance and thermal response time to be as 2.74×10^{-10} J/K, and 2.25×10^{-10} J/K, for the bottom and top microbolometers respectively. The lowest measured noise in vacuum annealing was 1.1×10^{-15} V^2/Hz at 8 Hz lowest corner frequency for the bottom microbolometer with metasurface. While it was 7.41×10^{-15} V^2/Hz at 200 Hz lowest corner frequency for the top conventional microbolometer. In addition, the corresponding Hooge's parameters γ, β and K_f for the bottom microbolometer after 4 hours vacuum annealing was 1.1, 1.93, and 6.92×10^{-13}, respectively.

BIBLIOGRAPHY

[1] Black, S. H., Sessler, T., Gordon, E., Kraft, R., Kocian, T., Lamb, M. Yang, T. (2011, May). Uncooled detector development at Raytheon. *SPIE. Proc*. Vol. 8012, p. 80121A.

[2] Hanson, C. M., Ajmera, S. K., Brady, J., Fagan, T., McCardel, W., Morgan, D. Taylor, M. F. (2010, July). Small pixel a-Si/a-SiGe bolometer focal plane array technology at L-3 Communications. *SPIE. Proc*. Vol. 7660, p. 76600R.

[3] Li, C. C., Han, C. J., & Skidmore, G. D. (2011). Overview of DRS uncooled VOx infrared detector development. *Optical engineering*, Vol. 50(6), p. 061017.

[4] Blackwell, R., Franks, G., Lacroix, D., Hyland, S., & Murphy, R. (2010). Small pixel uncooled imaging FPAs and applications. *SPIE. Proc.*, Vol. 7660, p. 303-309.

[5] Dufour, D., Marchese, L., Terroux, M., Oulachgar, H., Généreux, F., Doucet, M., Bergeron, A. (2015). Review of terahertz technology development at INO. *Journal of Infrared, Millimeter, and Terahertz Waves*, Vol. 36(10), p. 922-946.

[6] Mizrahi, U., Bikov, L., Giladi, A., Shiloah, N., Elkind, S., Czyzewski, T., Fraenkel, A. (2010, May). New developments in SCD's 17-µm VOx µ-bolometer product line. *SPIE. Proc*. Vol. 7660, p. 76600W.

[7] Marshall, C. A., Butler, N. R., Blackwell, R. J., Murphy, R., Breen, T. B. (1996, June). Uncooled infrared sensors with digital focal plane array. *SPIE. Proc*. Vol. 2746, p. 23-31.

[8] Black, S., Ray, M., Hewitt, C., Wyles, R., Gordon, E., Almada, K., Sessler, T. (2008, May). RVS uncooled sensor development for tactical applications. *SPIE.*

Proc. Vol. 6940, p. 676-684.

[9] Murphy, D., Ray, M., Wyles, J., Hewitt, C., Wyles, R., Gordon, E., ... & Black, S. (2007, May). 640×512 17 μm microbolometer FPA and sensor development. *SPIE. PROC*. Vol. 6542, p. 65421Z.

[10] Hai, M. L., Cheng, Q., Hesan, M., Qu, C., Kinzel, E. C., Almasri, M. (2018). Amorphous $Si_xGe_yO_{1-x-y}$ thin films for uncooled infrared microbolometers. *SPIE. Proc*. Vol. 95, p. 227-235.

[11] Moreno, M., Jiménez, R., Torres, A., Ambrosio, R. (2015). Microbolometers based on amorphous silicon–germanium films with embedded nanocrystals. *IEEE Transactions on Electron Devices,* vol. 62(7), p. 2120-2127.

[12] Calleja, C., Torres, A., Moreno, M., Rosales, P., Sanz-Pascual, M. T. Velázquez, M. (2016). A microbolometer fabrication process using polymorphous silicon–germanium films (pm-SixGey: H) as thermosensing material. *physica status solidi (a)*, Vol. 213(7), p. 1864-1868.

[13] Ajmera, S. K., Syllaios, A. J., Tyber, G. S., Taylor, M. F., Hollingsworth, R. E. (2010, May). Amorphous silicon thin-films for uncooled infrared microbolometer sensors. *SPIE. Proc*. vol. 7660, p. 338-345.

[14] Rogalski, A. (2022). Van der Waals materials for HOT infrared detectors: A review. *Opto-Electronics Review*, e140551-e140551.

[15] Ong, Y. Y., Chen, B. T., Tay, F. E., Iliescu, C. (2006, April). Process analysis and optimization on PECVD amorphous silicon on glass substrate. *Journal of Physics: Conference Series*, Vol. 34, No. 1, p. 134.

[16] Hanson, C. M. (2005, May). Compact, rugged, and intuitive thermal imaging cameras for homeland security and law enforcement applications. *SPIE. Proc.*

Vol. 5778, p. 751-756.

[17] Seto, J. Y. (1975). The electrical properties of polycrystalline silicon films. *Journal of Applied Physics,* Vol. 46(12), p. 5247-5254.

[18] Dong, L., Yue, R., Liu, L. (2003). An uncooled microbolometer infrared detector based on poly-SiGe thermistor. *Sensors and Actuators A: Physical,* Vol. 105(3), p. 286-292.

[19] Xu, R., Li, W., He, J., Sun, Y. Jiang, Y. D. (2013). Boron-doped nanocrystalline silicon germanium thin films for uncooled infrared bolometer applications. *Infrared Physics & Technology,* Vol. 58, p. 32-35.

[20] Sedky, S., Fiorini, P., Caymax, M., Verbist, A., Baert, C. (1998). IR bolometers made of polycrystalline silicon germanium. *Sensors and Actuators A: Physical,* Vol. 66(1-3), p. 193-199.

[21] Leonov, V. N., Creten, Y., De Moor, P., Du Bois, B., Goessens, C., Grietens, B. Vermeiren, J. P. (2003, October). Small two-dimensional and linear arrays of polycrystalline SiGe microbolometers at IMEC-XenICs. *SPIE. Proc*. Vol. 5074, pp. 446-457.

[22] Sobolewski, R., Butler, D. P. Celik-Butler, Z. (2001, March). Cooled and uncooled infrared detectors based on yttrium barium copper oxide. *International Society for Optics and Photonics,* Vol. 4318, p. 204-214.

[23] Almasri, M., Butler, D. P. Celik-Butler, Z. (2001). Self-supporting uncooled infrared microbolometers with low-thermal mass. *Journal of microelectromechanical systems,* Vol. 10(3), p. 469-476.

[24] Almasri, M. F., Celik-Butler, Z., Butler, D. P., Yaradanakul, A. Yildiz, A. (2001, October). Semiconducting YBaCuO microbolometers for uncooled broadband

IR sensing. *SPIE. Proc.* Vol. 4369, pp. 264-273.

[25] Gray, J. E., Celik-Butler, Z., Butler, D. P. Almasri, M. F. (1998, October). Semiconducting YBaCuO as infrared-detecting bolometers. *SPIE. Proc*. Vol. 3436, pp. 555-565.

[26] Forsberg, F., Fischer, A. C., Roxhed, N., Samel, B., Ericsson, P., Stemme, G. Niklaus, F. (2013). Heterogeneous 3D integration of 17 μm pitch Si/SiGe quantum well bolometer arrays for infrared imaging systems. *Journal of Micromechanics and Microengineering*, Vol. 23(4), pp. 045017.

[27] Jin, Y. O., Saint-John, D., Podraza, N., Jackson, T. N. Horn, M. W. (2015). High temperature coefficient of resistance molybdenum oxide and nickel oxide thin films for microbolometer applications. *Optical Engineering*, Vol. 54(3), pp. 037101.

[28] Shie, J. S., Chen, Y. M., Ou-Yang, M. Chou, B. C. (1996). Characterization and modeling of metal-film microbolometer. *Journal of Microelectromechanical systems*, Vol. 5(4), pp. 298-306.

[29] Ramakrishna, M. V. S., Karunasiri, G., Sridhar, U. Chen, G. (1999, April). Performance of titanium and amorphous germanium microbolometer infrared detectors. *SPIE. Proc*. Vol. 3666, pp. 415-420.

[30] Kolahdouz, M., Farniya, A. A., Östling, M. Radamson, H. H. (2011). The performance improvement evaluation for SiGe-based IR detectors. *Solid-state electronics*, Vol. 62(1), pp. 72-76.

[31] Sumesh, M. A., Karanth, S., Prakash, S., Laxmiprasad, A. S. Nagendra, C. L. (2013). Ion beam sputtered Ge–Si–O amorphous thin films for microbolometer infrared detectors and their application in earth sensors. *Sensors and Actuators*

A: Physical, Vol. 192, pp. 81-91.

[32] Iborra, E., Clement, M., Herrero, L. V. Sangrador, J. (2002). IR uncooled bolometers based on amorphous Ge/sub x/Si/sub 1-x/O/sub y/on silicon micromachined structures. *Journal of microelectromechanical systems*, Vol. 11(4), pp. 322-329.

[33] Clement, M., Iborra, E., Sangrador, J., & Barberan, I. (2001). Amorphous Ge_x $Si_{1-x}O_y$ sputtered thin films for integrated sensor applications. *Journal of Vacuum Science & Technology B*: Microelectronics and Nanometer Structures Processing, Measurement, and Phenomena, vol. 19(1), pp. 294-298.

[34] Ahmed, A. H. Z. Tait, R. N. (2003). Characterization of amorphous $Ge_xSi_{1-x}O_y$ for micromachined uncooled bolometer applications. *Journal of applied physics*, Vol. 94(8), pp. 5326-5332.

[35] Rana, M. M. Butler, D. P. (2006). Radio frequency sputtered Si1− xGex and Si1− xGexOy thin films for uncooled infrared detectors. *Thin Solid Films*, Vol. 514(1-2), pp. 355-360.

[36] Murphy, D., Ray, M., Kennedy, A., Wyles, J., Hewitt, C., Wyles, R., & Kostrzewa, T. (2005, May). Expanded applications for high performance VOx microbolometer FPAs. *SPIE. Proc*. Vol. 5783, pp. 448-459.

[37] Murphy, D., Ray, M., Wyles, J., Hewitt, C., Wyles, R., Gordon, E. Black, S. (2007, May). 640×512 17 μm microbolometer FPA and sensor development. *SPIE. Proc.* Vol. 6542, p. 65421Z.

[38] Ajmera, S. K., Syllaios, A. J., Tyber, G. S., Taylor, M. F. Hollingsworth, R. E. (2010, May). Amorphous silicon thin-films for uncooled infrared microbolometer sensors. *SPIE. Proc.* Vol. 7660, pp. 338-345.

[39] Hanson, C. M., Beratan, H. R. Arbuthnot, D. L. (2008, April). Uncooled thermal imaging with thin-film ferroelectric detectors. *SPIE. Proc.* Vol. 6940, pp. 700-711.

[40] Rub, M., Bauer, J. Vogt, H. (2007, May). The geometric design of microbolometer elements for uncooled focal plane arrays. *SPIE. Proc.* Vol. 6542, p. 654223.

[41] Leonov, V. N., Creten, Y., De Moor, P., Du Bois, B., Goessens, C., Grietens, B., & Vermeiren, J. P. (2003, October). Small two-dimensional and linear arrays of polycrystalline SiGe microbolometers at IMEC-XenICs. *SPIE. Proc*. Vol. 5074, pp. 446-457.

[42] Alves, F., Karamitros, A., Grbovic, D., Kearney, B. T., & Karunasiri, G. (2012). Highly absorbing nano-scale metal films for terahertz applications. *Optical Engineering*, Vol. 51(6), pp. 063801.

[43] Enukova, T. A., Ivanova, N. L., Kulikov, Y. V., Malyarov, V. G. Khrebtov, I. A. (1997). Amorphous silicon and germanium films for uncooled microbolometers. *Technical Physics Letters*, Vol. 23(7), pp. 504-506.

[44] Byrnes, J. (Ed.). (2008). Unexploded ordnance detection and mitigation. Springer Science & Business Media.

[45] Breen, T. B., Kohin, M., Marshall, C. A., Murphy, R., White, T. E., Leary, A. R. Parker, T. W. (1999, July). Even more applications of uncooled microbolometer sensors. *SPIE. Proc*. Vol. 3698, pp. 308-319.

[46] Johnson, W. R., Hook, S. J. Shoen, S. M. (2012). Microbolometer imaging spectrometer. *Optics letters*, Vol. 37(5), pp. 803-805.

[47] Lohrmann, D., Littleton, R. T., Reese, C. E., Murphy, D. Vizgaitis, J. N. (2013).

Uncooled long-wave infrared small pixel focal plane array and system challenges. *Optical Engineering*, Vol. 52(6), pp. 061305.

[48] Hanson, C. M., Ajmera, S. K., Brady, J., Fagan, T., McCardel, W., Morgan, D., ... & Taylor, M. F. (2010, July). Small pixel a-Si/a-SiGe bolometer focal plane array technology at L-3 Communications. *SPIE. Proc*. Vol. 7660, p. 76600R.

[49] Li, C., Han, C. J., Skidmore, G. D., & Hess, C. (2010, May). DRS uncooled VOx infrared detector development and production status. *SPIE. Proc.* Vol. 7660, pp. 276-284.

[50] Hay, K. A. (2006, September). Large format VOx microbolometer UFPA development at ITC. *SPIE. Proc.* Vol. 6295, p. 629505.

[51] Yon, J. J., Astier, A., Bisotto, S., Chamingis, G., Durand, A., Martin, J. L., ... & Tissot, J. L. (2005, May). First demonstration of 25 µm pitch uncooled amorphous silicon microbolometer IRFPA at LETI-LIR. *SPIE. Proc*. Vol. 5783, pp. 432-440.

[52] Rana, M. M. Butler, D. P. (2005, May). Amorphous Ge x Si 1-x and Ge x Si 1-x O y thin films for uncooled microbolometers. *SPIE. Proc*. Vol. 5783, pp. 597-606.

[53] Ahmed, A. H. Z., Tait, R. N., Oogarah, T. B., Liu, H. C., Denhoff, M. W., Sproule, G. I. Graham, M. J. (2004, December). A surface micromachined amorphous GexSi1-xOy bolometer for thermal imaging applications. *SPIE. Proc*. Vol. 5578, pp. 298-308.

[54] Song, W. B. Talghader, J. J. (2006). Design and characterization of adaptive microbolometers. *Journal of Micromechanics and Microengineering*, Vol. 16(5), pp. 1073.

[55] Petriashvili, G. Chanishvili, A. (2019). Liquid crystal blue phases interconversions based real-time thermal imaging device. *Optics Express,* Vol. 27(9), pp. 13526-13531.

[56] Leonov, V. N. Butler, D. P. (2001). Two-color thermal detector with thermal chopping for infrared focal-plane arrays. *Applied Optics*, Vol. 40(16), pp. 2601-2610.

[57] Almasri, M., Xu, B. Castracane, J. (2006). Amorphous silicon two-color microbolometer for uncooled IR detection. *IEEE Sensors journal*, Vol. 6(2), pp. 293-300.

[58] Walia, S., Shah, C. M., Gutruf, P., Nili, H., Chowdhury, D. R., Withayachumnankul, W. Sriram, S. (2015). Flexible metasurfaces and metamaterials: A review of materials and fabrication processes at micro-and nano-scales. *Applied Physics Reviews,* Vol 2(1), pp. 011303.

[59] Chen, K., Adato, R., & Altug, H. (2012). Dual-band perfect absorber for multispectral plasmon-enhanced infrared spectroscopy. *ACS nano*, Vol. 6(9), pp. 7998-8006.

[60] Hendrickson, J., Guo, J., Zhang, B., Buchwald, W., & Soref, R. (2012). Wideband perfect light absorber at midwave infrared using multiplexed metal structures. *Optics letters*, Vol. 37(3), pp. 371-373.

[61] Huang, H., Xia, H., Xie, W., Guo, Z., Li, H., & Xie, D. (2018). Design of broadband graphene-metamaterial absorbers for permittivity sensing at mid-infrared regions. *Scientific reports*, Vol. 8(1), pp. 1-10.

[62] Ogawa, S., Okada, K., Fukushima, N., & Kimata, M. (2012). Wavelength selective uncooled infrared sensor by plasmonics. *Applied Physics Letters*, Vol.

100(2), pp. 021111.

[63] Ogawa, S. Kimata, M. (2017). Wavelength-or polarization-selective thermal infrared detectors for multi-color or polarimetric imaging using plasmonics and metamaterials. *Materials*, Vol. 10(5), pp. 493.

[64] Shrekenhamer, D., Miragliotta, J. A., Brinkley, M., Fan, K., Peng, F., Montoya, J. A. Padilla, W. J. (2016, September). Electronic and thermally tunable infrared metamaterial absorbers. *SPIE. Proc.* Vol. 9918, p. 99180U.

[65] Safaei, A., Modak, S., Lee, J., Chandra, S., Franklin, D., Vázquez-Guardado, A. Chanda, D. (2018). Multi-spectral frequency selective mid-infrared microbolometers. *Optics express*, Vol. 26(25), pp. 32931-32940.

[66] De Santis, A. (2011, December). Status and prospects for Lorentz and CPT violation tests at KLOE and KLOE-2. *In Journal of Physics: Conference Series*. Vol. 335, No. 1, p. 012058.

[67] Kim, T., Bae, J. Y., Lee, N. Cho, H. H. (2019). Hierarchical metamaterials for multispectral camouflage of infrared and microwaves. *Advanced Functional Materials*, Vol. 29(10), pp. 1807319.

[68] Ogawa, S., Fujisawa, D., Hata, H., Kimata, M. (2016, March). Absorption properties of simply fabricated all-metal mushroom plasmonic metamaterials incorporating tube-shaped posts for multi-color uncooled infrared image sensor applications. *In Photonics*. Vol. 3, No. 1, p. 9.

[69] Kang, S., Qian, Z., Rajaram, V., Calisgan, S. D., Alù, A., & Rinaldi, M. (2019). Ultra-narrowband metamaterial absorbers for high spectral resolution infrared spectroscopy. *Advanced Optical Materials*, Vol. 7(2), pp. 1801236.

[70] Montoya, J. A., Tian, Z. B., Krishna, S. Padilla, W. J. (2017). Ultra-thin infrared

metamaterial detector for multicolor imaging applications. *Optics express,* Vol. 25(19), pp. 23343-23355.

[71] Chen, X. L., Tian, C. H., Che, Z. X. Chen, T. P. (2018). Selective metamaterial perfect absorber for infrared and 1.54 μm laser compatible stealth technology. *Optik,* Vol, 172, pp. 840-846.

[72] Alves, F., Pimental, L., Grbovic, D., & Karunasiri, G. (2018). MEMS terahertz-to-infrared band converter using frequency selective planar metamaterial. *Scientific Reports*, Vol. 8(1), pp. 1-14.

[73] Lee, N., Kim, T., Lim, J. S., Chang, I. Cho, H. H. (2019). Metamaterial-selective emitter for maximizing infrared camouflage performance with energy dissipation. *ACS applied materials & interfaces*, Vol. 11(23), pp. 21250-21257.

[74] Lin, P. S., Shen, T. W., Chang, K. C. Fang, W. (2020, January). Monolithic integration of plasmonic meta-material absorber with CMOS-MEMs infrared sensor for responsivity enhancement and human detection application. *IEEE MEMS*. pp. 157-160.

[75] Jung, J. Y., Lee, J., Choi, D. G., Choi, J. H., Jeong, J. H., Lee, E. S. Neikirk, D. P. (2015). Wavelength-selective infrared metasurface absorber for multispectral thermal detection. *IEEE Photonics Journal*, Vol. 7(6), pp. 1-10.

[76] Pitchappa, P., Ho, C. P., Kropelnicki, P., Singh, N., Kwong, D. L. Lee, C. (2014). Dual band complementary metamaterial absorber in near infrared region. *Journal of Applied Physics,* Vol. 115(19),pp. 193109.

[77] Zhang, N., Zhou, P., Wang, S., Weng, X., Xie, J. Deng, L. (2015). Broadband absorption in mid-infrared metamaterial absorbers with multiple dielectric layers. *Optics Communications,* Vol. 338, pp. 388-392.

[78] Ma, W., Wen, Y., Yu, X., Feng, Y. Zhao, Y. (2015). Performance enhancement of uncooled infrared focal plane array by integrating metamaterial absorber. *Applied Physics Letters*, Vol. 106(11), pp. 111108.

[79] Hui, Y., Gomez-Diaz, J. S., Qian, Z., Alu, A. Rinaldi, M. (2016). Plasmonic piezoelectric nanomechanical resonator for spectrally selective infrared sensing. *Nature communications*, Vol. 7(1), pp. 1-9.

[80] Grant, J., Escorcia-Carranza, I., Li, C., McCrindle, I. J., Gough, J. Cumming, D. R. (2013). A monolithic resonant terahertz sensor element comprising a metamaterial absorber and micro-bolometer. *Laser & Photonics Reviews*, Vol. 7(6), pp. 1043-1048.

[81] Luo, H. Cheng, Y. (2019). Dual-band terahertz perfect metasurface absorber based on bi-layered all-dielectric resonator structure. *Optical Materials*, Vol. 96, pp. 109279.

[82] Grant, J., Ma, Y., Saha, S., Khalid, A. Cumming, D. R. (2011). Polarization insensitive, broadband terahertz metamaterial absorber. *Optics letters*, Vol. 36(17), pp. 3476-3478.

[83] Shchegolkov, D. Y., Azad, A. K., O'hara, J. F. Simakov, E. I. (2010). Perfect subwavelength fishnetlike metamaterial-based film terahertz absorbers. *Physical review B*, Vol. 82(20), pp. 205117.

[84] Bayraktar, Z., Gregory, M. D., Wang, X., & Werner, D. H. (2012). Matched impedance thin planar composite magneto-dielectric metasurfaces. *IEEE Transactions on Antennas and Propagation*, Vol 60(4), pp. 1910-1920.

[85] Landy, N. I., Bingham, C. M., Tyler, T., Jokerst, N., Smith, D. R. Padilla, W. J. (2009). Design, theory, and measurement of a polarization-insensitive absorber

for terahertz imaging. *physical review B*, Vol. 79(12), pp. 125104.

[86] Yao, Y., Shankar, R., Kats, M. A., Song, Y., Kong, J., Loncar, M. Capasso, F. (2014). Electrically tunable metasurface perfect absorbers for ultrathin mid-infrared optical modulators. *Nano letters*, Vol. 14(11), pp. 6526-6532.

[87] Belal, S. A. H. (2015). Determination of Trace Elements in Human Hair and Nails as a measure of the Nutritional Imblance in Kassala State, Using XRF Spectroscopy (Doctoral dissertation, Sudan University of Science and Technology).

[88] Mroziewicz, B. (1988). Photon-detectors: *An overview of technology. Measurement*, Vol. 6(3), pp. 112-120..

[89] A. Wilson, *Optical Radiation Detector*. *Academic Press*, 2013.

[90] Rogalski, A. (2002). Infrared detectors: an overview. *Infrared physics & technology*, Vol. 43(3-5), pp. 187-210.

[91] S. Donati, (2020) " Thermal Detectors and Thermography ," *Photodetectors*, pp. 245–263.

[92] Putley, E. H. (1977). Thermal detectors. In Optical and Infrared Detectors (pp. 71-100). Berlin.

[93] Rogalski, A. W., Kopytko, M. E. Martyniuk, P. M. (2018). Antimonide-based infrared detectors: a new perspective. *SPIE-The International Society for Optics and Photonics*.

[94] Fedirko, V. A., Fetisov, E. A., Khafizov, R. Z., Rudakov, G. A. Sigarev, A. A. (2018). Thermopile IR Sensor Arrays. *In Proceedings of the Scientific-Practical Conference" Research and Development-2016"*, pp. 39-48.

[95] He, Y., Wang, Y. Li, T. (2020). Performance enhanced thermopile with rough

dielectric film black. *IEEE Electron Device Letters*, Vol. 41(4), pp. 593-596.

[96] Ashraf, S., Mattsson, C. G. Thungström, G. (2016, October). Fabrication of a mid-IR sensitive thermopile detector. *IEEE SENSORS*. pp. 1-3.

[97] Ashraf, S., Mattsson, C. G. Thungström, G. (2019). Fabrication and characterization of a SU-8 epoxy membrane-based thermopile detector with an integrated multilayered absorber structure for the Mid-IR region. *IEEE Sensors Journal*, Vol. 19(11), pp. 4000-4007.

[98] Ke, W., Wang, Y., Zhou, H., Li, T. Wang, Y. (2018). Design, fabrication, and characterization of a high-performance CMOS-compatible thermopile infrared detector with self-test function. *Journal of Micromechanics and Microengineering*, Vol. 28(12), pp. 125017.

[99] Li, W., Ni, Z., Wang, J. Li, X. (2019). A front-side microfabricated tiny-size thermopile infrared detector with high sensitivity and fast response. *IEEE Transactions on Electron Devices*, Vol. 66(5), pp. 2230-2237.

[100] Hou, H., Huang, Q., Liu, G. Qiao, G. (2019). Enhanced performances of CMOS-MEMS thermopile infrared detectors using novel thin film stacks. *Infrared Physics & Technology*, Vol. 102, pp. 103058.

[101] Porter, S. G. (1981). A brief guide to pyroelectric detectors. *Ferroelectrics*, Vol. 33(1), pp. 193-206.

[102] Kao, K. C. (2004). Ferroelectrics, piezoelectrics, and pyroelectrics. *Dielectric phenomena in solids*, Vol. 4, pp. 213-282.

[103] Tanrikulu, M. Y., Yildizak, C., Okyay, A. K., Akar, O., Sarac, A. Akin, T. (2018, May). Single layer microbolometer detector pixel using ZnO material. *SPIE. Proc.* Vol. 10624, pp. 1062417.

[104] Kesim, Y. E., Battal, E., Tanrikulu, M. Y. Okyay, A. K. (2014). An all-ZnO microbolometer for infrared imaging. *Infrared Physics & Technology*, Vol. 67, pp. 245-249.

[105] Lv, J., Que, L., Wei, L., Zhou, Y., Liao, B. Jiang, Y. (2014). Uncooled microbolometer infrared focal plane array without substrate temperature stabilization. *IEEE Sensors Journal*, Vol. 14(5), pp. 1533-1544.

[106] McKitterick, C. B., Vora, H., Du, X., Karasik, B. S., & Prober, D. E. (2014). Graphene microbolometers with superconducting contacts for terahertz photon detection. *Journal of Low Temperature Physics*, Vol. 176(3), pp. 291-298.

[107] Datskos, P. G. Lavrik, N. V. (2003). Detectors-figures of merit. *Encyclopedia of Optical Engineering*, Vol. 349, pp.100.

[108] Rana, M. M. Butler, D. P. (2007, October). Amorphous Ge x Si 1-x O y: H Microbolometers with High Responsivity. *IEEE SENSORS*, pp. 519-522.

[109] Dong, L., Yue, R. Liu, L. (2003). An uncooled microbolometer infrared detector based on poly-SiGe thermistor. *Sensors and Actuators A: Physical*, Vol. 105(3), pp. 286-292.

[110] Mott, N. F., & Davis, E. A. (2012). Electronic processes in non-crystalline materials. Oxford university press.

[111] A. H. Z. Ahmed and R. N. Tait, (2003), "Characterization of amorphous GexSi1-xOy for micromachined uncooled bolometer applications," *J. Appl. Phys.*, vol. 94, no. 8, pp. 5326–5332.

[112] Rogalski, A. (2009). Infrared detectors for the future. *Acta Physica Polonica-Series A General Physics*, Vol. 116(3), pp. 389.

[113] Schottky, W. (2018). On spontaneous current fluctuations in various electrical

conductors. Journal of Micro/Nanolithography, MEMS, and MOEMS, Vol. 17(4), pp. 041001.

[114] Fish, P. J. (2017). Electronic noise and low noise design. *Macmillan International Higher Education*.

[115] Van Der Ziel, A. (1970). Noise in solid-state devices and lasers. *Proceedings of the IEEE*, Vol. 58(8), pp. 1178-1206.

[116] Buckingham, M. J. (1983). Noise in electronic devices and systems. JOHN WILEY & SONS, INC., 605 THIRD AVE., NEW YORK, NY 10158, USA.

[117] Kruse, P. W. (1997). Principles of uncooled infrared focal plane arrays. *Semiconductors and semimetals*. Vol. 47, pp. 17-42.

[118] Galeazzi, M., Boyce, K. R., Brekosky, R., Gygax, J. D., Kelley, R. L., Liu, D. Tan, P. (2002, February). Non-ideal effects in doped semiconductor thermistors. *AIP Conference Proceedings*. Vol. 605, No. 1, pp. 83-86.

[119] Sedky, S., Fiorini, P., Baert, K., Hermans, L., & Mertens, R. (1999). Characterization and optimization of infrared poly SiGe bolometers. *IEEE transactions on Electron Devices*, Vol. 46(4), pp. 675-682.

[120] F. N. Hooge, (1994). "1/*f*-Noise Sources," *IEEE Trans. Electron Devices*, vol. 41, no. 11, pp. 1926–1935.

[121] García, M., Ambrosio, R., Torres, A. Kosarev, A. (2004). IR bolometers based on amorphous silicon germanium alloys. *Journal of Non-Crystalline Solids*, Vol. 338, pp. 744-748.

[122] Butler, D. P., Çelik-Butler, Z. Sobolewski, R. (2001). Yttrium barium copper oxide as an infrared radiation sensing material. *Advanced Electronic and Photonic Materials and Devices*, pp. 169-195.

[123] Chang, S., Guo, X. Ni, X. (2018). Optical metasurfaces: progress and applications. *Annual Review of Materials Research,* Vo. 48, pp. 279-302.

[124] Solntsev, A. S., Agarwal, G. S. Kivshar, Y. S. (2021). Metasurfaces for quantum photonics. *Nature Photonics*, Vo. 15(5), pp. 327-336.

[125] Petriashvili, G. Chanishvili, A. (2019). Liquid crystal blue phases interconversions based real-time thermal imaging device. *Optics Express*, Vo. 27(9), pp. 13526-13531.

[126] Almasri, M., Xu, B. Castracane, J. (2006). Amorphous silicon two-color microbolometer for uncooled IR detection. *IEEE Sensors journal*, Vol. 6(2), pp. 293-300.

[127] Keskin, S. Akin, T. (2012, May). The first fabricated dual-band uncooled infrared microbolometer detector with a tunable micro-mirror structure. *SPIE. Proc.* Vol. 8353, pp. 461-471.

[128] Chen, K., Adato, R. Altug, H. (2012). Dual-band perfect absorber for multispectral plasmon-enhanced infrared spectroscopy. *ACS nano*, Vol. 6(9), pp. 7998-8006.

[129] Hendrickson, J., Guo, J., Zhang, B., Buchwald, W. Soref, R. (2012). Wideband perfect light absorber at midwave infrared using multiplexed metal structures. *Optics letters*, Vol. 37(3), pp. 371-373..

[130] Takagawa, Y., Ogawa, S. Kimata, M. (2015). Detection wavelength control of uncooled infrared sensors using two-dimensional lattice plasmonic absorbers. *Sensors*, Vol. 15(6), pp. 13660-13669.

[131] Tong, J., Suo, F., Tobing, L. Y., Yao, N., Zhang, D., Huang, Z. Zhang, D. H. (2020). High order magnetic and electric resonant modes of split ring resonator

metasurface arrays for strong enhancement of mid-infrared photodetection. *ACS Applied Materials & Interfaces*, Vol. 12(7), pp. 8835-8844.

[132] Chen, N., Pitchappa, P., Ho, C. P., Hasan, D., Kropelnicki, P., Alioto, M. Lee, C. (2016). Polarization controllable multispectral symmetry-breaking absorberin mid-infrared. *Journal of Applied Physics*, Vol. 120(6), pp. 063105.

[133] Han, S. W., Kim, J. W., Sohn, Y. S. Neikirk, D. P. (2004). Design of infrared wavelength-selective microbolometers using planar multimode detectors. *Electronics Letters*, Vol. 40(22), pp. 1410-1411.

[134] Ogawa, S., Fujisawa, D., Hata, H., & Kimata, M. (2016, March). Absorption properties of simply fabricated all-metal mushroom plasmonic metamaterials incorporating tube-shaped posts for multi-color uncooled infrared image sensor applications. *Photonics*. Vol. 3, No. 1, p. 9.

[135] Kinzel, E. (2014, July). Design of a Frequency-Selective Surface strain sensor. *Proceedings of the IEEE.* pp. 2074-2075.

[136] Asadchy, V. S., Faniayeu, I. A., Ra'Di, Y., Khakhomov, S. A., Semchenko, I. V. Tretyakov, S. A. (2015). Broadband reflectionless metasheets: frequency-selective transmission and perfect absorption. *Physical Review X*, Vol. 5(3), pp. 031005.

[137] Oliveri, G., Werner, D. H. Massa, A. (2015). Reconfigurable electromagnetics through metamaterials—A review. *Proceedings of the IEEE*, Vo. 103(7), pp. 1034-1056.

[138] Leite, D. M. G., Pereira, A. L. J., Da Silva, L. F. Silva, J. H. (2006). Nanocrystalline GaN and GaN: H films grown by RF-magnetron sputtering. *Brazilian journal of physics*, Vol. 36(3b), pp. 978-981.

[139] Balandin, A. A. (2013). Low-frequency 1/*f*-noise in graphene devices. *Nature nanotechnology*, Vo. 8(8), pp. 549-555.

[140] Ahmed, A. H. Z. Tait, R. N. (2003). Characterization of amorphous Ge x Si 1− x O y for micromachined uncooled bolometer applications. *Journal of applied physics*, Vol. 94(8), pp. 5326-5332.

[141] Clement, M., Iborra, E., Sangrador, J. Barberan, I. (2001). Amorphous Ge x Si 1− x O y sputtered thin films for integrated sensor applications. *Journal of Vacuum Science & Technology B*, Vol. 19(1), pp. 294-298.

[142] Ragauskas, M., Palenskis, V., Matukas, J., Pralgauskaite, S., Minkevicius, L., Kasalynas, I. Valusis, G. (2013, June). Low frequency noise characteristics of InGaAs bow-tie diodes for terahertz detection. *Proceedings of the IEEE*. pp. 1-4.

[143] Andersson, J. Y., Ericsson, P., Radamson, H. H., Wissmar, S. G. E. Kolahdouz, M. (2011). SiGe/Si quantum structures as a thermistor material for low cost IR microbolometer focal plane arrays. *Solid-State Electronics*, Vol. 60(1), pp. 100-104.

[144] Ahmed, M., Chitteboyina, M. M., Butler, D. P. Celik-Butler, Z. (2011). Temperature sensor in a flexible substrate. *IEEE Sensors Journal*, Vol. 12(5), pp. 864-869.

[145] Singh, V., Mathimalar, S., Dokania, N., Nanal, V., Pillay, R. G. Ramakrishnan, S. (2014). Heat Capacity Setup for Superconducting Bolometer Absorbers below 400 mK. *Journal of Low Temperature Physics*, Vol. 175(3), pp. 604-613.

VITA

Amjed Abdullah received his B.Sc. degree from the University of Mosul, Mosul, Iraq in 2008. He received his M.Sc. from the University of Missouri Columbia, Missouri, USA. He is currently working toward his Ph.D. degree in the electrical engineering at the University of Missouri, Columbia. His current research interests include design and fabrication of uncooled infrared microbolometers, silicon germanium oxide IR sensing material for uncooled IR detection, microfluidics, biosensors, and fiber optics.